Finite-frequency tomography with complex body waves - taking into account data uncertainty and correlation

Simon Christian Stähler

München 2013

Finite-frequency tomography with complex body waves - taking into account data uncertainty and correlation

Simon Christian Stähler

Dissertation
an der Fakultät für Geowissenschaften
der Ludwig–Maximilians–Universität
München

vorgelegt von
Simon Christian Stähler
aus Neu Isenburg

München, den 17.10.2013

Erstgutachter: Prof. Dr. Heiner Igel
Zweitgutachter: Dr. habil. Karin Sigloch
Tag der mündlichen Prüfung: 16.04.2014

Zusammenfassung

Seismische Tomographie ist die eindrücklichste und intuitivste Methode, Informationen über das tiefe Erdinnere, von der Kruste bis an die Kern-Mantel-Grenze zu erlangen. Die von entfernten Erdbeben aufgezeichneten Bodenbewegungen werden mit den für ein einfaches Erdmodell vorhergesagten verglichen, um ein verbessertes Modell zu erhalten. Dieses dreidimensionale Modell kann dann geodynamisch oder tektonisch interpretiert werden.
Durch die Entwicklung leistungsfähiger Computersysteme kann die Ausbreitung seismischer Wellen mittlerweile im gesamten messbaren Frequenzbereich simuliert werden, sodass dieses gesamte Spektrum der Tomographie zur Verfügung steht.
Die vorliegende Arbeit beschäftigt sich mit der Verbesserung der Wellenformtomographie. Zum einen wird die Nutzbarkeit eines komplexen Typs seismischer Wellen, der in der Mantelübergangszone zwischen 410 und 660 km Tiefe gestreuten triplizierten Wellen gezeigt. Diese Wellen versprechen eine erheblich bessere Auflösung der geodynamisch wichtigen Diskontinuitäten zwischen oberem und unterem Mantel als bisher verwendete teleseismische Wellen.
Zum anderen wird der nichtlineare Einfluss des Erdbebenmodells auf die Wellenformtomographie untersucht. Mittels Bayesianischer Inferenz werden Wahrscheinlichkeitsdichten für die Herdparameter des Erdbebens, wie Tiefe, Momententensor und Quellfunktion bestimmt. Dazu wird zuvor ein Modell der Messunsicherheit und des Modellierungsfehlers in der Herdinversion bestimmt, das bis dato nicht vorlag.
Dabei zeigt sich im Weiteren, dass der Effekt der Unsicherheit im Herdmodell eine nichtlineare und bisher weitgehend ignorierte Fehlerquelle in der seismischen Tomographie ist. Dieses Ergebnis ermöglicht es, die Varianz seismischer Laufzeit- und Wellenformmessungen sowie die Kovarianz zwischen einzelnen Messstationen zu bestimmen.
Die Ergebnisse dieser Arbeit können in Zukunft erheblich dazu beitra-

gen, die Unsicherheiten der seismischen Tomographie quantitativ zu bestimmen, um eventuell vorhandene Artefakte zu zeigen und damit geologischen Fehlinterpretationen tomographischer Ergebnisse vorzubeugen.

Summary

Seismic tomography is the most impressive method of inferring a picture of the deep interiour of the Earth, from the lower crust to the core mantle boundary. Recordings of ground motions caused by distant earthquakes are used to refine an existing earth model, employing difference between measured and predicted data. The resulting three-dimensional models and images can be interpreted in terms of tectonics and large-scale geodynamics.

The increase in computing power in the last decade has lead to an enormous progress in tomographic methods, which can now simulate and therefore exploit the whole frequency range of seismographic measurements.

This thesis refines waveform tomography in its flavour of finite-frequency tomography. It first shows that complex wave types, like the those perturbed by the discontinuities in the mantle transition zone can be used for waveform tomography. Using these waves promise an improved resolution of the geodynamically important transition zone compared to the hitherto used teleseismic waves.

A second part checks the nonlinear influence of the source model on waveform tomography. By the method of Bayesian inference, probability density functions of the source parameters depth, moment tensor, and the source time function are determined. For that, a model of the measurement uncertainties is necessary, which was hitherto not available and is derived from a large catalogue of source solutions.

The results of the probabilistic source inversion allow to quantify the effect of source uncertainty on seismic tomography. This allows to estimate the variance of seismic traveltimes and waveforms and also the covariance between different seismographic stations.

The results of this work could improve uncertainty estimation in seismic tomography, show potential artefacts in the result and therefore avoid misinterpretation of tomographic images by geologists and others.

Contents

List of Figures

List of Tables

I have been insisting for about 20 years that the claim of finality for any scientific inference is absurd.

(Jeffreys, 1939)

1 Introduction

1.1 Historic overview and state of the art

The curious task of Earth Sciences is to infer a four-dimensional model of our whole planet in time, solely by measurements on the two-dimensional surface of it. Compared to the eons in which geological processes unfold, these measurements are quasi instantaneous. So if there ever was a perfect example for an inverse problem, it is the reconstruction of the tectonic history of the Earth's crust, mantle and core.

One of the most important tools to infer the structure of the Earth's mantle is seismology. The original interest was to explain the devastating ground shaking. The invention of the seismograph allowed to measure these motions and quantify them. In 1889, seismographs in Potsdam and Wilhelmshaven recorded a signal from an earthquake in Japan and showed that seismic waves travel through the whole planet (Von Rebeur-Paschwitz, 1889). Two decades later, double arrivals of seismic waves from an earthquake in Zagreb led Andrija Mohorovicic to postulate the existence of a geological boundary in a depth of 54 km (Mohorovičić, 1909), which later proved to be a global feature, namely the geological boundary between the crust and the mantle. At the turn of the centuries, Richard Oldham first separated body waves and surface waves in the seismic record (Oldham, 1900) and later discovered a delay on body waves (Oldham, 1906), which he speculated to result from the iron core predicted by Wiechert from observations on the density and inertia of the earth (Wiechert, 1896, 1897). Using

much clearer seismographic records, Benno Gutenberg inferred the existence of a strong discontinuity in 2890 km depth from seismic records (Gutenberg, 1913), which Harold Jeffreys interpreted as the boundary between the solid mantle and the liquid outer core of the earth, when he was unable to find shear waves passing through the core (Jeffreys, 1926). In the same year, Gutenberg proposed a low velocity layer in around 120km depth (Gutenberg, 1926), which remained a topic of discussion for decades (Lehmann, 1961), but is nowadays called the asthenosphere. Inge Lehmann finished the fundamental earth model, when she explained the hitherto inexplicable phase P' (today: PKIKP) with it a high-velocity solid inner core (Lehmann, 1936). The work on a spherically symmetric earth was in principle completed with the huge seismic travel time tables of Jeffreys and Bullen in 1940 (Jeffreys and Bullen, 1940).

The nuclear race and the monitoring of nuclear tests radically changed the discipline. The Vela Uniform project of the Eisenhower administration (Bates, 1961) increased US federal funding by a factor of 30 between 1959 and 1961. Even though this funding was motivated by military considerations, i.e. the estimation of Soviet nuclear strength and the monitoring of underground nuclear tests, it lead to an enormous increase in number and quality of seismic facilities available for research. Seismic arrays, first installed as military facilities improved the signal-to-noise ratio of seismic records and allowed the refinement of travel time tables, partially even by using data from nuclear explosions (Jeffreys, 1962; Wright and Muirhead, 1969). The entanglement with the military-industrial complex lead the discipline slightly astray, when even the leading seismologists of the time demanded several "clean" and peaceful *Megaton* nuclear explosions to reduce uncertainties on seismically inactive regions in the world (Bullen, 1958; Griggs and Press, 1961). In the context of the Vela Uniform project, seven underground nuclear explosions with a yield of 80 kt and less were conducted specifically for the case of seismic monitoring and research. For a very interesting sociological perspective, see Barth (2003).

However, since the interests of the military was to refine source estimation, which was one of the stated goals of the scientific community at that time anyway, seismology in general flourished. The aftermath of Vela Uniform was a huge increase in the number and size of institutes, the World-Wide Standard Seismograph Network (WWSSN), which homogenized the quality of seismic recordings, the first ocean bottom seismometers and large seismic arrays with centralized computer facilities, where for the first time, seismograms were recorded digitally. Especially the latter allowed completely new seismic observations, because it enabled digital filtering and postprocessing of data, which in the end led to the methods applied in this Ph.D. thesis.

The inversion of large sets of seismic travel-times allowed for the first time to produce first regionalized (Dziewoński et al., 1975) models of the earth's mantle.

Together with the advances in numerical prediction of seismic waveforms and computational power first three-dimensional models (Dziewoński et al., 1977; Woodhouse and Dziewoński, 1984; Dziewoński, 1984) of the upper mantle were derived and showed velocity anomalies related to plate subduction. The digital recordings also allowed for the first time an automated calculation of a catalogue of earthquake parameters (Dziewoński et al., 1981) including the moment tensor. At the same time, the automated collection of very large travel time datasets in the International Seismic Catalogue (ISC) allowed to refine spherically symmetric earth models, culminating in the incredibly enduring *Preliminary Reference Earth Model* Dziewoński and Anderson (1981), which - older than the author - is still the reference model for seismology and geodynamics alike.
The explosion of computational power in the last decades brought an huge increase in tomographic studies, which were able to confirm a lot of geological assumptions, especially in the context of mantle convection (van der Hilst et al., 1997) or continental evolution (Ritsema et al., 1999).
Up to the year 2000, tomographic studies were assuming a ray-theoretical model based on the Eikonal equation. It assumes that the travel time of a seismic wave can be defined and measured as the arrival of the first energy in the seismic time series. From that follows that the sensitivity of the travel time to three-dimensional perturbations in the velocity model is confined to an infinitesimally narrow ray path (Kennett, 2001). Two ideas challenged this assumption:

- Full waveform inversion
- Fresnel zone / Fréchet kernels

1.2 State of the art in seismic tomography

The rapid progress in computing power has made it possible to simulate the seismic wavefields of an earthquake with almost arbitrary precision. The preferred method on a global scale is the spectral element method (Komatitsch and Vilotte, 1998), since it combines numerical efficiency with a natural handling of the free-surface boundary condition. With current high-performance computing capacities, it is possible to simulate the complete seismic wavefield in the whole earth for up to 0.2 Hz in a three-dimensional velocity model (with the SpecFEM code presented in Komatitsch and Tromp (2002a)) or even above 2 Hz in an axially symmetric model (Nissen-Meyer et al., 2014). Since meaningful measurements on teleseismic waves rarely exceed 2 Hz, we might assume that any measured information in a seismogram can in principle already be simulated[1]

[1]Unfortunately, the assumption of axial symmetry (or even radial symmetry) is only valid in certain regions of the earth, especially in he lower mantle, which seems to be radially symmetric

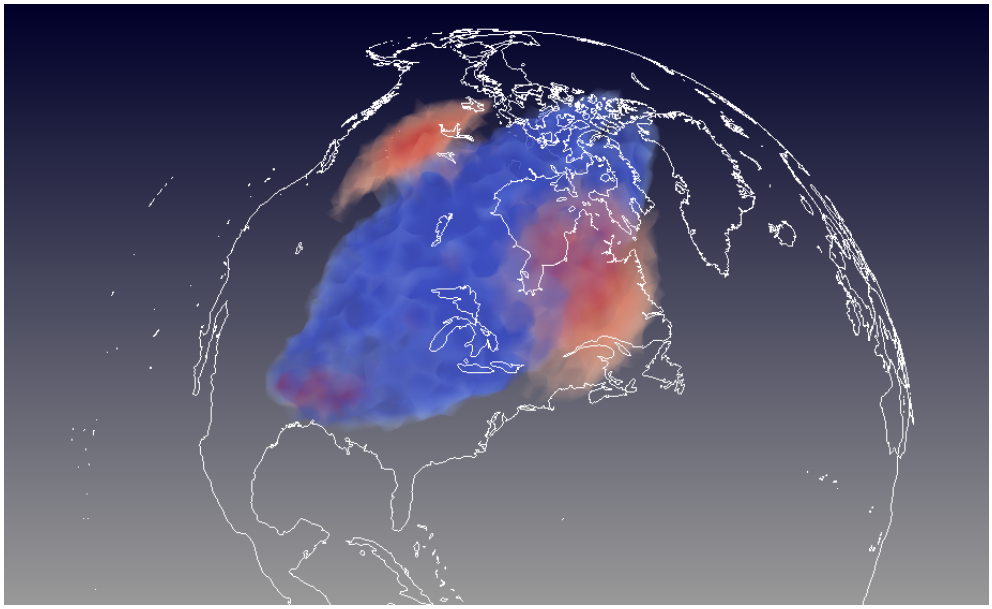

Figure 1.1: Shown is a the volume which affects the recording of a seismic traveltime in northern Mexico for an earthquake in 100 km depth at the north pole. The kernel is calculated in a 20s log-Gabor passband and projected on a global tetrahedral inversion mesh. Shown are only elements with a value of more than 1 per cent of the maximum value of the kernel. Note that the fine structure of the kernel gets lost due to coarse inversion mesh. Nevertheless, it is obvious that a ray approximation would not be sufficient here.

This progress has rendered approximations like ray theory to approximate seismograms unnecessary and has allowed to extract as much information from the seismogram as possible, by fitting whole waveforms instead of just arrival time picks. These techniques are advertised by a plethora of names, but can be mainly divided by two factors: **1. The forward simulation** they use, waveform based or ray-theoretical and **2. the inversion scheme**, which can be iterative-linearised or a one-step-linear inversion. Both have merits and drawbacks, which I want to classify and motivate my selection for this thesis:

linear, ray-based This method formed the bulk of inversions before the paradigm-shift towards banana-doughnut methods. An advantage is that the huge

to a degree of a few percent (Ritsema et al., 2011). The crust is provably very heterogeneous (Bassin et al., 2000; Molinari and Morelli, 2011). The seismic anomalies of the asthenosphere and upper mantle are disputed, but are probably in the range of less than 5% on large scales (Becker and Boschi, 2002). The inner core might be strongly heterogeneous, but the data is yet poorly constrained due to likely modelling errors in the lowermost mantle (Tromp, 2001; Tkalčić et al., 2013).

archive of millions of hand-picked travel-times, which was collected over decades by the ISC can be used.

iterative, ray-based This is somewhat more difficult, since it requires to update the Fréchet-derivatives of the model towards the observables for a new model, one method for which is 3D ray tracing (e.g. Qin et al., 1992; Rawlinson and Sambridge, 2004). This method is preferred for regional studies, where a very heterogeneous velocity structure can be expected and a lot of high-frequency (short-period) recordings are available, for which the infinite-frequency ray approximation has a certain plausibility.

linear, wavefield-based This method calculates the Fréchet derivatives in a spherically symmetric earth model, which allows to the full frequency range of global seismology. The derivations of the true model from this earth model are assumed to be small, so that the problem can be treated as linear. The method was in principle conceived in the late nineties (Marquering et al., 1999; Dahlen et al., 2000), let to considerable controversy, but was applied with roaring success in the following decade to refine existing models of the mantle (Montelli et al., 2004; Sigloch, 2008; Tian et al., 2011), shed new light on the plume debate (Montelli et al., 2006) or reinterpret continental scale tectonic history (Sigloch and Mihalynuk, 2013). The Fréchet kernels for the above-mentioned studies were calculated using ray-theoretical phase delays for different scatterer locations. Nissen-Meyer (2007) proposed to calculate those from the full seismic wavefield and to calculate this in a 3D to 2D reduction strategy valid for spherically symmetric earth models. This has so far not been applied, but preparations for it are part of this thesis.

iterative, wavefield-based An alternative and rather *en vogue* technique goes under names as *Full Waveform Inversion* (Virieux and Operto, 2009), *Full Waveform Tomography* (Fichtner et al., 2011) or *Adjoint tomography* (Tape et al., 2009). Common is a combination of Fréchet derivatives calculated from the full seismic wavefield via the adjoint method and an iterative method (Newton-based or conjugate-gradient) to reduce the objective function (misfit) (Boehm and Ulbrich, 2013). An advantage is that this method allows for a clean and natural strategy to simulate waveforms and directly use the misfit to drive an optimization strategy. A disadvantage is that this strategy has no natural way to infer the uncertainties of the final model. All strategies are based on the Hessian of the misfit in terms of the model (Fichtner and Trampert, 2011), but this assumes Gaussian noise and can only estimate the resolution of the final inversion step and therefore only about the model space close to the final model.

The last and to a smaller extend the third technique are currently gaining most attention in the seismological community, but also in the exploration context. While the idea of a *full waveform* technique, which includes all physics into the simulation seems tempting, it should be objected that this is simply impossible and certain a number of approximations is always necessary. Handling these approximations, like corrections for topography and the crust, consciously, might be more reliable than just increasing the number of free model parameters.

1.3 Objectives of this thesis

The work presented in this thesis aims at improving the possibilities of seismic waveform tomography to resolve structural features in the Earth and to determine the uncertainties thereof. It is based on the linearised approach presented by Sigloch (2008), but tries to address problems found in this work:

1. The kernel calculation method by Dahlen et al. (2000) is only applicable to teleseismic bodywaves which are clearly separated from other phases. These are especially P in a range between 32 and 85 degrees, SH in a range between 32 and 85 degrees, SV between 32 and 60 degrees and PP and SS. Their vertical resolution in the upper mantle is limited, due to the steep angle. It would therefore be beneficial to use regional body waves, which have a better vertical resolution. They can be calculated using the wavefield based method by Nissen-Meyer (2007). Chapter 2 will describe the potential to model triplicated waveforms and to use them for tomography.

2. Seismic tomography uses earthquakes as wave-sources. The source model of the earthquake has a big influence on the estimate of the travel-time misfit and therefore on the inversion itself. The broadband waveform inversion requires a model of the temporal evolution of the earthquake in form of a so-called *source time function*. The estimation of the depth, the moment tensor and the source time function is a non-linear inverse problem. Using a Bayesian inversion scheme described in chapter 3, I inverted for probability density functions of the source parameters.

3. Bayesian inference requires a model of the data variances. The variance of seismological measurements is rather unknown. For the application of probabilistic source inversion, I propose in chapter 4 to estimate the data variance for this specific problem from a large dataset of existing source solutions and employ these variances and covariances in a Bayesian framework.

4. The uncertainty of the estimated travel-time misfits, which are the input parameters of the seismic tomography have hitherto been set to a fixed value or have been estimated heuristically from the signal-to-noise ratio of a seismogram. From the probabilistic source inversion, we can directly estimate the variance of each travel-time and the covariance between all travel-times for one earthquake. Probabilistic traveltime estimations are a completely new dataset for seismic tomographers, which allow a straightforward handling of correlated seismic recordings of varying quality.

Aller guten Dinge sind drei

Wisdom of the German elders, Vol. CLXVII

2

Using triplicated waveforms for tomography

This chapter was published in *Solid Earth* in September 2012 under the title *Triplicated P-wave measurements for waveform tomography of the mantle transition zone* (Stähler, Sigloch, and Nissen-Meyer, 2012)

Abstract

Triplicated body waves sample the mantle transition zone more extensively than any other wave type, and interact strongly with the discontinuities at 410 km and 660 km. Since the seismograms bear a strong imprint of these geodynamically interesting features, it is highly desirable to invert them for structure of the transition zone. This has rarely been attempted, due to a mismatch between the complex and band-limited data and the (ray-theoretical) modelling methods. Here we present a data processing and modelling strategy to harness such broadband seismograms for finite-frequency tomography. We include triplicated P-waves (epicentral distance range between 14 and 30°) across their entire broadband frequency range, for both deep and shallow sources. We show that is it possible to predict the complex sequence of arrivals in these seismograms, but only after a careful effort to estimate source time functions and other source

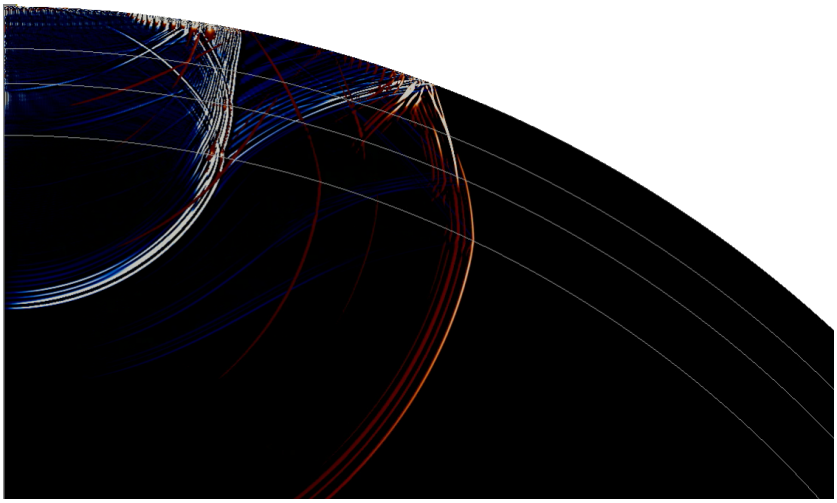

Figure 2.1: Snapshot of the seismic wavefield 100 seconds after an earthquake. Straintrace is in reddish colours and curl in blueish. Three P-wavefronts are visible.

parameters from data, variables that strongly influence the waveforms. Modelled and observed waveforms then yield decent cross-correlation fits, from which we measure finite-frequency traveltime anomalies. We discuss two such data sets, for North America and Europe, and conclude that their signal quality and azimuthal coverage should be adequate for tomographic inversion. In order to compute sensitivity kernels at the pertinent high body wave frequencies, we use fully numerical forward modelling of the seismic wavefield through a spherically symmetric Earth.

2.1 Introduction

The mantle transition zone (MTZ) is of great interest geodynamically, since its properties determine the extent to which material and heat gets exchanged between the upper and lower mantle. In the seismological view, the MTZ extends from the discontinuity at 410 km depth to one at 660 km – both discontinuities are characterized by marked jumps in seismic velocity. The sharpness and topographic undulations of these discontinuities can be linked to mineral physics laboratory experiments in order to infer material properties and mantle rheology.

The seismic waves that sample the MTZ most extensively are regional body waves, i.e., refracted waves that turn within the MTZ. Travelling only moder-

ate distances of $\Delta \approx$1500–3100 km (i.e. 14–29°), these waves are recorded strong and clear on seismic stations, delivering by far the highest signal to noise ratio of any wave type that could be used to study the transition zone. Yet these phases have rarely been used in general, and for seismic tomography in particular, in sharp contrast to teleseismic phases ($\Delta > 30°$). The reason is that these regional waves generate more complex signals than teleseismic ones as they have interacted more extensively with the MTZ discontinuities. Such observations do not lend themselves to abstraction into isolated pulses and the associated, idealized modelling by ray theory. Conversely we may suspect that if we succeed at modelling and inverting these waveforms, we will be able to learn a great deal about the mantle structures that are leaving such a strong imprint on them. Here we demonstrate that this should be possible.

Regional P and S waves are commonly termed triplicated waves, since every interaction with a discontinuity spawns three distinguishable phases. We investigate triplicated P-waves, which occur at epicentral distances of 14° to 29°, and sample the MTZ in some interval halfway between source and receiver. Our aim is to use them in finite-frequency waveform inversion for transition zone structure.

Finite-frequency modelling as originally conceived by Dahlen et al. (2000) is feasible across the entire relevant frequency range of body waves, but has been limited to interpreting direct and reflected teleseismic phases (Montelli et al., 2004; Sigloch et al., 2008; Zhou et al., 2004, 2006; Tian et al., 2011), due to the applicability limitations of paraxial ray tracing for computing sensitivity kernels. Here we present kernels that overcome this limitation. They are obtained from fully numerical forward computations of the seismic wavefield, using the spectral element code of (Nissen-Meyer et al., 2007b). Exploitation of the near-spherical symmetry of the 3-D Earth uses the currently available computational resources very efficiently, allowing access to the entire relevant broadband range of the wavefield (0.03 to 1 Hz), like the original Dahlen method.

Triplicated body waves carry a very strong imprint of their interaction with transition zone discontinuities, which is both an advantage and a challenge. Not only do the triplicated arrivals overlap each other in time, due to the finite-frequency nature of real data, but for shallow earthquakes they additionally overlap the depth phases pP and sP, which get triplicated themselves. Hence an integral part of modelling the waveforms is the careful estimation of source parameters (since they determine the shape of the synthetic Green's function), and of the source time function.

The differential moveout of the triplicated phases has since long been used to derive one-dimensional velocity models(Grand, 1984), which required a large number of seismic stations in a narrow azimuth range. Modelling of individual triplicated waveforms has been successfully used to sample localized het-

erogeneities in the MTZ (Tajima and Grand, 1995; Melbourne and Helmberger, 2002; Tajima et al., 2009). A few studies that included picked arrival times into ray theoretical inversions demonstrated the potential of triplicated waves for tomography (Grand, 2002), but so far they have rarely been used. Only very recently, Zhu et al. (2012) used triplicated phases, amongst others, for a European regional tomography, albeit at lower frequencies.

Regional body waves are complementary to all phases currently used for MTZ studies. Teleseismic body waves also offer good signal-to-noise ratios, but have comparably low sensitivity in the MTZ, which they traverse at steep angles. Hence they constrain the MTZ beneath sources and/or station, whereas triplicated waves sample it extensively midway between sources and receivers. So it would be highly beneficial to combine them in one inversion.

Other methods for sampling transition zone discontinuities have much lower signal-to-noise ratios (SNR). Receiver functions exploit P-to-S or S-to-P converted energy of body waves, which require stacking numerous seismograms. Their migration from the time domain to depth depends on a velocity structure model, which either must have been obtained independently or is neglected, with corresponding systematic errors in the result.

PP and SS precursors, i.e., body waves reflected at the undersides of MTZ discontinuities, have also been used in structural studies, (Shearer and Masters, 1992; Thomas and Billen, 2009; Deuss et al., 2006; Deuss, 2009). Their SNR is low, so that only the rare strong earthquakes that are recorded on seismic arrays can be used. Distinguishing between the signal of an undulated discontinuity and a volumetric velocity perturbation is challenging (Chaljub and Tarantola, 1997), as for receiver functions.

Surface waves have lower image resolution than body waves. Only their higher modes have significant sensitivity to the MTZ, but higher modes carry little energy, and are more difficult to process. Hence surface wave tomography is largely limited to depths above the MTZ.

We start with a discussion of the nature of triplicated body waves, and of their expression in actual seismic broadband data (Sect. 2.2.1). Section 2.2.2 and 2.2.3 demonstrate how we model these waveforms; this covers the computations of Green's functions and the inversion for source time functions and source mechanisms. We then explain the concept of wavefield kernels (Sect. 2.3), and show how passband-filtering to different frequency bands significantly increases the resolution in the transition zone, by comprehensively exploiting information across the entire broadband range (Sect. 2.3.3). The sizeable and well-instrumented continents of Europe and North America currently offer the most favourable source-receiver combinations of criss-crossing regional body waves for tomography. Section 2.4 discusses the two data sets that we have assembled for these two regions, with a focus on the *USArray*. We conclude with a discussion of the

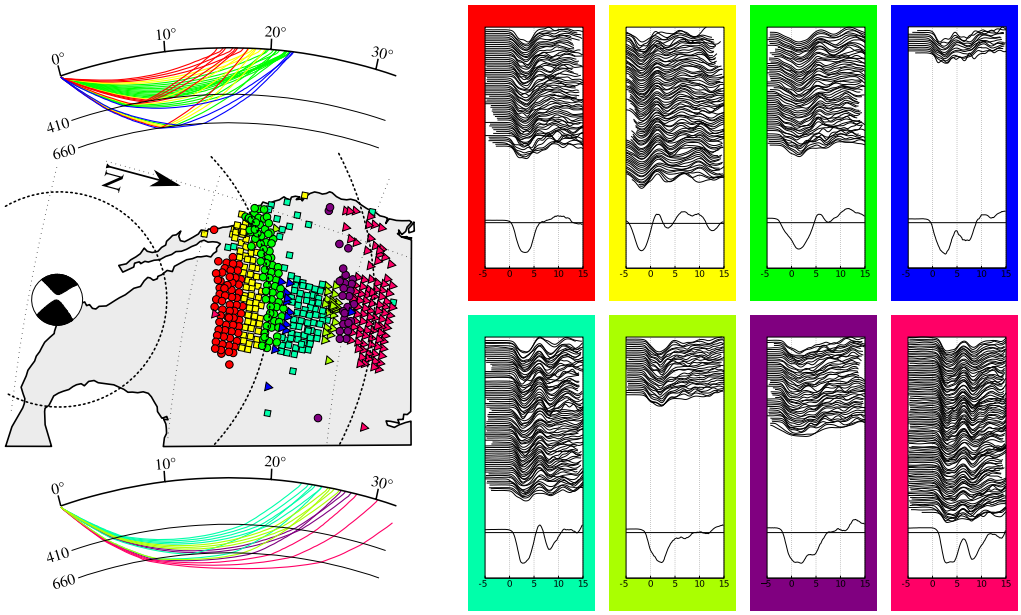

Figure 2.2: Observed waveforms and nominal ray paths of regional P-waves, for a magnitude 6.4 earthquake off the coast of Mexico (2008/09/24 02:33:05, Lat: 17.61 Lon: −105.50, Depth: 6 km). Ray colouring in the left figure corresponds to the colouring of the waveform clusters in the right figure. Our automated clustering algorithm sorts the different kinds of triplicated phases into different groups, based on similarity of the broadband waveforms. The waveform below each seismogram group is the waveform stack. This empirical sorting into groups coincides with the epicentral distance bins predicted by theory (see text for details). This demonstrates that we are dealing with a robust signal that waveform tomography should be able to interpret.

results, and the prospects of inverting these data for MTZ structure (Sects. 2.5 and 2.6).

2.2 Regional P-waves

2.2.1 Triplications

The term *triplication* refers to three seismic wave phases that have similar ray parameters and arrive closely spaced in time. The concept is rooted in ray theory. While our data processing and kernel computations are targeted at interpreting the full waveforms, it is useful to consider their ray theoretical approximation first, in order to appreciate the nature of triplicated waves. It assumes that the

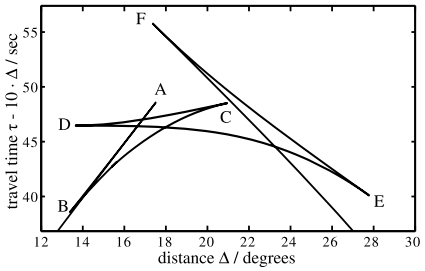

Figure 2.3: Triplication of P-wave traveltimes in *IASP91* (Kennett and Engdahl, 1991). The triplication C to D is produced by the discontinuity at 410 km depth, the one from E to F by the discontinuity at 660 km. The AB triplication originates from the 210 km discontinuity, which is only of second order in *IASP91*. This triplication can hardly be observed, especially since it overlaps with the one from 410 km.

wave from one source to one receiver travels along an infinitesimally narrow ray path, which is described by the eikonal equation (e.g., Kennett, 2001). Strictly speaking, the approximation only holds for the case of a non-dispersive medium. Even when the medium is not intrinsically dispersive, velocity heterogeneities may introduce a frequency-dependent group velocity, which is the motivation for finite-frequency tomography.

In a layered velocity model $c(r)$, the traveltime τ and the angular distance Δ of a direct phase (e.g., a P-wave) depend only on the ray parameter $\wp$.

$$\Delta(\wp) = \int \frac{\mathrm{d}r}{r\sqrt{r^2/(\wp c(r))^2 - 1}} \tag{2.1}$$

$$\tau(\wp) = \int \frac{\mathrm{d}r}{c(r)\sqrt{1 - (\wp c(r))^2/r^2}} \tag{2.2}$$

If the velocity gradient with respect to depth is smooth, τ and Δ increase monotonously with decreasing $\wp$, i.e. stations at a larger distance from the earthquake record the P-phase at later times. If the velocity profile contains strong gradients, or even discontinuities with positive velocity jumps, $\frac{\mathrm{d}\Delta}{\mathrm{d}\wp}$ changes sign, so that rays of smaller $\wp$ arrive closer to the source[1]. Because $\frac{\mathrm{d}\tau(\wp)}{\mathrm{d}\wp} < 0$ in either case, two rays arrive at the same distance at different times. If $\frac{\mathrm{d}c}{\mathrm{d}r} < 0$, $\Delta(\wp)$ is still continuous. The turning points of $\Delta(\wp)$ mark the transition (with decreasing $\wp$) first from a ray travelling above the discontinuity to one being critically reflected at the discontinuity and then to one travelling below it. In the traveltime-distance

[1]The literature does not provide any hard constraints for a triplication to occur. However, it is clear that a discontinuity in $c(r)$ or $\mathrm{d}c/\mathrm{d}r$ will be sufficient.

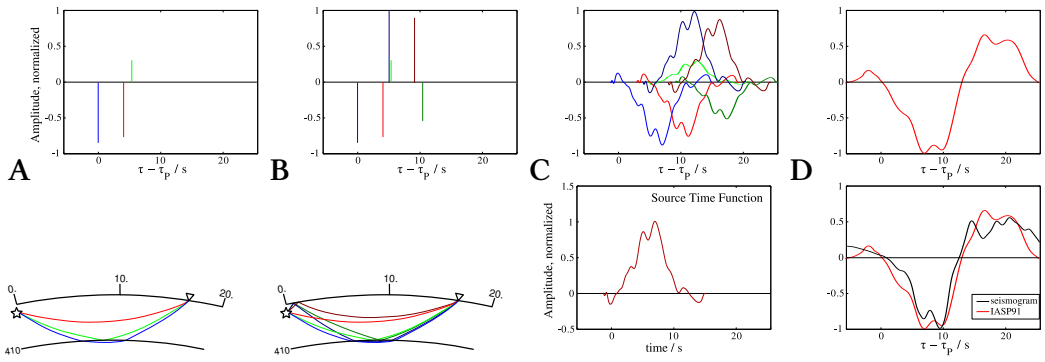

Figure 2.4: Schematic composition of a triplicated broadband P-wave signal: **(A)** Arrival times (top row) and nominal ray paths (bottom row) of the direct P-waves. Three pulses arrive, two of which are refracted above and below the discontinuity (here *410*), and the third reflected by it. **(B)** If the earthquake is shallow, additional depth phases arrive (pP and sP), which get triplicated themselves. **(C)** Real-world seismograms do not resemble sequences of dirac pulses. Rather, the pulses of the Green's functions are dispersed and the source time function (bottom row) convolves into all of them. **(D)** The sum of all contributions is the predicted seismogram (top), which may be compared to the observed seismogram (bottom row), in order to extract measurements for waveform tomography. Even though the waveform is complex, it can be modelled sufficiently well using a layered background model.

relation $\tau(\Delta)$, which is also continuous, a pattern called triplication emerges (Fig. 2.3).

The velocity discontinuities in seismic velocity in the upper mantle (at 410 and 660 km depth in the *IASP91* reference model (Kennett and Engdahl, 1991), henceforth termed *410* and *660*, produce triplications: Neglecting crustal phases and the weakly developed 210-km discontinuity, we receive one P phase up to a distance of 14°, which has travelled through the upper mantle. At 14° another P-phase arrives 8 seconds later (point D in Fig. 2.3), being reflected at the *410*. This branch bifurcates into one reflected path (DC), and one refracted below (DE). The refraction branch continues to 28° distance (E), while the uppermost-mantle branch meets with the reflected one at 21.5° (C) and ends there. From 17.5° (F) on there are also reflection and refraction branches from the *660*. The *660*-reflection branch (EF) meets with the *410*-refraction branch (DF) at 27.8° (E), where they both end. Only the *660* refraction branch can be measured at distances exceeding 27.8°.

With this conceptual knowledge, consider the real data in Fig. 2.2. It shows broadband P-waveforms in a 20 s window, starting 5 s before the first arrival

predicted by *IASP91*. The 692 waveforms from stations in the western United States are aligned (VanDecar and Crosson, 1990) and clustered by similarity as described by Sigloch and Nolet (2006). This clustering results purely from the waveform shapes and does not use meta-information such as station distance or azimuth from the source. The clusters show a clear zonation by distance, caused by the triplications from the transition zone discontinuities. The figure can best be understood by first considering the most distant group of P-waveforms (pink). The stations are mainly located beyond 28° epicentral distance, so that the signal contains no triplications. The secondary pulse, arriving 7 s after the first one, can therefore be recognized as a reflection from the ocean surface near the source (pwP).

In the distance bin closest to the source, from ≈15° to 18° (red), the triplicated phases overlap so that just one broadened pulse arrives. In the second group (yellow), the arrivals are further spread so that a first arriving pulse, a surface reflected phase (at 5 s) and multiple triplicated phases can be distinguished. Additionally, we observe an arrival ≈10 s after the first one, which is a reflection from the *660* (FE branch in Fig. 2.3). In the third group (green), this reflection is already closer to the first arrival, and the first-arriving pulse is a superposition of the DE branch from the transition zone and the BC phase from the upper mantle and depth phases. The next group (dark blue) is quite heterogeneous and marks the transition from *410* triplications to *660* triplications.

In the cyan group, beginning at 22°, the refractions above and below the *660* arrive almost at the same time and collapse into a single pulse. The reflected phase is usually quite weak and not visible at all here. The two clearly separated arrivals hence correspond to P (two overlapping refractions) and pwP (another two refractions). In the next two groups (grass green and purple), the refracted phase from above and below the *660* begin to separate, so that they spill into pwP once more. The most distant group (pink) shows clearly separated P and pwP pulses no longer affected by triplications. The shape of this teleseismic waveform does not change much out to ≈ 85° distance.

Hand-picked arrival times of the different triplication branches have been used in a few tomographic studies (Grand, 1994, 2002), although this approach fails to take into account the finite frequencies of seismic waves. As Fig. 2.2 demonstrates, the triplications are often not clearly separated, due to several factors. The finite duration of the source rupture has a low-passing effect. Earth's intrinsic attenuation disperses the P-wave pulse, which does not contain much energy above 1 Hz. Additionally, waves of a finite wavelength λ are influenced by scatterers off of the direct path, if the detour to reach the scatterer is less than $\lambda/2$, which is the definition of the Fresnel zone. This argument is continued in Sect. 2.3.

2.2.2 Waveform modeling

We download broadband seismograms from the *IRIS* and *ORFEUS* data management centres. The waveforms are corrected are band-passed between 0.01 Hz and 3.5 Hz, de-trended, and transferred to ground displacement by deconvolving the instrument responses. A time window is cropped from 10 s before to 25 s after the theoretical P arrival. Noisy seismograms are singled out by a clustering algorithm and removed manually.

In order to do cross-correlation measurements for waveform tomography, it is necessary to compare a synthetic waveform to the observed seismogram. Synthetic seismograms are calculated using the reflectivity method of Fuchs and Müller (1971). As a reference model we use *IASP91* (Kennett and Engdahl, 1991), together with the density and intrinsic attenuation of *PREM* (Dziewoński and Anderson, 1981).

Fig. 2.4 demonstrates the challenge of modelling regional P-waveforms. Within a short time window, three to five triplicated phases arrive (Fig. 2.4a). If the earthquake is shallow, as most earthquakes are, the surface-reflected phases pP, sP or pwP arrive within a few seconds of P, and are themselves triplicated (Fig. 2.4b). For an earthquake at 20° epicentral distance, ten phases arrive within less than 9 s, triplicated by both the *410* and the *660* discontinuities. The polarity of the reflected phases is negative compared to the refracted phases, and the depth phases may have reversed polarity depending on the source plane orientation. Hence the overall waveform is highly sensitive to the exact depth, mechanism, and distance of the earthquake.

Additionally, the finite duration of the source process is imprinted on the seismogram, which is the convolution of the moment rate function $\dot{m}$, termed *source time function* (STF), with the Green's function $\vec{G}(\vec{r}_\mathrm{s}, \vec{r}_\mathrm{r}, \tau)$. Since duration of the STF is usually of several seconds, it can change the waveform completely.

If the maximum frequency in the seismograms is $f \ll 1/T$, where T is the duration of earthquake rupture, then the source time function is sometimes approximated by a Dirac delta, a triangular function or a Gaussian. This is usually done in surface wave tomography and long-period waveform inversion. We use earthquakes of moment magnitudes between 5.5 and 7.0, where T is between one and several tens of seconds, and we want to invert up to dominant periods of up to 1 s. Hence this approximation is too rough for our purposes, and we need explicit estimates of each STF in order to construct the matched filter.

2.2.3 Source inversion

As seen in the previous section, waveform tomography requires an inversion for the temporal and spatial parameters of the earthquake sources prior to the

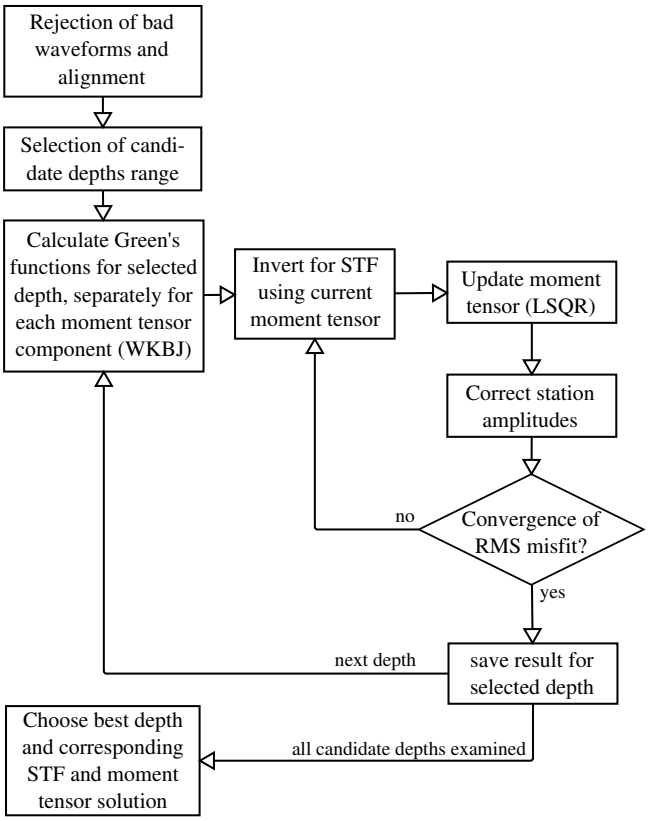

Figure 2.5: Flowchart of the source inversion procedure as described in (Sigloch and Nolet, 2006).

actual tomographic inversion. For the deconvolution of the STF, we use teleseismic P-waves rather than the complex, triplicated regional waves. We briefly describe the procedure here and in Fig. 2.5, for details see Sigloch and Nolet (2006): We remove obviously problematic stations and align all waveforms to the arrival of the P-phase (VanDecar and Crosson, 1990). We then choose a reasonable candidate depth range to survey, 1–50 km for shallow events and *NEIC* depth ± 30 km for deep events. Then we execute the following scheme for each candidate depth: First a joint deconvolution of the synthetic seismograms, calculated with the *NEIC* moment tensor M_0 from the measured seismograms is done, resulting in an STF estimate $\dot{m}(\tau)$. Source orientation is assumed to be constant during the rupture, so that $\dot{m}(\tau)$ is identical for all components of the moment tensor. Second, with this STF, an update for the moment tensor δM is calculated and the amplitudes of all stations are corrected individually. The new moment tensor $M_0 + \delta M$ and the amplitude corrections are used to derive a new

STF estimation and this is repeated, until the RMS misfit between synthetics and broadband seismograms has converged.

After all depths have been treated, we manually choose the depth, at which the RMS misfit is minimal and the STF does not contain any significant negative parts, which would be unphysical. The STF and moment tensor results for this "most likely" depth are retained for kernel calculation and tomography.

The teleseismic Green's functions are calculated by the *WKBJ* code of Chapman (1978), using *IASP91* as reference model. For source inversion we use only waveforms from globally distributed, reliable broadband stations (*GSN* and *Geoscope* networks). For typical earthquakes, around 40 of these stations are located within teleseismic range. Since STF deconvolution is a numerically sensitive operation, we deliberately use only this small, high-quality ensemble, rather than all available broadband stations. The spatial distribution of these permanent, international network stations is relatively even, whereas a deconvolution from all *IRIS* stations would always be dominated by the 1000+ receivers located in North America. Their waveforms and misfits are highly correlated, so that the additional information content with regard to the source is low. However, all available stations will later be used for tomography.

We always attempt to invert for a single STF that fits all global teleseismic data, but in about one out of three earthquakes, we need to allow for two or more regional STF solutions, e.g., when the European station cluster cannot be fit to the same STF as the North American cluster. This may be due to structure close to the source, like a subducting slab or be an effect of source directivity. Our view of a "source time function" is pragmatic: we want it to absorb all signal that is common to all seismograms, even when that signal does not derive from the source rupture sensu stricto. The remaining signal can then be interpreted as an imprint of the structure along the wave-path.

2.3 Sensitivities

2.3.1 Waveform tomography – direct phases

The concept of arrival time of a phase, which may be picked manually by an analyst, assumes a broadband minimum-phased signal. In a heterogeneous Earth, scattering off of the "direct" path adds a small, frequency-dependent component to the direct waveform. Hence scattering introduces a nonlinear dispersion even if the medium is perfectly viscoelastic (Dahlen et al., 2000; Nolet, 2008). This dispersion reflects the scale-dependent interaction of different finite wavelengths with the mantle heterogeneities that we want to image. Hence it embodies the information that waveform inversion captures above and beyond the ray theo-

retical approximation. We measure this dispersion by the method of matched filtering (Sigloch and Nolet, 2006).

A predicted waveform $\vec{u}(t)$ is synthesized from six partial Green's functions $\vec{G}_j(\vec{r}_s, \vec{r}_r, t)$, weighted by the six independent components of the moment tensor M_j, and convolved by the source time function $\dot{m}(t)$. The broadband $\vec{u}(t)$ is immediately bandpass filtered to $\vec{u}_k(t)$, through convolution with a filter response $f_k(t)$ (k is the frequency band index). Hence the finite-frequency synthetic is

$$\vec{u}_k(t) = \sum_{j=1}^{6} \vec{G}_j(\vec{r}_s, \vec{r}_r, t) \cdot \dot{m}(t) \cdot M_j \cdot f_k(t), \tag{2.3}$$

which must be compared to an accordingly filtered observed waveform $\vec{u}^o_k(t)$. For this we parametrize $\vec{u}_k(t)$ by the two observables (misfit measures) that we want to estimate: the traveltime anomaly δT_k and the amplitude anomaly δA_k,

$$\hat{\vec{u}}_k(t) = A_k \vec{u}^o(t - \delta T_k). \tag{2.4}$$

$\hat{\vec{u}}_k(t)$ is the matched filter, and the optimal δT_k, δA_k are obtained by minimizing the RMS misfit between $\hat{\vec{u}}_k(t)$ and $\vec{u}^o_k(t)$. This is equivalent to finding the time shift δT that maximizes the cross correlation between $\hat{\vec{u}}_k(t)$ and $\vec{u}^o_k(t)$.

With this method, we obtain up to $2 \cdot k$ frequency-dependent misfit observables δT_k, δA_k from one broadband P-wave seismogram. The derivative of these misfits with respect to the Earth model can be expressed in so-called *sensitivity kernels* $K_i(\vec{r}_\mathrm{x})$. These represent the sensitivity of the traveltime misfit or the amplitude misfit with respect to changes in P-wave velocity $\Delta V_\mathrm{P}/V_\mathrm{P}$ at a given point $\vec{r}_\mathrm{x}$. The traveltime anomaly δT_k is then modelled as

$$\delta T_k = \int_{\oplus} K_k(\vec{r}_\mathrm{x}) \frac{\Delta V_\mathrm{P}}{V_\mathrm{P}}(\vec{r}_\mathrm{x}) \, \mathrm{d}^3\vec{r}_\mathrm{x}. \tag{2.5}$$

Obviously, this kernel has to be calculated using a reference velocity model. Equation 2.5 and the construction of the kernel K_k contain the assumption that the traveltime anomaly δT_k originates exclusively from single scattering off of anomalies $\Delta V_\mathrm{P}/V_\mathrm{P}$, which quantify the difference between the reference model and true Earth structure. This so-called Born approximation is justified by the observation that the magnitude of lateral mantle heterogeneities $\Delta V_\mathrm{P}/V_\mathrm{P}$ is small, typically on the order of a few percent, so that multiple scattering can be neglected. Kernel K_k is the first Fréchet derivative of δT_k towards $\Delta V_\mathrm{P}(\vec{r}_\mathrm{x})$ (Marquering et al., 1999).

Dahlen et al. (2000) proposed a fast algorithm to derive kernels for teleseismic body waves by paraxial ray tracing. This effectively uses ray theory to go beyond

the limits of ray theory, since it synthesizes sensitivity kernels of finite volume from the interaction of an infinity of rays. The method has been applied to teleseismic body waves with great success (Montelli et al., 2004; Sigloch et al., 2008) and was extended to surface waves (Zhou et al., 2004, 2006; Tian et al., 2011) but its scope is limited to phases without caustics, diffractions or other wave effects (Dahlen et al., 2000; Nissen-Meyer et al., 2007a).

2.3.2 Waveform tomography – arbitrary phases

Triplicated waveforms, with their interactions of refracted and reflected phases around the discontinuity, are not adequately modelled by the ray theoretical formalism. The caustics at turning points A–F (Fig. 2.3) would lead to infinite amplitudes at the corresponding distances. Moreover, the ray-centred approach by Dahlen et al. (2000) works strictly speaking only in a continuous velocity model. Hence we need to calculate the kernels from the full wavefield instead.

Computing the first order perturbation $\delta\vec{u}(t)$ of a seismic waveform $\vec{u}(t)$ involves the wavefield from source to every possible scattering location $\vec{u}\,(t,\vec{r})$, and of the scattered wavefield to the receiver. Thanks to source-receiver reciprocity, this second wavefield may instead be replaced by the back-propagating wavefield $\overleftarrow{u}\,(t,\vec{r})$ from receiver to scatterers, which is generally much cheaper computationally (Nissen-Meyer et al., 2007a, eqn. 10). This is conceptually similar to the adjoint method (Tromp et al., 2005).

$$\delta u = -\int_{\oplus} \left[\delta\rho\,\vec{v}_i\cdot\overleftarrow{v}_i + \vec{E}_{ij}\cdot\overleftarrow{E}_{kl}\delta C_{ijkl}\right] \mathrm{d}^3\vec{r}. \tag{2.6}$$

$\vec{v} = \partial_t\,\vec{u}$ is the velocity field of the forward propagating wave and $\vec{E}_{\,ij} = \frac{1}{2}\left[\frac{\partial\vec{u_i}}{\partial r_j} + \frac{\partial\vec{u_j}}{\partial r_i}\right]$ is the strain tensor. Note that this is index notation, so summation over repeat indices is implied. The arrows serve as a reminder of the forward and backward nature of the wavefields and strains. For an isotropic medium, the dependence on the Lamé parameters is

$$\delta u = -\int_{\oplus} \left[\delta\rho\,\vec{v}_i\cdot\overleftarrow{v}_i + \vec{E}_{ii}\cdot\overleftarrow{E}_{jj}\delta\lambda + 2\,\vec{E}_{ij}\cdot\overleftarrow{E}_{ij}\delta\mu\right] \mathrm{d}^3\vec{r}. \tag{2.7}$$

If the inversion is for δV_P and δV_S rather than for the Lamé parameters $\delta\lambda$, $\delta\mu$, we replace them:

$$\delta\mu = V_\mathrm{S}^2\,\delta\rho + 2V_\mathrm{S}\rho\,\delta V_\mathrm{S} \tag{2.8}$$

$$\delta\lambda = \left(V_\mathrm{P}^2 - 2V_\mathrm{S}^2\right)\,\delta\rho + 2V_\mathrm{P}\rho\delta V_\mathrm{P} - 4V_\mathrm{S}\rho\,\delta V_\mathrm{S} \tag{2.9}$$

Replacing $\delta\mu$ and $\delta\lambda$ in Eq. (2.7), we have

$$\begin{aligned}\delta u &= \\ &- \int_{\oplus} \Big[\delta\rho \left(\vec{v}_i \cdot \overleftarrow{v}_i + \left(V_\mathrm{P}^2 - 2V_\mathrm{S}^2\right) \cdot \vec{E}_{ii} \cdot \overleftarrow{E}_{jj} + V_\mathrm{S}^2 \cdot \vec{E}_{ij} \cdot \overleftarrow{E}_{ij}\right) \\ &+ \delta V_\mathrm{P} \left(2\rho V_\mathrm{P} \cdot \vec{E}_{ii} \cdot \overleftarrow{E}_{jj}\right) \\ &+ \delta V_\mathrm{S} \left(-4\rho V_\mathrm{S} \cdot \vec{E}_{ii} \cdot \overleftarrow{E}_{jj} + 2\rho V_\mathrm{S} \cdot \vec{E}_{ij} \cdot \overleftarrow{E}_{ij}\right)\Big] \, \mathrm{d}^3\vec{r}\end{aligned}$$

Equation 2.10 shows that V_P-kernels are straightforward to calculate because they only involve the diagonal elements of the strain tensor, which is equivalent to the divergence of the displacements: $\vec{E}_{ii} = \frac{\partial \vec{u}_i}{\partial r_i} = \nabla \vec{u}$. Hence for P-wave tomography, we need to store only the displacement field $\vec{u}(\vec{r})$, rather than the full strain tensor $E_{ij}(\vec{r})$. The exact expression of the kernel now depends on the chosen misfit criterion. We prefer the cross-correlation traveltime misfit measured on one component i (in the case of P-waves usually BHZ), defined as

$$\delta T = -\frac{\Re \int_0^\infty \mathrm{i}\omega \overline{u_i(\omega)} \delta u_i(\omega) \mathrm{d}\omega}{\int_0^\infty \omega^2 \overline{u_i(\omega)} u_i(\omega) \mathrm{d}\omega}. \tag{2.10}$$

With $u_i(\omega) = G_{ij}(\vec{r}_\mathrm{s}, \vec{r}_\mathrm{r}, \omega)\dot{m}(\omega)M_j$, we can calculate the sensitivity of δT w.r.t. δV_P. Using the definition of the kernel in Eq. (2.5), we arrive at

$$\begin{aligned}K(\vec{r}_\mathrm{x}) &= \sum_{j=1}^{6} \frac{2V_\mathrm{P}(\vec{r}_\mathrm{x})\rho(\vec{r}_\mathrm{x})}{\int_0^\infty \omega^2 |G_{\mathrm{sr},ij}(\omega)\dot{m}(\omega)|^2 \mathrm{d}\omega} \cdot M_j \\ &\cdot \Re \int_0^\infty \mathrm{i}\omega \, \overline{G_{\mathrm{sr},ij}(\omega)} |\dot{m}(\omega)|^2 \\ &\quad \nabla \vec{G}_j(\vec{r}_\mathrm{x}, \omega) \nabla \overleftarrow{G}_j(\vec{r}_\mathrm{x}, h\omega) \mathrm{d}\omega.\end{aligned} \tag{2.11}$$

The term $|\dot{m}(\omega)|$, which Dahlen et al. (2000) originally denoted as the source term, contains the source spectrum, but also the bandpass filters. $G_\mathrm{sr}(\omega)$, the Green's function from source to receiver, introduces any intrinsic attenuation of the reference Earth model into the kernel.

2.3.3 Spherical Earth kernels

The calculation of a global wavefield at a dominant period of 5 s requires around 10^4 CPUh when a full 3-D forward solver like *SPECFEM* (Komatitsch and Tromp, 2002b) is used. For a realistic iterative global tomography using $> 10^5$ waveforms, the calculation cost would be $\gg 10^9$ CPUh, which is completely prohibitive. In a spherically symmetric background model, this cost can be reduced

10 second dominant period

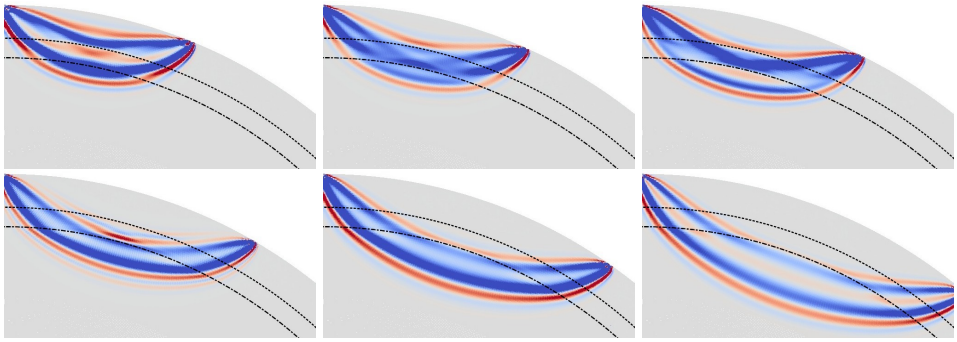

20 second dominant period

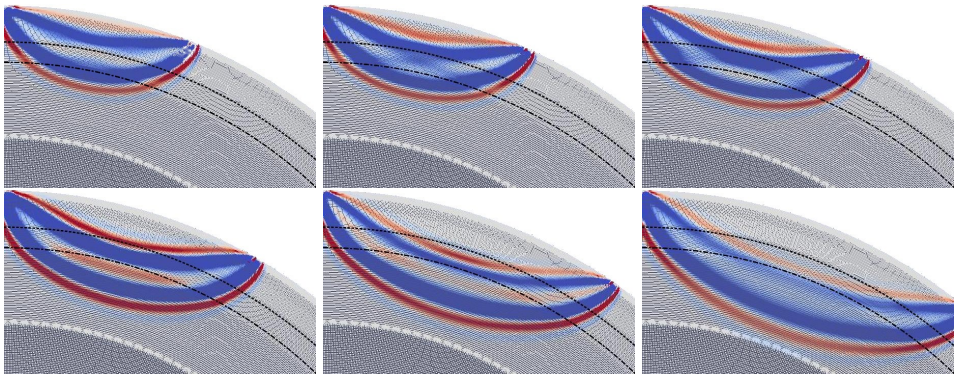

Figure 2.6: Traveltime sensitivity kernels for $\Delta V_P/V_P$, calculated by the Axisem spectral element code. Sensitivities are for a cross-correlation traveltime misfit, in the time window of 5 s before to 15 s after the estimated arrival. Dominant period is 10 s for the upper two rows, and 20 s for the lower two rows. Distances (from top left): 22°, 24°, 26°, 30°, 35°, 40°. Background model: *IASP91*; source: explosion; receiver: z-component. The *410*-discontinuity is marked by the dashed line, the *660* by the dashed-dotted line. Note that most kernels do not feature the famous doughnut hole, which is filled in by the sensitivities to the two discontinuities.

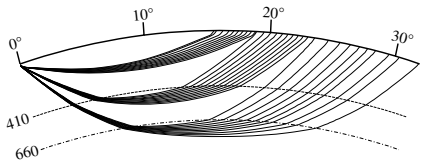

Figure 2.7: Nominal ray paths of first arriving P-waves in *IASP91*. None of the rays bottom out in the lower part of the transition zone. Contrast this to the realistic (finite-frequency) sensitivities of Fig. 2.6, which extend broadly across the entire MTZ.

dramatically: 3-D wavefields in a layered Earth can be computed at the cost of the equivalent 2-D wavefields, since the symmetry implies that one dimension may be calculated analytically (Nissen-Meyer et al., 2007a). Forward wavefields are pre-computed for reasonable depth increments (e.g. increments of 1 km for depths from 0 to 100 km, and increments of 10 km from 100 to 700 km, requiring 160 simulations). The backward wavefield needs to be calculated just once, assuming that all receivers are located at the surface or within one P-wavelength of it. The 160 forward calculations need to be done four times (Nissen-Meyer et al., 2007a, p. 1057) for

1. a M_{zz} monopole source
2. a $\frac{1}{2}\left(M_{xx} + M_{yy}\right)$ monopole source
3. a M_{xz} dipole source
4. a M_{xy} quadrupole source.

Since the response of a station at azimuth ϕ to a M_{xz}-source equals that of a station at $\phi - \pi/2$ to a M_{yz}-source, and response of a $(M_{xx} - M_{yy})$-source at ϕ equals that of a M_{xy}-source at $\phi - \pi/4$, we can reconstruct the response of a spherically symmetric Earth to an arbitrary moment tensor from these four calculations. The backward propagation needs to be done twice:

1. p_z monopole source for the Z-component of the seismogram
2. p_x or p_y dipole source for the E- or N-component of the seismogram

Again, p_x or p_y are equivalent if the receiver location is rotated by $\pi/2$. Using the 3-D to 2-D reduction strategy applied in the SEM-code *Axisem* (Nissen-Meyer et al., 2007b, 2008), the computation cost for a 3-D global wavefield of dominant period $T = 5$ s is around 16 CPUh on an i7 machine, or $\approx 10^4$ CPUh for the entire wavefield library. Since the calculation grows at $O(1/T^3)$, a library of

dominant period 1.25 s would still require less than 10^6 CPUh, which is easily feasible nowadays. From these 642 pre-computed wavefields, kernels for any arbitrary time window in the seismogram can be calculated on the fly in the frequency domain, which is memory intensive but computationally cheap.

Time window choices for these kernels are not limited to any specific phase arrivals or wave types, although it is certainly judicious to chose parts of the seismogram that contain significant seismic energy rather than noise. The window length should be chosen with care. A window that is too long will contain more noise than necessary, and the diameter of the kernel will grow, since longer detours from the direct path are allowed. The outer parts of the kernel will contain the higher-order Fresnel zones, which oscillate rapidly and are unlikely to meaningfully contribute in the inversion. Windows too short will contain too little signal and be more prone to cycle skips. The window length should probably be no shorter than twice the dominant period of the bandpass filter. It will not be possible to calculate kernels separately for each of the triplicated phases, since in real data they overlap in time (cf. Fig. 2.4). However, it is neither necessary or even desirable to revert to this Dirac-type, ray-theoretical way of processing. The kernel formalism ensures the proper interpretation of the waveforms, as long as the actual measurements use the same window lengths and filters as the wavefield computations.

2.3.4 Kernel gallery

A selection of V_P-kernels at dominant periods of 10 s and 20 s are plotted in Fig. 2.6, for an explosive source at the surface and the z-component of the seismogram. Especially at 24° epicentral distance, the two frequency bands differ significantly in their sampling of the MTZ. While the 20 s kernel samples the regions directly below the *410* and the *660*, the 10 s kernel samples mainly the region above the *660*. This is particularly striking when compared to the sensitivity of the first arriving rays (Fig. 2.7), which is completely confined to the region directly below the discontinuities. The 22° and 26° kernels in the 10 s band have nearly complementary sampling characteristics in the transition zone. The 22° kernel is negative where the 26° one has its largest positive values. With dense arrays like the *USArray*, we obtain many 22° and 26° recordings for the same earthquake, which thus should yield good constraints on the MTZ. The 30° to 40° kernels in the second and forth row look more similar to teleseismic kernels, even though clear imprints of the MTZ remain even for a 40° kernel, resulting in an appearance quite different from the 40° kernel of the original Dahlen method (Dahlen et al., 2000). Geodynamically interesting regions just above the discontinuities, where effects of fluid release might be present (Ohtani, 2005), can classically be sampled only by teleseismic waves. Since they traverse the

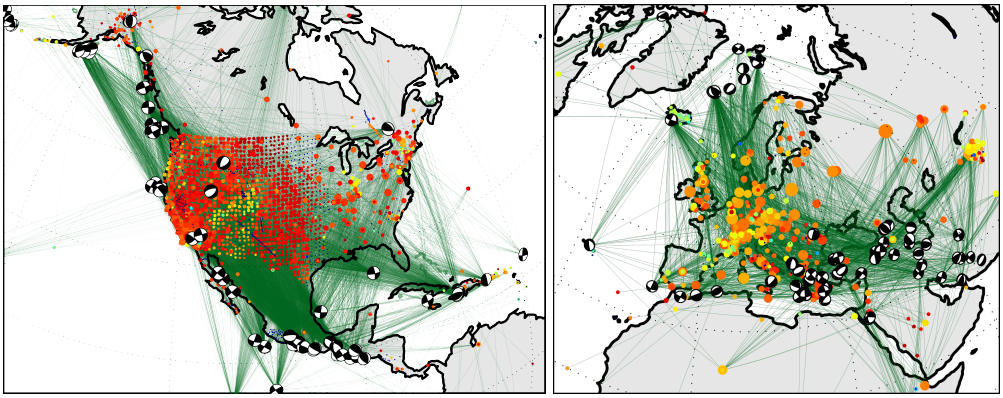

Figure 2.8: Source and stations in two regional data sets for North America and Europe. The rays connect source-receiver combinations at distances between 15 and 35 degrees. Earthquake locations are shown as beachballs. Station colour codes for the goodness of fit between to observed and modelled waveforms at each station. Red denotes median cross-correlation coefficient of $CC_{\max} > 0.8$, which we consider a reasonable threshold for accepting any individual measurement. Orange and yellow colours indicate a lower median fit, which means that only some waveforms at this station may be used. Marker size is proportional to the number of events recorded by the station.

MTZ at steep incidence angles, their vertical resolution is quite limited, in contrast to triplicated phases. Topography on the discontinuities may also influence the waveforms, an effect for which sensitivities may be computed from from the same wavefields (Nissen-Meyer et al., 2007a; Colombi et al., 2012). Ultimately it will be desirable to separate topography effects from those of the volumetric velocity structure, by integrating both kinds of kernels into a joint inversion.

2.4 The data sets

We identified two regions that appear particularly suited to tomography of the transition zone using triplicated body-waves: North America and Europe. They are densely instrumented, decently surrounded by earthquake sources, and large enough for wave paths to penetrate the MTZ on their way from source regions to receivers.

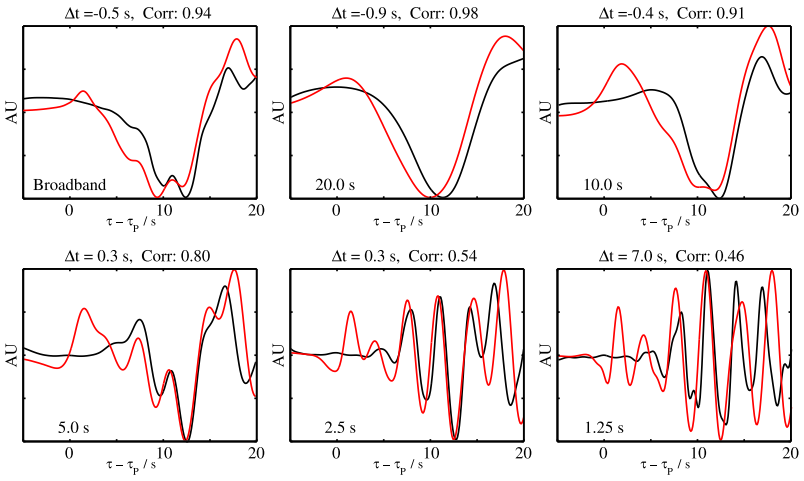

Figure 2.9: The fit between a triplicated P-wave and its synthetic, filtered into frequency pass bands. The epicentral distance is 18.6°, so that the waveform contains triplications from both the *410* and *660* discontinuities. This example uses the same broadband waveforms as seen in Fig. 2.4; the seismic station is VALT (Mount St. Helens crater rim).

2.4.1 North America

Since the advent of *USArray*, North America is clearly the best-instrumented large landmass on Earth. *USArray* stations are spaced by ≈70 km on a regular grid and deliver superb broadband waveforms.

The data from the first year of instalment already brought new insights into the subduction history of the Farallon plate and the formation of the Rocky mountains (Sigloch et al., 2008) or to fluid transport in the Gorda subduction system (Cao and Levander, 2010). The recent move of the deployment into the Great Plains has brought the seismicities of the Guerrero subduction and along the western Canadian margin into distances of 15° to 30°, creating large numbers of crossing paths in triplication range. *USArray* recordings are supplemented by permanent networks in the US, Canada, and Mexico, and by data from temporary experiments. All North American data was downloaded from the *IRIS* data management center (DMC). Currently *IRIS* delivers about 2000 global stations per event, of which ≈1400 are located in larger North America, i.e. between 180° W and 45° W in the Northern Hemisphere.

We found that between 01/01/2001 and 31/12/2011, 92 regional earthquakes generated triplicated P-wave recordings of acceptable signal-to-noise ratio. This yielded 26 016 unique, acceptable wave paths and broadband waveforms in total. We applied Gabor bandpass filters (bandwidth one octave) at centre periods of

Northern American data set

CC_{lim}	0.70	0.75	0.80	0.85	0.90	0.95
20 s	19 897	18 563	16 717	14 225	10 553	5018
10 s	17 646	15 440	12 995	10 124	6317	2143
5 s	12 691	10 331	7900	5452	2861	729
2.5 s	8180	5852	3856	2235	1056	220
1.25 s	3561	2368	1481	773	258	13
total	61 975	52 554	42 949	32 809	21 045	8123
broadband	14 552	12 177	9949	7141	3715	1080

European data set

CC_{lim}	0.70	0.75	0.80	0.85	0.90	0.95
20 s	3450	3161	2840	2423	1891	775
10 s	2953	2477	1922	1261	577	84
5 s	1556	1037	598	264	83	5
2.5 s	882	483	233	91	19	0
1.25 s	277	164	72	29	5	0
total	11 627	9311	7042	4840	2876	886
broadband	2509	1989	1377	772	301	22

Table 2.1: Number of acceptable traveltime measurements in the various frequency bands, as a function of the chosen rejection threshold CC_{lim}. In total 26016 (NA) and 4916 (Europe) broadband seismograms were available.

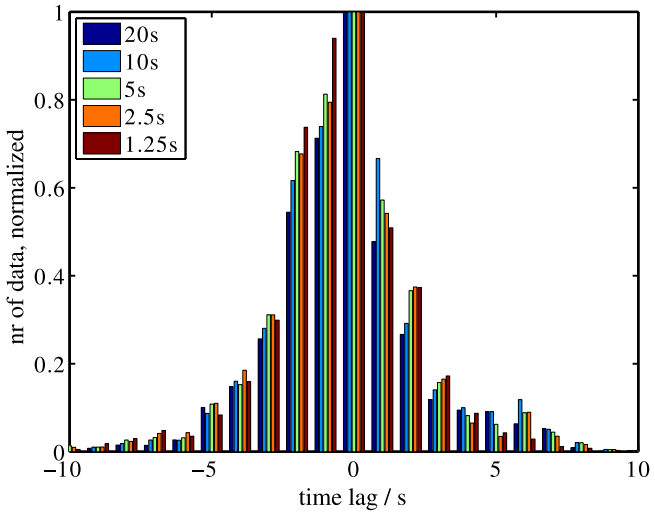

Figure 2.10: Measured traveltime anomalies δT for all paths in the North American data set, in all five frequency bands (distinguished by colour). Only data whose fit exceeds $CC_{\max} > 0.8$ are plotted. The histograms are normalized so that at $\delta T = 0$, each bar has value 1.

20 s, 10 s, 5 s, 2.5 s, 1.25 s. Since we make cross-correlation measurements, the correlation coefficient between observed (filtered) waveforms and their synthetics using *IASP91* serves as the primary measure of goodness of fit. We denote by δT the time shift that maximizes the cross-correlation between observed seismogram and matched filter as in Eq. (2.4), and by $CC_{\max}$ the correlation coefficient at this optimum time shift. Hence $CC_{\max}$ acts as a quality measure, and δT is the actual finite-frequency observable to be interpreted by tomography. Previous experience (Sigloch and Nolet, 2006; Sigloch, 2008) lets us assume that $CC_{\lim} \geq 0.8$ is a good threshold for acceptance. If we only accept filtered waveforms with $CC_{\max} \geq 0.8$, 42 949 out of 130 080 remain (Table 2.1). Fitting waveforms in the five separate frequency bands thus increases the number of usable data more than fourfold, compared to fitting only the broadband seismograms. In particular, we can often accept at least one passband measurement even when the $CC_{\max}$ of the broadband measurement is clearly too low – this salvages many important wave paths. For teleseismic waves, another frequency band below 20 s might reasonably be added, but for regional P-waves this is less interesting, since the 20 s kernels already fill up the entire depth range of the transition zone (see Fig. 2.6).

Figure 2.9 shows a comparison between matched filters and real waveforms for the seismograph station at Mount St. Helens crater, which is by no means an ideal station. Still three out of five bands have $CC_{\max} > 0.8$ and could contribute to tomography. These seismograms were calculated using *IASP91* velocity model.

For an actual tomography of Northern America it may be beneficial to calculate matched filters and kernels in a regional 1-D model; for a recent model and a comparison between previous results see Chu et al. (2012).

Figure 2.10 shows that the average absolute traveltime anomaly δT is similar in all bands, with a standard deviation of $\approx$2.4 s. From our experience with teleseismic P-waves, we know that a large part of this δT signal is due to mislocated sources rather than to mantle heterogeneity; both contributions are jointly inverted for by our tomography software.

These δT measurements on triplicated data will be embedded into a larger data set of teleseismic P-wave data (Sigloch, 2011). The latter have better azimuthal coverage, since they include earthquakes from the east (mid-Atlantic ridge and southern Europe). Unfortunately, very few seismic sources east of North America are located at regional distances.

2.4.2 Europe

Compared to North America, the European seismic networks are less homogeneous, even though the *NERIES* initiative brought a great advance. We downloaded our waveforms from the *ORFEUS* DMC. This archive currently contains around 400 seismic stations, mainly in Europe, but also several temporary installations by European agencies, e.g. in Indonesia. Figure 2.8 shows that data coverage is quite uneven. Several large countries like France and Poland are sparsely instrumented, other networks do not share their data yet. There have been several large temporary installations in Central Europe and Scandinavia, data which would be very interesting but are being released only slowly. The *IRIS* DMC holds hardly any broadband stations above and beyond the *ORFEUS* DMC. On the other hand, the geometry and seismicity of Europe is more favourable than for North America. Hellenic seismicity is recorded over a large azimuthal range from Spain to Russia and produces many crossing paths, together with Western Mediterranean seismicity recorded in Central Europe, and seismicity on the North Atlantic ridge between Iceland and Svalbard. One of the most interesting features in the transition zone are the slab remnants below the Northern Balkans and the Carpathians, which cannot be easily connected to the established subduction regimes. Sampling of the MTZ by triplicated waves is very good in this region, and should help in further illuminating its mantle processes. A clear difference to the North American data is that few earthquakes above magnitude 6 are recorded in Europe. Since we obtain best correlations between data and synthetics at around magnitude 6.5, the data quality is generally lower than in North America. In total, the number of available stations in larger Europe (defined as the region between 45° W and 75° E in the northern hemisphere) is 390. Our dataset contains 66 earthquakes, which recorded 4916 broadband seismo-

grams (unique wave paths). 7042 out of 24 580 passband measurements have a data-synthetic fit that exceeds $CC_{\max} > 0.8$. Compared to the North America, we obtain about five times fewer waveforms, and seven times fewer acceptable δT measurements. This lower average signal quality seems to be mainly due to the weaker seismicity around Europe.

2.4.3 Information content of triplicated P-waveforms

Before embarking on tomographic inversions, we want to convince ourselves that triplicated waveforms do indeed contain coherent and usable structural information. The broad footprint of *USArray* may be sliced up into dense seismic profiles at various back-azimuths, each featuring dozens of stations. Here we consider one such quasi linear section, generated by an earthquake from Guerrero, Mexico. Figure 2.11 shows the P-waveforms of 84 displacement seismograms in a range between 22 and 35° distance. The traces are color coded, where green means zero displacement, blue is negative displacement, and red is positive. Traces are time-aligned on the *IASP91*-predicted arrivals of the first P-phase.

The first arrival in the real seismograms occurs around +2 s for all traces, a systematic bias w.r.t. to *IASP91* that is most likely due to source mislocation. The blue triangular move-outs (e.g. to +7 s at 21° distance) are the triplicated phases of P. Starting at +10 s, the whole P-arrival sequence is "echoed" (also in blue) – this is the depth phase pP, in itself triplicated, for this shallow event (12 km deep).

If the Earth were truly spherically symmetric, the P-arrivals would be aligned smoothly – if not along a vertical line of $t = 0$, then along some other smooth line of steep move-out. This is clearly not the case, signalling the kind of lateral mantle heterogeneity that seismic tomography targets. Strong unevenness is for example observed between 25 and 31° distance, where the P-onset varies between 0 s and +3 s.

The largest delays are present between 29 and 31° distance. This might be explained by a low-velocity anomaly directly below the *660*, since only waves of this distance range bottom there (see Fig. 2.7). Recordings at more distant stations would be less influenced by this hypothetical anomaly, since they traverse it at a steeper angle, with correspondingly lower sensitivity. However, a second observation leads to another explanation: The second triplication (here arriving at ≈5 s at 28°), represents the phase bottoming directly above the *660*. According to *IASP91*, it should be recorded only to a distance of 27.8°, but here we observe it to distances exceeding 29°. This could be explained by a depression of the 660-km discontinuity to a depth of 680 km, which would also explain the delay of the first phase at this distance. A depressed *660* in this region of subduction is plausible, since the lower temperatures of the slab would shift the phase transition to

higher pressures and deeper depths. Indeed, studies from SS precursors Houser et al. (2008) showed a *660* depressed to 668–671 km in Northern Mexico.

The second subplot of Fig. 2.11 shows several stations at 28 to 29° distance, where the second triplication should not be recorded. We do observe the phase, but only at some of the stations (at +4 to +5 s), which suggests that the depression of the *660* is quite localized. From the azimuthal spread of the stations, we can estimate their bottoming points to be spaced only by tens of kilometres, and yet the imprint of the *660* in the seismograms is quite variable. Since the maximum frequencies in these waveforms are less than 1 Hz, the scale of the undulations on the *660* must be close to the resolution limit of these waves. The aforementioned precursor study lacked the resolution to resolve such small features.

2.5 Discussion

Using triplicated P-waves fills an important gap in waveform tomography. Teleseismic waves have relatively poor depth resolution in the MTZ, and little sensitivity to the discontinuities themselves. Since regional waves have this resolution, we hope to greatly increase the resolution of future P-wave models in the transition zone. So far, triplicated body waves have hardly ever been used for tomography, since they are not well modelled by classical ray theory. The appearance of the actually measured waveform has a clear finite-frequency character rather than resembling a sequence of Dirac pulses.

Our choice of misfit criterion is the cross-correlation traveltime – effectively a phase shift measurement, given our relatively narrow pass-bands. Cross-correlation is the optimal strategy for the detection and estimation of a known signal (the synthetic waveform or "matched filter") in a noisy version of the same signal (the measured waveform), where the noise is assumed to be white additive Gaussian noise in each passband. Intuitively it might seem that cross-correlation may not be a suitable misfit for triplicated waves, since for all but the highest frequencies, the time window will necessarily encompass all three triplicated phases, each of which has different spatial sensitivity. Hence calculating one traveltime delay on all three overlapping phases may seem unphysical. We believe that this understanding of the cross-correlation misfit is misguided by (ray-theoretical) intuition. While it is true that one cross-correlation applied to a broadband signal only calculates one delay time for the whole broadband time series, this is actually not what we propose to do. When splitting the signal into multiple frequency bands k and calculating separate δT_k, several, ideally independent measurements are done on the waveform. The corresponding sensitivity kernels describe the sensitivity of the model towards each of these measurements. It does not describe the sensitivity towards the traveltime of one particular (ray-theoretical)

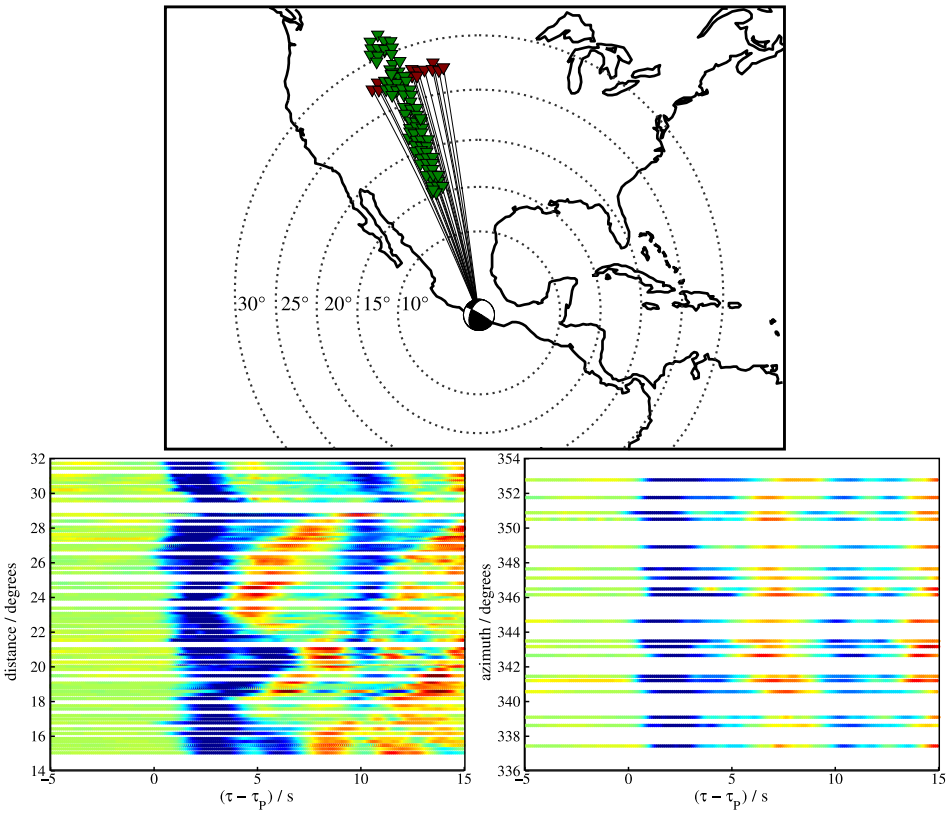

Figure 2.11: Evidence of 3-D structural information contained in triplicated P-waves. Top: we extract a quasi 1-D profile of 84 *USArray* stations, recording an earthquake in Mexico (Event: 2009/04/27 16:46:28, Mag: 5.8, Lat: 17.03, Lon: −99.45, Depth: 35 km). Middle: Section of broadband seismograms at triplication distances (between 22 and 35°, green in the map plot). Z-component, colour coded, green is zero displacement, blue negative, red positive. The traces are normalized separately, and aligned to the first arriving P-wave as predicted by *IASP91*. See text for discussion. Bottom: Seismograms from the ensemble of stations at quasi-constant distance of 28 to 29° (red triangles in map plot). The second P-triplication is observed on some of the traces (at t = 4–5 s) but not on others, pointing to variations on the 660-km discontinuity.

phase. The kernel computation formalism ensures that the proper sensitivity for each window and filter is computed, whatever they may be, meaning a time window containing triplicated waves can be used just as any other time window. One should just not expect a ray-theoretically intuitive meaning corresponding to each measurement.

The calculation of full wavefields in a laterally heterogeneous 3-D Earth model is still prohibitively expensive for frequencies above 0.05 Hz. Hence waveform tomography must currently choose between one of two compromises:

1. In a laterally heterogeneous Earth model, calculate low frequency wavefields (< 0.05 Hz), since high frequencies are not affordable. This means focusing on surface waves and the low-frequency part of body waves. Due to the large wavelengths of body waves, their low-frequency part offers little resolution in the mantle transition zone (already at a dominant period of 20 s, the kernel fills the entire transition zone). The high cost of wavefield calculations mandates that they need not be done too often. The adjoint method proposed by Tarantola (1984), and applied in continental-scale seismology by Tromp et al. (2005), Fichtner et al. (2009) and Zhu et al. (2012), offers an efficient solution by calculating wavefields only once per source, resulting in composite, so-called event kernels, which indicate the descent direction for the (linearised) gradient search. Several iterations are possible and customary, since wavefields can be computed in arbitrary Earth models, in particular also the updated ones.

2. In a spherically symmetric Earth model, calculate kernels that span any or all parts of the seismically relevant frequency spectrum. This broadband capacity has defined "finite-frequency tomography" since Dahlen et al. (2000). Nissen-Meyer et al. (2007b) showed that full wavefield kernel computations are feasible for frequencies up to 1 Hz, due to the extreme computational savings that result from smart exploitation of the spherical symmetry. The use of high-frequency waves promises accordingly higher image resolution. The method is so efficient that all source-to-receiver kernels are explicitly calculated, turning the problem into one of matrix inversion, for which powerful analysis concepts and computational tools are well known. The disadvantage is that several iterations are not possible, since the Earth model would lose its spherical symmetry after the first update. This might be a serious drawback in media with heterogeneity of strong magnitude, where the single-scattering (Born) approximation starts breaking down, but where several linearised iterations might still lead significantly closer to the global misfit minimum than a single one.

We believe that the finite-frequency approach is currently better suited to tomography of the upper mantle and the transition zone, since (a) being able to use the highly resolving body waves across their entire frequency range should be a big advantage, and (b) all previous studies let us expect only relatively weak perturbations from a layered background model like *IASP91*, on the order of a few percent, so that the single-scattering approximation should be completely adequate.

A global reference model may not be best suited for a regional study. Rather, careful selection of a suitable regional reference model is a crucial step of a tomography.

We note that the mixed use of forward modelling codes (*WKBJ*, reflectivity method) has historical reasons and reflects an unfinished (though functional) stage of development. Ultimately all steps will be carried out with the most complete method, Axisem. For inversion of source time functions from teleseismic data, *WKBJ* has been an efficient tool since (Sigloch and Nolet, 2006). It is completely adequate for teleseismic waves, and this STF inversion step is treated as independent from the modelling of triplicated waveforms. Reflectivity is used for efficient forward modelling of the triplicated broadband seismograms (*WKBJ* cannot easily compute triplicated phases, and Axisem is not yet set up to do true broadband computations efficiently for the number of computations needed). In order to compute sensitivity kernels, the full wavefield is needed, and we obtain it from full numerical forward modelling using Axisem (but not yet routinely up to frequencies of 1 Hz).

Analysis of triplicated waveforms has so far been mostly applied to deep events (Tajima and Grand, 1995; Tajima et al., 2009), in order to separate the influence of the discontinuities from the depth phases. We have shown that shallow events can be modelled when source parameters are carefully estimated. Routine catalogue estimates (Global CMT (Dziewoński et al., 1981) or NEIC) do not deliver all the parameter we need (source time function), or not to the required accuracy (e.g., source depth).

However, using our own source inversion results from teleseismic P-waves, we can model the sources sufficiently well for our purposes. The ability to use shallow earthquakes enlarges the data base enormously, since most earthquakes occur shallower than 30 km depth. In particular, good tomographic resolution requires good azimuthal coverage by sources, but few regions on Earth are surrounded by subduction zones to generate deep earthquakes from all directions.

The regional data sets are promising, both for North America and for Europe. They will be seamlessly embedded into a global inversion that also contains teleseismic P-wave measurements Sigloch (2011). A regional tomography of Europe can thus still benefit from events in eastern Asia, i.e. beyond the triplicated range. Hence the fact that the regional seismocity around Europe is weaker than

in North America, is compensated by the superiour azimuthal coverage at teleseismic distances. Nevertheless, the European network is nowhere as dense as the *USArray*, which will make any American mantle structure far better resolved in the foreseeable future. Average waveform cross-correlation is poorer in the European data set than in the North American one. Three possible explanations come into mind:

1. Station quality might be lower. We do not believe this is generally the case, even though the average distance to the nearest coast is smaller in Europe than in North America.

2. European mantle structure could be more complicated than under Northern America, generating a larger mismatch between observed and modelled waveforms. The tectonic history of Europe is often thought to be more complex, but tomographic studies since the advent of *USArray* have also revealed very heterogeneous mantle structure under North America (Pavlis et al., 2012; Becker, 2012). Hence it is unlikely that the true seismic velocity structure in the mantle under Europe deviates significantly more from a layered model than under North America.

3. Earthquake sources around Europe may be less suited. We think this is the main issue. In North America, we can use rather strong strike-slip events along the west coast, and numerous deep events along the Guerrero subduction zone, many of them exceeding magnitude 6. European seismicity is weaker in magnitude and tends to consist of complicated events in the Aegean subduction and along the Anatolian fault; strike-slip events along the Atlantic ridge are rather weak. Since some of these events are not contained in the *IRIS WILBER* archive and thus only the *ORFEUS* stations were available to us, our source inversion for them might be more error prone as well.

The seismic section from the Mexican earthquake demonstrates the high signal quality of *USArray* recordings (Fig. 2.11). The discussed strong imprint of a depressed *660* in this signal shows that we may need to be careful to properly parametrize the inversion such that depressed or elevated discontinuities are detected and become part of the tomography result, rather than smearing into bulk velocity structure. In order to separate the two effects, we are considering the use of boundary topography kernels (Colombi et al., 2012), in addition to the volumetric velocity kernels shown in Fig. 2.6.

2.6 Conclusion

We conclude that regional body waves should be usable and useful for waveform tomography. We plan to invert these data using finite-frequency tomography and kernels from full numerical wavefield computations (Nissen-Meyer et al., 2007b), but our conclusions about the nature of the data have broader validity.

After careful deconvolution of the source time function and other source parameters from teleseismic waveforms, we obtain good cross-correlations between observed and modelled triplicated seismograms, across the broadband range and even for shallow sources. Due to the much more complex nature of the waveforms, these fits are lower than what we obtain for teleseismic P-waves, but are still sufficient to assemble two decently sized tomography data sets for North America and Europe. The inclusion of these data greatly increase and complement the sensitivity to transition zone structure, and in particular to the discontinuities at 410 km and 660 km, which so far must be investigated using waves of far lower signal-to-noise ratio. The abundance and high quality of data from *USArray* make the transition zone under North America the natural target for a first waveform inversion using triplicated P-waves.

2.7 Further reading

In the compilation of this work, further articles were consulted, which have not been cited explicitly so far: (Fukao, Obayashi, and Nakakuki, 2009; Müller, 1985; Ringwood, 1975)

So ist das Leben eben,
es muss Beben geben.

Seeed, in: Tide is High

3

Probabilistic seismic source inversion

This chapter was published in *Solid Earth Discussions* in July 2013 under the title *Fully probabilistic seismic source inversion – Part 1: Efficient parametrisation* (Stähler and Sigloch, 2013)

Abstract

Seismic source inversion is a non-linear problem in seismology where not just the earthquake parameters themselves, but also estimates of their uncertainties are of great practical importance. Probabilistic source inversion (Bayesian inference) is very adapted to this challenge, provided that the parameter space can be chosen small enough to make Bayesian sampling computationally feasible. We propose a framework for PRobabilistic Inference of Source Mechanisms (*PRISM*) that parameterises and samples earthquake depth, moment tensor, and source time function efficiently by using information from previous non-Bayesian inversions. The source time function is expressed as a weighted sum of a small number of empirical orthogonal functions, which were derived from a catalogue of > 1000 STFs by a principal component analysis. We use a likelihood model based on the cross-correlation misfit between observed and predicted waveforms. The resulting ensemble of solutions provides full uncertainty and covariance information for the source parameters, and permits to propagate these source uncertainties into travel time estimates used for seismic tomography. The computational effort is such that routine,

global estimation of earthquake mechanisms and source time functions from teleseismic broadband waveforms is feasible.

3.1 Introduction

Seismic source inversion is one of the primary tasks of seismology, and the need to explain devastating ground movements was at the origin of the discipline. The interest is to locate the earthquake source using seismogram recordings, and to combine this information with geological knowledge, in order to estimate the probability of further earthquakes in the same region. This purpose is served well by a variety of existing source catalogues, global and regional. Large earthquakes and those in densely instrumented areas are being studied in detail, using extended-source frameworks like finite-fault or back-projection.

Smaller earthquakes ($M_S \leq 7.5$), and especially remote events with sparse data coverage, are better parameterised by a point source. Most catalogues determine only a location and a moment tensor solution, which often allows for identification of the associated fault. But the waveform data contain additional information: for earthquakes exceeding $M_S \geq 5.5$, it is generally possible to invert for the temporal evolution of the rupture, described by a time series called the source time function (STF) (Ruff, 1989; Houston, 2001; Sigloch and Nolet, 2006). While the STF may further aid the understanding of fault characteristics and hazard or the interpretation of an event in a mining context (Gibowicz, 2009), our primary motivation for estimating it is a different one: the STF convolves the broadband Green's function and strongly affects its waveform. Waveform tomography estimates three-dimensional earth structure by optimising the fit of observed to predicted waveforms, but at high frequencies (e.g., exceeding 0.1 Hz), such fits can only succeed when the source time function is incorporated into the predicted waveform (Sigloch and Nolet, 2006; Stähler et al., 2012). Hence the purpose here is to develop an automated procedure to routinely estimate broadband source time functions and point source parameters from global seismogram recordings, including a full treatment of parameter uncertainties.

A few recent catalogues now include STF estimates (Vallée et al., 2011; Garcia et al., 2013), but the treatment of parameter uncertainties is still incomplete. Uncertainties in the STF correlate most strongly with source depth estimates, especially for shallow earthquakes (Sigloch and Nolet, 2006), where surface-reflected phases (pP, sP) inevitably enter the time window for STF estimation (see Fig.3.1). Inversion for the STF and the moment tensor is linear, whereas inversion for depth is inherently non-linear. Hence gradient-free optimisation techniques like Simulated Annealing (Kirkpatrick et al., 1983) or the first stage of the Neighbourhood Algorithm (Sambridge, 1999a) have become popular; Table 3.4 presents an

overview of gradient-free source inversion algorithms from recent years. These optimisation algorithms provide only rudimentary uncertainty estimates.

A natural alternative, pursued here, is Bayesian sampling, where an ensemble of models is generated. The members of this ensemble are distributed according to the posterior probability density $P(\vec{m})$, where $\vec{m}$ is the model parameter vector to estimate. Integrating over certain parameters of this joint posterior $P(\vec{m})$, or linear combinations thereof, yields marginal distributions over arbitrary individual parameters or parameter combinations. To the best of our knowledge, ensemble sampling in the context of source parameter estimation has been tried twice so far (Wéber, 2006; Dębski, 2008), and has been limited to a few events in either case.

A hurdle to using sampling algorithms has been the efficient parameterisation of the source time function. We propose a parameterisation based on empirical orthogonal wavelets (Sect. 3.2.1), which reduces the number of free parameters to less than 12 for the STF, and to around 18 in total. We show that this makes Bayesian sampling of the entire model space computationally feasible.

A normalised moment tensor is sampled explicitly, and the scalar moment and absolute values for M_j are derived from the amplitude misfit (Sect. 3.2.2). Section 3.3 introduces Bayesian inference as a concept and explains the model space and prior assumptions. The ensemble inference is done with the Neighbourhood Algorithm (Sambridge, 1999a,b). In Sect. 3.4, the code is applied to a magnitude 5.7 earthquake in Virginia, 2011. Section 3.5 discusses aspects of our algorithm and potential alternatives. We compare to related studies by other workers in Sect. 3.5.4 and in the appendix.

Our procedure is called *PRISM* (PRobabilistic Inference of Source Mechanisms), by applying it routinely, we plan to publish ensemble solutions for intermediate-size earthquakes in the near future. A usage of uncertainty information gained from the ensemble is demonstrated in Sect. 3.4.3, where the influence of source uncertainties on tomographic travel time observables is estimated. Further investigations of noise and of inter-station covariances are presented in a companion paper (Stähler et al., 2014).

3.2 Method

3.2.1 Parametrisation of the source time function

Source time function (STF) is a synonym for the moment rate $\dot{m}(t)$ of a point source, denoting a time series that describes the rupture evolution of the earthquake. It is related with $u(t)$, the vertical or transverse component of the dis-

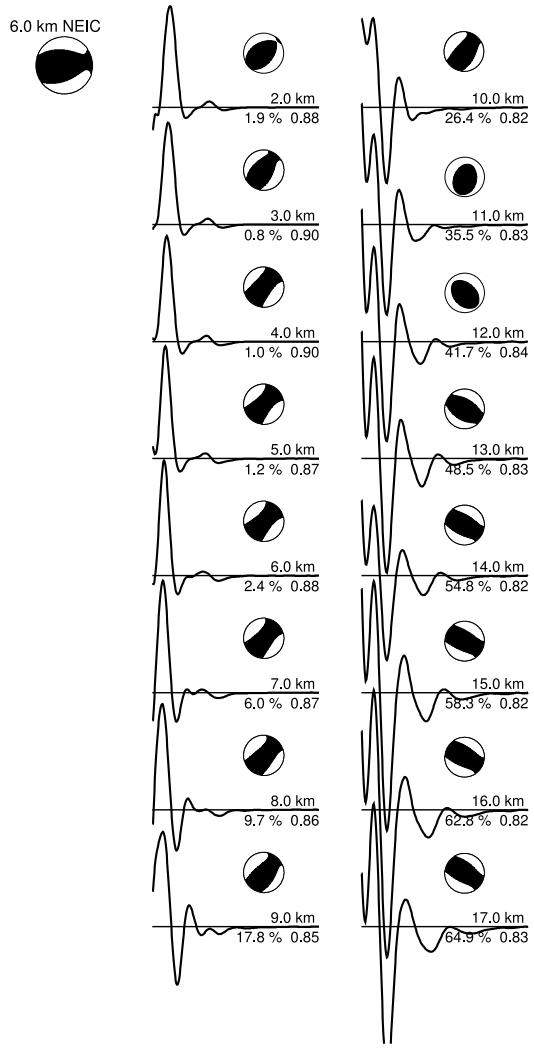

Figure 3.1: Source time function solutions for a $M_W 5.7$ earthquake in Virginia, USA (2011/08/23) obtained from joint inversion for STF and moment tensor $\vec{M}$, using the iterative linearised optimisation algorithm of Sigloch and Nolet (2006). Trial source depths ranged from 2 km to 17 km, in increments of 1 km, and each deconvolution was based on the same 86 broadband, teleseismic P-waveforms. Note the strong changes in STF and moment tensor as a function of depth. Top left shows the moment tensor solution from the NEIC catalogue for comparison. For every candidate solution, the percentage of "non-negative" energy is given, a proxy for how oscillatory (and thus inherently non-physical) the solution is. The third number gives the average cross-correlation coefficient between observed and predicted waveforms achieved by each solution. At depths between 2 and 7 km, the STF is pulse-like, simple, non-negative, and waveform cross-correlation attains its maximum, signalling the most likely depth range for this event. The present study offers an approach to quantify these qualitative trade-offs and judgements.

placement seismogram observed at location $\vec{r}_\mathrm{r}$ by convolution with the Green's function:

$$u(t) = \sum_{j=1}^{3} \sum_{k=1}^{3} \frac{\partial G^j}{\partial x_k}(\vec{r}_s, \vec{r}_\mathrm{r}, t) * s(t) \cdot M_{j,k} \tag{3.1}$$

where ; $s(t) \equiv \dot{m}(t)$ is the STF; $M_{j,k}$ denotes the elements of the symmetric, 3×3 moment tensor, **M**; and $\mathbf{G}(\vec{r}_s, \vec{r}_\mathrm{r}, t)$ is the Green's function between the hypocenter $\vec{r}_s$ and receiver location $\vec{r}_\mathrm{r}$.

Due to the symmetry of **M**, we can reduce eq. 3.1 to a simpler form:

$$u(t) = \sum_{j=1}^{6} g_l(t) * s(t) \cdot M_l, \tag{3.2}$$

where M_l are the unique moment tensor elements and g_l are the respective derivatives of the Greens function. The elements g_j are no 3-D vectors because we compute either only its vertical component (for P waves) or its transverse component (for SH waves). In either case, $\vec{g}$ is a superposition of six partial functions g_j, corresponding to contributions from six unique moment tensor elements M_l, with a weighting for the nondiagonal elements of **M**, that appear twice in eq. 3.1. The orientation of the source is considered to remain fixed during the rupture, i.e., M_l does not depend on t, so that a single time series $s(t)$ is sufficient to describe rupture evolution.

For intermediate-size earthquakes ($5.5 < M_W < 7.0$) the STF typically has a duration of several seconds, which is not short compared to the rapid sequence of P-pP-sP or S-sS pulses that shallow earthquakes produce in broadband seismograms. Most earthquakes are shallow in this sense, i.e., shallower than 50 km. In order to assemble tomography-sized data sets, it is therefore imperative to account for the source time function in any waveform fitting attempt that goes to frequencies above ≈0.05 Hz (Sigloch and Nolet, 2006).

Equation 3.2 is linear in $s(t)$, so that $s(t)$ can be determined by deconvolving $\vec{G}$ from $\vec{u}$ if M_j in considered fixed. However, $\vec{G}$ depends strongly on source depth (third component of vector $\vec{r}_s$), so that a misestimated source depth will strongly distort the shape of the STF, as demonstrated by Fig. 3.1. Another complication is present in the fact that observed seismograms $\vec{u}(t)$ (as opposed to the predicted Green's functions) are time-shifted relative to each other due to 3-D heterogeneity in the earth, and should be empirically aligned before deconvolving $s(t)$.

These issues can be overcome by solving iteratively for $s(t)$ and M_j (Sigloch and Nolet, 2006; Stähler et al., 2012), but the approach requires significant human interaction, which poses a challenge for the amounts of data now available for

regional or global tomography. Moreover, such an optimisation approach does not provide systematic estimates of parameter uncertainties.

Monte Carlo sampling avoids the unstable deconvolution and permits straightforward estimation of full parameter uncertainties and covariances. However, the model space to sample grows exponentially with the number of parameters, and the STF adds a significant number of parameters. In a naive approach, this number could easily be on the order of 100, i.e., computationally prohibitive. For example, the STFs deconvolved in Fig. 3.1 were parameterised as a time series of 25 s duration, sampled at 10 Hz, and thus yielding 250 unknowns – not efficient, since neighbouring samples are expected to be strongly correlated. This raises the question of how many independent parameters or degrees of freedom this problem actually has.

Due to intrinsic attenuation of the earth, the highest frequencies still significantly represented in teleseismic P-waves are around 1 Hz. If from experience we require a duration of 25 s to render the longest possible STFs occurring for our magnitude range (Houston, 2001), then the time-bandwidth product is 1 Hz * 25 s = 25, and the problem cannot have more degrees of freedom than that.

Efficient parametrisation then amounts to finding a basis of not more than 25 orthogonal functions that span the subspace of the real-world, band-limited STFs just described. In fact, we can empirically decrease the number of parameters even further. By the method of Sigloch and Nolet (2006), we have semi-automatically deconvolved more than 3000 broadband STFs while building data sets for finite-frequency tomography. Of these, we propose to use the 1000 STFs that we consider most confidently determined as prior information for what the range of possible STFs looks like, for earthquakes of magnitude $5.5 < M_W < 7.5$. By performing a Principal Component Analysis on this large set of prior STFs, we find that only around 10 empirical orthogonal wavelets are needed to satisfactorily explain almost all of the STFs, as shown in figure 3.2. In concrete terms, we applied the MATLAB function *princomp.m* to a matrix containing the 3000 prior STFs in its rows. The mean over the matrix columns (time samples) was subtracted prior to performing the decomposition, and is shown in Fig. 3.2a as wavelet $s_0(t)$. Principal Component Analysis then determines $s_1(t)$ as the function orthonormal to $s_0(t)$ that explains as much of the variance in the matrix rows as possible. After subtracting (optimally weighted) $s_1(t)$ from each row, function $s_2(t)$ is determined such that it is orthonormal to $s_0(t)$ and $s_1(t)$, and explains as much as possible of the remaining variance. Each subsequent iteration generates another orthonormal s_i until $i = 256$, the number of time samples (matrix columns). The source time function can now be expressed as

$$s(t) = \sum_{i=1}^{255} a_i s_i(t) + s_0(t). \tag{3.3}$$

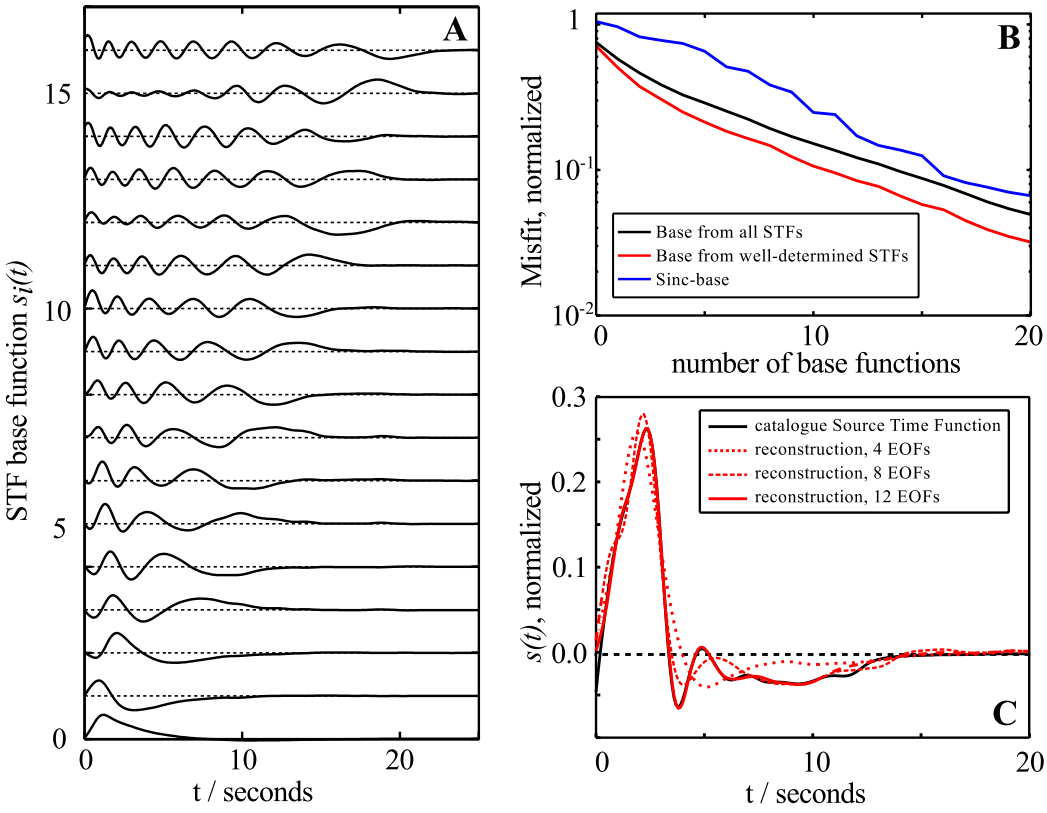

Figure 3.2: Efficient parametrisation of the STF in terms of empirical orthogonal functions, computed from a large set of manually deconvolved STFs that effectively serve as prior information. (a) First 16 members of the basis of empirical orthogonal functions. (b) Median RMS misfit between members of the prior STF catalogue and their projection on a subspace of the model space spanned by the first wavelet basis functions. (c) A typical STF from the catalogue, and its projection onto several subspaces spanned by the first few basis functions ($N = [4, 8, 12]$).

In this parametrisation, the new unknowns to solve for during source estimation are the a_i. Since Principal Component Analysis has sorted the a_i by their importance to explaining a typical STF, we may choose to truncate this sum at a relatively low value $N \ll 256$:

$$s_N(t) = \sum_{i=1}^{N} a_i s_i(t) + s_0(t), \tag{3.4}$$

In practice, N will be chosen based on the residual misfit between $s(t)$ and $s_N(t)$ that one is willing to tolerate. Figure 3.2(b) shows the dependence of this misfit on N. If we tolerate an average misfit of 5% in total signal variance, N = 12-14 basis functions are sufficient. In the following we use $N = 12$.

3.2.2 Parametrisation of the moment tensor

The orientation of the source can either be parametrised by a moment tensor using 6 parameters, or as a pure shear displacement source (Aki and Richards, 2002, p.112) with strike, slip and dip (to which a term for an isotropic component might be added).
Here we want to estimate the non-double-couple content of the solutions, and hence we sample the full moment tensor. The scalar moment is fixed to 1, so that only relative M_j are estimated. This is equivalent to sampling a hypersphere in the six-dimensional vector space $\{M_{\mathrm{xx}}, M_{\mathrm{yy}}, M_{\mathrm{zz}}, M_{\mathrm{xy}}, M_{\mathrm{yz}}, M_{\mathrm{xz}}\}$ with

$$M_0 = 1/\sqrt{2}\sqrt{M_{xx}^2 + M_{yy}^2 + M_{zz}^2 + 2(M_{xy}^2 + M_{yz}^2 + M_{xz}^2)} = 1. \tag{3.5}$$

Uniform sampling on a n-D hypersphere can be achieved by the method of Tashiro (1977), which transforms $n-1$ uniformly distributed random variables x_i to produce n random variables r_i that are distributed uniformly on a hypersphere with $\sqrt{\sum_{i=1}^{6} r_i^2} = 1$. We identify r_i with the moment tensor components and note that the non-diagonal elements $M_{kl}, k \neq l$ appear twice in the sum (thus we actually sample an ellipsoid rather than a hypersphere). We then have

$$x_i \sim U(0,1), \quad i = 1, 2, \ldots, 5$$
$$Y_3 = 1; \qquad Y_2 = \sqrt{x_2}; \qquad Y_1 = Y_2 x_1$$

$$
\begin{aligned}
M_{xx}/M_0 &= \sqrt{Y_1} \cdot \cos(2\pi x_3)\sqrt{2} \\
M_{yy}/M_0 &= \sqrt{Y_1} \cdot \sin(2\pi x_3)\sqrt{2} \\
M_{zz}/M_0 &= \sqrt{Y_2 - Y_1} \cdot \cos(2\pi x_4)\sqrt{2} \\
M_{xy}/M_0 &= \sqrt{Y_2 - Y_1} \cdot \sin(2\pi x_4) \\
M_{yz}/M_0 &= \sqrt{Y_3 - Y_2} \cdot \cos(2\pi x_5) \\
M_{zx}/M_0 &= \sqrt{Y_3 - Y_2} \cdot \sin(2\pi x_5)
\end{aligned}
\tag{3.6}
$$

3.2.3 Forward simulation

Broadband, teleseismic Green's functions for P-pP-sP and S-sS wave trains are calculated by the WKBJ code of Chapman (1978), using *IASP91* (Kennett and Engdahl, 1991) as spherically symmetric reference model for the mantle. The reference crust at the receiver site is replaced by the two-layered crust predicted by model CRUST2.0 (Bassin et al., 2000). Values for intrinsic attenuation are taken from the spherically symmetric earth model *PREM* (Dziewoński and Anderson, 1981). The synthetic waveforms are compared to the observed seismograms in time windows that start 10 s before the theoretical P-wave arrival time (according to *IASP91*) and end 41.2 seconds after.

3.3 Source parameter estimation by Bayesian sampling

3.3.1 Bayesian inversion

Bayesian Inversion is an application of Bayes' Rule

$$
P(\vec{m}|\vec{d}) = \frac{P(\vec{d}|\vec{m})P(\vec{m})}{P(\vec{d})}, \tag{3.7}
$$

where $\vec{m}$ is a vector of model parameters (in our case depth, moment tensor elements M_j and STF weights a_i), and $\vec{d}$ is a vector of data, i.e., a concatenation of P- and SH-waveforms. These quantities are considered to be random variables that follow Bayes' Rule. We can then identify $P(\vec{m})$ with the prior probability density of a model. This is the information on the model parameters that we have independent of the experiment. The conditional probability of $\vec{d}$ given $\vec{m}$, $P(\vec{d}|\vec{m})$, also called $\mathcal{L}(\vec{m}|\vec{d})$, is the *likelihood* of a model $\vec{m}$ to produce the data $\vec{d}$. Term $P(\vec{d})$ is constant for all models and is therefore dropped in what follows.

$P(\vec{m}|\vec{d})$ is called the posterior probability density (short, "the posterior"), and denotes the probability assigned to a model $\vec{m}$ after having done the experiment.

$$P(\vec{m}|\vec{d}) = P(\vec{m})\mathcal{L}(\vec{m}|\vec{d})k^{-1} \tag{3.8}$$

Since the posterior $P(\vec{m}|\vec{d})$ may vary by orders of magnitude for different $\vec{d}$, we work with its logarithm. We introduce the quantity $\Phi(m|\vec{d})$ to denote some kind of data misfit such that the likelihood can be written as $\mathcal{L}(\vec{m}) = \exp[-\Phi(\vec{m}|\vec{d})]$.

$$\ln\left(P(\vec{m}|\vec{d})\right) = -\Phi(\vec{m}|\vec{d}) + \ln P(\vec{m}) - \ln k. \tag{3.9}$$

The normalisation constant k is

$$k = \int \exp[-\Phi(\vec{m}|\vec{d})]P(\vec{m})\mathrm{d}\vec{m} \tag{3.10}$$

and calculated by the Neighbourhood Algorithm in the ensemble inference stage. In case of Gaussian-distributed noise on the data with a covariance matrix S_D

$$\vec{d} = g(\vec{m}) + \epsilon, \quad \epsilon \sim \mathcal{N}(0, S_D) \tag{3.11}$$

where $g(\vec{m})$ is the data predicted by model $\vec{m}$, we would obtain the familiar expression

$$\Phi(\vec{m}|\vec{d}) = k'\left(\frac{1}{2}(\vec{d} - g(\vec{m}))^T S_D^{-1}(\vec{d} - g(\vec{m}))\right). \tag{3.12}$$

This term is usually called Mahalanobis distance or ℓ^2 misfit. We do not choose this sample-wise difference between observed and predicted waveforms as our measure of misfit, since for tomography we do not use it either. There are questions about the Gaussian noise assumption for real data, but mainly we consider there to be a measure that is more robust and adapted to our purpose, the cross-correlation (mis-)fit between data and synthetics (Sigloch and Nolet, 2006; Nolet, 2008), which essentially quantifies phase misfit. In the optimisation-based, linearised approach to tomography, fitting the phase shift between two waveforms remains a near-linear problem in a wider range around the reference model than fitting the waveforms sample-wise. The cross-correlation fit is defined as:

$$\mathrm{CC}(\Delta T_i) = \frac{\int_t (u_i^c(t - \Delta T_i) \cdot u_i(t)\mathrm{d}t)}{\int_t u_i^c(t - \Delta T_i)\mathrm{d}t \cdot \int_t u_i(t - \Delta T_i)} \tag{3.13}$$

where $u_i(t)$ is the measured and $u_i^c(t)$ is the synthetic waveform for a model $\vec{m}$ at station i. In general, CC is a function of the time lag ΔT_i for which we compare the observed and predicted waveforms, but here we imply that ΔT_i has already

been chosen such as to maximise $CC(\Delta T_i)$. (This value of ΔT_i that maximises the cross-correlation is called the "finite-frequency travel time anomaly" of waveform $u_i(t)$, and represents the most important observable for finite-frequency tomography (Nolet, 2008; Sigloch and Nolet, 2006). Section 3.4.3, which discusses error propagation from source inversion into tomographic observables, should clarify this motivation of the cross-correlation criterion further.)

Correlation $CC(\Delta T_i)$ measures goodness of fit, so we choose decorrelation $D_i = 1 - CC(\Delta T_i)$ as our measure of misfit (one scalar per wavepath i). From the large set of pre-existing deterministic source solutions described in Sect. 3.2.1, we estimated the distribution of this misfit D_i, based on our reference data set of about 1000 very confidently deconvolved STF solutions. For this large and highly quality-controlled set of earthquakes, we empirically find that the decorrelation D_i of its associated seismograms $u_i(t) - u_i^c(t)$ follows a log-normal distribution in the presence of the actual noise and modelling errors. The statistics of this finding are discussed further in the companion paper (Stähler et al., 2014), but here we use it to state our likelihood function $\mathcal{L}$, which is the multivariate log-normal distribution:

$$\mathcal{L} = \frac{\exp\left(-\frac{1}{2}\left(\ln(\vec{D}) - \vec{\mu}\right)^T S_D^{-1}\left(ln(\vec{D}) - \vec{\mu}\right)\right)}{(2\pi)^{\frac{n}{2}}\sqrt{|\det(S_D)|}} \tag{3.14}$$

$\vec{D}$ is the decorrelation vector into which n decorrelation coefficients D_i are gathered. Each D_i was measured on a pair of observed/predicted broadband waveforms that contained either a P- or an SH-arrival. The parameters of this multivariate log-normal distribution are its mean vector $\vec{\mu}$ containing n means μ_i and its covariance matrix S_D. Empirically we find that the μ_i and the standard deviations σ_i (diagonal elements of S_D) depend mainly on the signal-to-noise-ratio (SNR) of waveform u_i. The data covariance between two stations i and j (off-diagonal elements in S_D) is predominantly a function of the distance between station i and station j. We estimate their values from the data set of the 1000 trustworthy STF solutions, i.e., from prior information, and proceed to use these $\vec{\mu}$ and S_D in our Bayesian source inversions.

It follows from Eq. 3.14 that the misfit Φ is

$$\Phi = \frac{1}{2}\left(\sum_i^n \sum_j^m \left(\ln(D_j) - \mu_j\right)^T S_{D,ij}^{-1}\left(ln(D_j) - \mu_j\right)\right) + \frac{1}{2}\ln\left((2\pi)^n |\det(S_D)|\right) \tag{3.15}$$

3.3.2 Construction of the prior probability density

A crucial step in Bayesian inference is the selection of prior probabilities $P(\vec{m})$ on the model parameters $\vec{m}$. Our model parameters are:

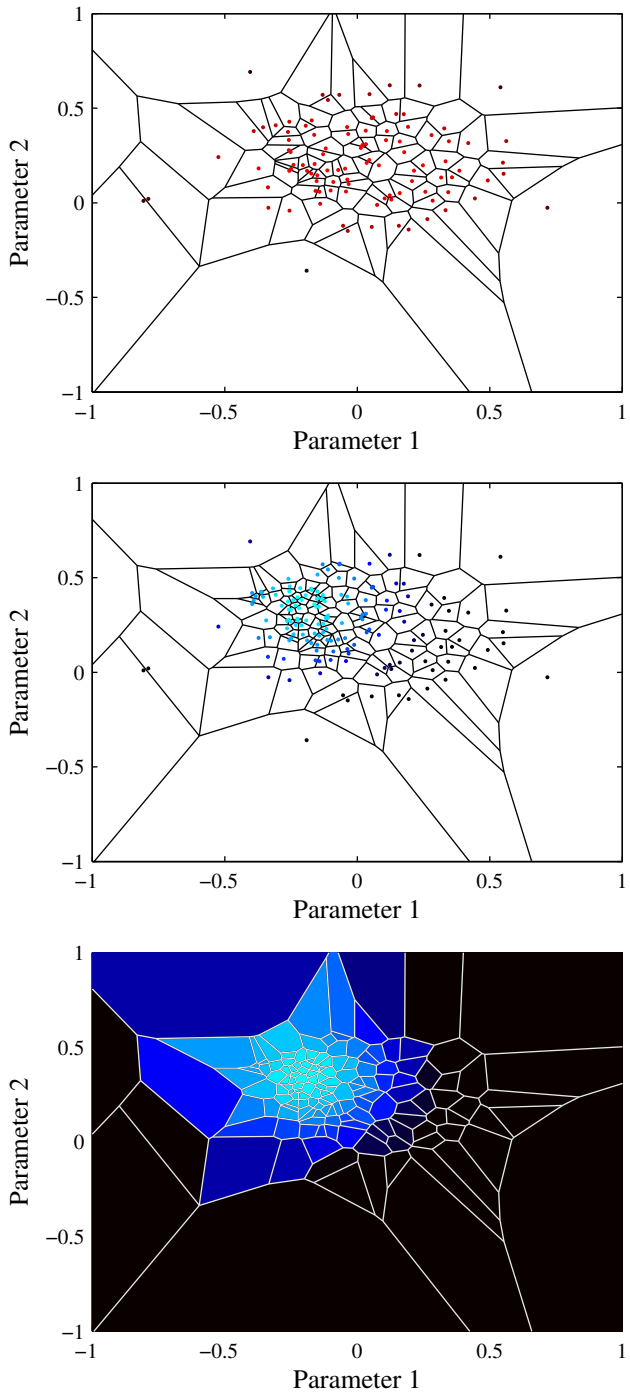

Figure 3.3: Principle of the Neighbourhood Algorithm, demonstrated for a two-dimensional toy problem (the underlying distributions are fictional and chosen for demonstration purposes). Top: In the pre-mapping stage, only the prior distribution is evaluated, resulting in a map of starting models that cluster in regions of high prior probability (marked by lighter shades of red). Middle: Next, the NA loads this map, evaluates the posterior probability for every sample, and refines the map only in the best fitting Voronoi cells. Lighter shades of blue correspond to a higher posterior probability. Bottom: In the sampling or appraisal stage, the value of the posterior is interpolated to the whole Voronoi cell. The Gibbs sampler uses this map to produce an ensemble. This ensemble can be used to calculate integrals over the model space, like the mean or mode of selected parameters.

i	range	i	range	i	range
1	± 1.5	6	± 0.7	11	± 0.4
2	± 1.0	7	± 0.7	12	± 0.4
3	± 0.9	8	± 0.6	13	± 0.3
4	± 0.8	9	± 0.5	14	± 0.3
5	± 0.8	10	± 0.5	15	± 0.3

Table 3.1: Sampling of the prior probability distribution: range of STF weights a_i that are permitted in the first stage of the Neighbourhood Algorithm.

- m_1: source depth. We assume a uniform prior based on the assumed depth of the event in the NEIC catalogue. If the event is shallow according to the ISC catalogue (< 30 km), we draw from depths between 0 km and 50 km, i.e., $m_1 \sim \mathcal{U}(0, 50)$. For deeper events, we draw from depths between 20 km and 100 km. Events deeper than 100 km have to be treated separately, using a longer time window in eq. 3.13 that should include the surface reflected phases *pP* and *sP*.

- $m_2, ..., m_{13} = a_1, ..., a_{12}$, the weights of the source time function (Eq. 3.4). The samples are chosen from uniform distributions with ranges shown in table 3.1, but are subjected to a prior π_{STF} (see below).

- $m_{14}, ..., m_{18} = x_1, ...x_5$, the constructor variables for the moment tensor (Eq. 3.6). $x_i \sim \mathcal{U}(0, 1)$, but they are subjected to two priors π_{iso} and π_{CLVD} (see below).

An earthquake is caused by the release of stress that had built up along a fault, driven by shear motion in the underlying, viscously flowing mantle. Hence the rupture is expected to proceed in only one direction, the direction that releases the stress. The source time function is defined as the time-derivative of the moment, $s(t) = \dot{m}(t)$. The moment is proportional to the stress and thus monotonous, and hence $s(t)$ should be non-negative. In practice, an estimated STF is often not completely non-negative (unless this characteristic was strictly enforced). The reason for smaller amounts of "negative energy" (time samples with negative values) in the STF include reverberations at heterogeneities close to the source, which produce systematic oscillations that are present in most or all of the observed seismograms. Motivated by waveform tomography, our primary aim is to fit predicted to observed waveforms. If a moderately non-negative STF produces better-fitting synthetics, then our pragmatic approach is to accept it, since we are not interested in source physics *per se*. However, we still need to moderately penalise non-negative samples in the STF, because otherwise they

creep in unduly when the problem is underconstrained, due to poor azimuthal receiver coverage. In such cases, severely negative STFs often produce marginally better fits by fitting the noise.

Our approach is to punish slightly non-negative STF estimates only slightly, but to severely increase the penalty once the fraction of "negative energy" I exceeds a certain threshold I_0. To quantify this, we define I as the squared negative part of the STF divided by the entire STF squared:

$$I = \frac{\int_0^T s_N(t)^2 \cdot \Theta(-s_N(t))dt}{\int_0^T s_N(t)^2}, \text{where} \tag{3.16}$$

$$s_N = s_0(t) + \sum_{i=1}^{N} a_i s_i(t) \tag{3.17}$$

and Θ is the Heaviside function. Based on I, we define a prior π_{STF}:

$$\pi_{\text{STF}}(m_2, ..., m_{13}) = \exp\left[-\left(\frac{I}{I_0}\right)^3\right], \tag{3.18}$$

where the third power and $I_0 = 0.1$ have been found to work best. In other words, we do not mind if up to 10% of STF variance is contributed by negative samples (mostly oscillations), but we do not tolerate more negative samples than that.

The Neighbourhood Algorithm supports only uniform distributions on parameters. The introduction of π_{STF} defined by Eq. 3.18 leads to a certain inefficiency, in that parts of the model space are sampled that are essentially ruled out by the prior. We carefully selected the ranges of the a_i by examining their distributions for the 3000 catalogue solutions. A test was to count which fraction of random models were consistent with $I < 0.1$. For the ranges given in Table 3.1, we found that roughly 10% of the random STF estimates had $I < 0.1$.

A second prior constraint is that earthquakes caused by stress release on a fault should involve no volume change, meaning that the isotropic component $M_{\text{iso}} = M_{\text{xx}} + M_{\text{yy}} + M_{\text{zz}}$ of the moment tensor should vanish. Hence we introduce another prior constraint

$$\pi_{\text{iso}}(m_{14}, ..., m_{18}) = \exp\left[-\left(\frac{M_{\text{iso}}/M_0}{\sigma_{\text{iso}}}\right)^3\right] \tag{3.19}$$

where M_0 is the scalar moment, and $\sigma_{\text{iso}} = 0.1$ is chosen empirically.

Third, we also want to encourage the source to be double-couple-like. A suitable prior is defined on the Compensated Linear Vector Dipole (CLVD) content,

which is the ratio $\epsilon = |\lambda_3|/|\lambda_1|$ between smallest and largest deviatoric eigenvalues of the moment tensor:

$$\pi_{\text{CLVD}}(m_{14}, ..., m_{18}) = \exp\left[-\left(\frac{\epsilon}{\sigma_{\text{CLVD}}}\right)^3\right] \tag{3.20}$$

A moment tensor with $\epsilon = 0.5$ corresponds to a purely CLVD source, while $\epsilon = 0$ is a pure DC source. Again we have to decide on a sensible value for the characteristic constant σ_{CLVD}. For intermediate-sized earthquakes of the kind we are interested in, $\epsilon \leq 0.2$ seems to be a reasonable value (Kuge and Lay, 1994). The total prior probability density is then

$$\begin{aligned} P(\vec{m}) &= \pi_{\text{STF}}(m_2, ..., m_{13}) \\ &+ \pi_{\text{iso}}(m_{14}, ..., m_{18}) + \pi_{\text{CLVD}}(m_{14}, ..., m_{18}) \end{aligned} \tag{3.21}$$

3.3.3 Sampling with the Neighbourhood Algorithm

Our efficient wavelet parametrisation of the STF reduces the total number of model parameters to around 18, but sampling this space remains non-trivial. The popular Metropolis-Hastings-algorithm (Hastings, 1970) can handle problems of this dimensionality, but is nontrivial to use for sampling of multimodal distributions (see the discussion for details). Better suited and faster is a Gibbs sampler, but it needs to know the conditional distribution $p(x_j|x_1, ...x_{j-1}, x_{j+1}, x_n)$ along parameter x_j in the n-dimensional model space (Geman and Geman, 1984). This conditional distribution is usually not available, especially not for nonlinear inverse problems.
To overcome the problem of navigation in complex high-dimensional model spaces, the Neighbourhood Algorithm uses Voronoi cells (Sambridge, 1998) to approximate a map of the misfit landscape (Sambridge, 1999a, first stage), followed by a Gibbs sampler to appraise an ensemble based on this map (Sambridge, 1999b, second stage).

In order to point the map-making first stage of the NA into the direction of a priori allowed models, we use a pre-calculated set of starting models. For that, the NA is run without forward simulations and without calculating the likelihood, so that only a map of the prior landscape is produced, from 32,768 samples (Fig. 3.3a). The resulting 32,768 Voronoi cells are used as a starting set to produce a map of the posterior landscape. This means that from the start, the map will be more detailed in a priori favourable regions, and avoids that the algorithm will waste too much time refining the map in regions that are essentially ruled out by the prior.

Next, the prior landscape is loaded and a forward simulation is run for each member in order to evaluate its posterior probability. Then this map is further

	V_P	V_S	ρ	depth
Upper crust:	4.10 km/s	2.15 km/s	2.51 Mg/m³	10.5 km
Lower crust:	6.89 km/s	3.84 km/s	2.98 Mg/m³	24.5 km

Table 3.2: Crustal model assumed for the source region of the 2011 Virginia earthquake (CRUST2.0).

Credible intervals for source parameters:

	1st decile	median	9th decile
depth	1.8	5.9	11
M_W	5.57	5.67	5.74
M_{tt}	-0.233	1.38	2.54
M_{tp}	-1.99	-0.955	-0.165
M_{rt}	-2.7	-0.325	2.72
M_{pp}	-9.4	-4.74	-2.7
M_{rp}	-3.25	-0.563	1.87
M_{rr}	3.16	4.42	7.84

Table 3.3: Credible intervals for source parameters of the Virginia earthquake. The moment tensor components M_{kl} need to be multiplied by 10^{16} Nm.

refined by 512 forward simulations around the 128 best models. This is repeated until a total of 65,536 models have been evaluated.
In the second stage of the NA, which is the sampling stage, 400,000 ensemble members are drawn according to the posterior landscape from the first step. This process runs on a 16 core Xeon machine and takes around 2 hours in total per earthquake.

3.4 A FULLY WORKED EXAMPLE

3.4.1 2011/08/23 Virginia earthquake

In the following we present a fully worked example for a Bayesian source inversion, by applying our software to the $M_W 5.7$ earthquake that occurred in Central Virginia on 23 August 2011 (figures 3.4 and 3.5, also compare to figure 3.1). While not considered a typical earthquake region, events from this area have nevertheless been recorded since the early days of quantitative seismology (Taber, 1913). Due to its occurrence in a relatively unusual but densely populated area, this relatively small earthquake was studied in considerable detail, affording us the opportunity to compare to results of other workers. Moderate-sized events of this kind are typical for our targeted application of assembling a large

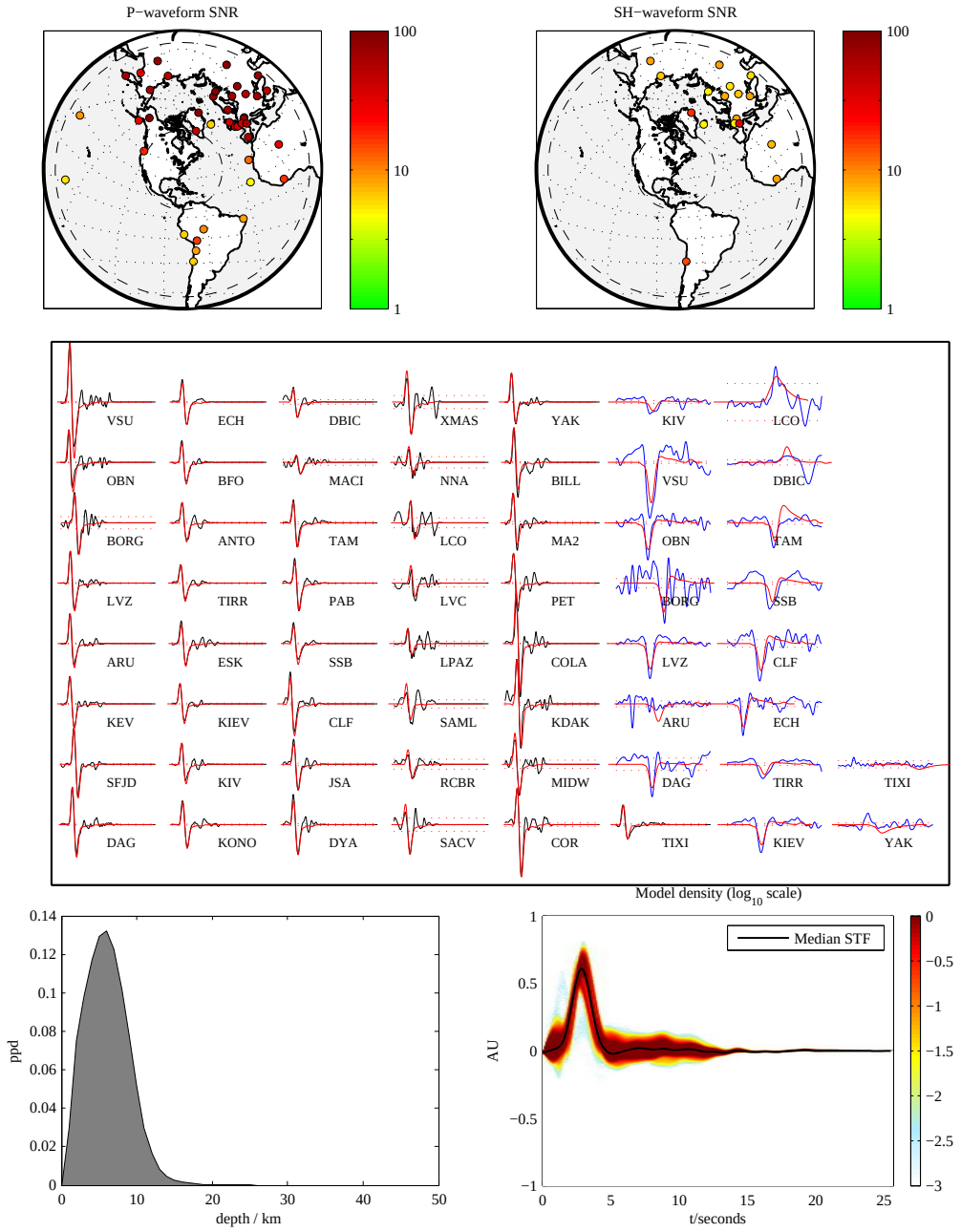

Figure 3.4: Waveform data and source estimates for the 2011/08/23 Virginia earthquake (M_W 5.7). Top row: Distribution of 41 and 17 teleseismic broadband stations that recorded P- and S-waveforms, respectively. Station colour corresponds to the signal-to-noise ratio in the relevant waveform window. Middle row: Synthetic broadband waveforms (red), compared to the data for the best fitting model. Black waveforms are P-seismograms, blue waveforms are SH-seismograms. The time windows are $51.2\ s$ long and start $5\ s$ before the theoretical phase arrival time. The amplitudes of all P- and SH-waveforms have been normalised. Bottom left: posterior marginal distribution of estimated source depth. Bottom right: posterior marginal distribution of the source time function. Probability densities are marked by colour and are highest in the areas shaded red.

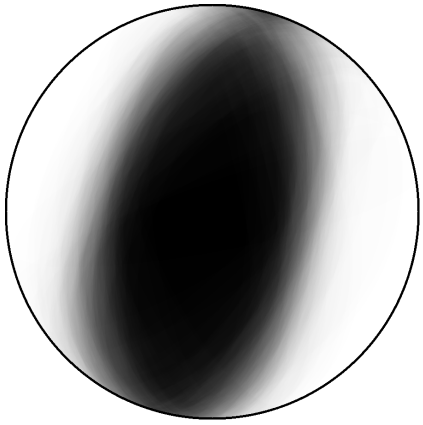

Figure 3.5: Bayesian beach ball: Probabilistic display of focal mechanism solutions for the 2011 Virginia earthquake.

catalogue. The greatest abundance of suitable events is found just below magnitude 6; toward smaller magnitudes, the teleseismic signal-to-noise ratio quickly deteriorates below the usable level.

For the inversion, we used a set of 41 P waveforms and 17 SH waveforms recorded by broadband stations at teleseismic distances (fig. 3.4). For waveform modelling, the crustal structure of model CRUST 2.0 (Bassin et al., 2000) was assumed around the source region; values are given in table 3.2. The algorithm ran 65,536 forward simulations to generate a map of the posterior landscape, and produced an ensemble of 400,000 members in the second step. From this ensemble, the source parameters were estimated. Table 3.3 shows the estimated credible intervals and the mode of the depth and the moment tensor. These quantiles represent only a tiny part of the information contained in the ensemble, i.e., two statistics of 1-dimensional marginals derived from a 16-dimensional probability density function. Some credible intervals are large, for example we cannot constrain the depth to a range of less than 10 km with 90% credibility. Using such credible interval estimates, routine production runs of our software should be able to clarify whether depth uncertainties in existing catalogues tend to be overly optimistic or pessimistic. The complete marginal distribution of the source depth estimate is shown in figure 3.3, bottom left.

We aim for additional, informative ways of summarising and conveying the resulting ensemble. Figure 3.5 is what we call a “Bayesian beach ball”: an overlay of 1024 focal mechanisms drawn from the ensemble at random. The thrust faulting character of the event is unambiguous, but the direction of slip is seen to be less well constrained. The estimate of the source time function and its un-

certainty are displayed in figure 3.4, bottom right. Within their frequency limits, our teleseismic data prefer a single-pulsed rupture of roughly 3 s duration, with a certain probability of a much smaller foreshock immediately preceding the main event. Smaller aftershocks are possible, but not constrained by our inversion.

3.4.2 Comparison to source estimates of other workers

Our solution is consistent with the solution from the SCARDEC catalogue (Vallée, 2012), which puts the depth of this event at 9 km, and its STF duration at 2.5 s. Chapman (2013) studied the source process of the 2011 Virginia event in great detail. He argues for three sub-events having occurred within 1.6 s at a depth of 7-8 km, and spaced less than 2 km apart. This is compatible with our solution: since teleseismic waveforms contain little energy above frequencies of 1 Hz, we would not expect to resolve three pulses within 1.6 s with the method presented here. Chapman (2013) used both local and teleseismic recordings, and was therefore able to exploit high frequencies recorded close to the source. His local crustal model featured an upper crustal velocity that was 50% higher than ours, which may explain why he estimates the source 1-2 km deeper than our most probable depth of 5.9 km (figure 3.4, bottom left).

3.4.3 Uncertainty propagation into tomographic observables

We are interested in source estimation primarily because we want to account for the prominent signature of the source wavelet in the broadband waveforms that we use for waveform tomography. Input data for the inversion, primarily traveltime anomalies ΔT_i, where i is the station index, are generated by cross-correlating observed seismograms with predicted ones. A predicted waveform consists of the convolution of a synthetic Green's function with an estimated source time function (eq. 3.2). Thus uncertainty in the STF estimate propagates into the cross-correlation measurements that generate our input data for tomography. Previous experience has led us to believe that the source model plays a large role in the uncertainty of ΔT_i. The probabilistic approach presented here permits to quantify this influence by calculating $\Delta T_{i,j}$ for each ensemble member j. From all values for one station, the ensemble mean $\overline{\Delta T_i}$ and its standard deviation σ_i can then be used as input data for the tomographic inversion. Thus we obtain a new and robust observable: Bayesian traveltime anomalies with full uncertainty information.

Figure 3.6 shows the standard deviation σ_i of P-wave ΔT_i at all stations. Comparison to the signal-to-noise ratios of fig. 3.6 shows no overall correlation, except for South American stations, where a higher noise level is correlated

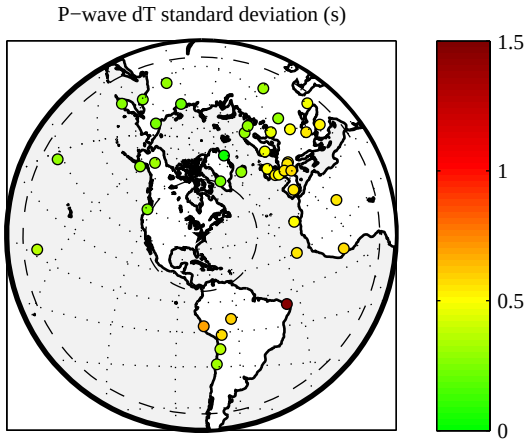

Figure 3.6: Standard deviations σ_i of P-wave travel times ΔT_i, as calculated from the ensemble of solutions. The travel time estimates are by-products of using waveform cross-correlation as the measure for goodness of fit, and they represent our main input data for tomographic inversions. The unit on the colour scale is seconds.

with a somewhat larger uncertainty on ΔT_i. By contrast, European stations all have good SNR, but uncertainties in the travel times are large nonetheless, because source uncertainty happens to propagate into the estimates of ΔT_i more severely in this geographical region. This information would not have been available in a deterministic source inversion and could strongly affect the results of seismic tomography.

3.5 Discussion

3.5.1 Performance of the empirical orthogonal basis for STF parametrisation

We choose to parametrise the source time function in terms of empirical orthogonal functions (eofs), which by design is the most efficient parametrisation if the characteristics of the STFs are well known. We think that they are, having semi-automatically deconvolved thousands of STFs in prior work (Sigloch and Nolet, 2006; Sigloch, 2011) and compared them with other studies (Tanioka and Ruff, 1997; Houston, 2001; Tocheport et al., 2007). The flip side of this tailored basis is that it might quickly turn inefficient when atypical STFs are encountered.

From the appearance of the eofs in Fig. 3.2a, it is for example obvious that STFs longer than 20 s could not be well expressed well as a weighted combination of only 10 eofs. Hence the STFs of the strongest earthquakes considered (around M_W 7.5) might not be fit quite as well as the bulk of smaller events, which contributed more weight to defining the eof base. For our tomography application, this behaviour is acceptable and even desirable, since the largest events are no more valuable than smaller ones (often quite the opposite, since the point source approximation starts to break down for large events).

At first glance it might seem unintuitive that the basis functions have oscillatory character and thus negative parts, rather than resembling a set of non-negative basis functions (a set of triangles would be one such set). Remember however that the training collection to which the Principal Components Analysis was applied did consist of predominantly non-negative functions, which by construction are then represented particularly efficiently, even if the eofs may not give this appearance. On top of this, we explicitly encourage non-negativity of the solution via the prior π_{STF} (Eq. 3.18). A rough estimation showed that roughly 90% of the model space are "forbidden" by the condition that the source should have a vanishing negative part.

We wanted to know how many basis functions of a more generic basis (e.g., wavelets) would be required in order to approximate the STF collection equally well as with the eofs. A trial with a basis of sinc-wavelets showed that 16 basis functions were needed to achieve the same residual misfit as delivered by our optimised basis of only 10 eofs. Since the size of the model space grows exponentially with the number of parameters, avoiding 6 additional parameters makes a big difference in terms of sampling efficiency.

3.5.2 Moment tensor parametrisation

The parametrisation of the moment tensor is a technically non-trivial point. We discuss the pros and cons of possible alternatives to our chosen solution:

- Parameterisation in terms of strike ϕ_f, slip λ and dip δ is problematic for sampling. Strike and dip describe the orientation of the fault plane; an equivalent description would be the unit normal vector $\vec{n}$ on the fault.

$$\vec{n} = \begin{pmatrix} -\sin\delta\sin\phi_f \\ -\sin\delta\cos\phi_f \\ \cos\delta \end{pmatrix} \tag{3.22}$$

  All possible normal vectors form a unit sphere. In order to sample uniformly on this unit sphere, samples have to be drawn from a uniform volumetric density (Tarantola, 2005, 6.1). Since the Neighbourhood Algorithm

(and most other sampling algorithms) implicitly assume Cartesian coordinates in the model space, the prior density has to be multiplied by the Jacobian of the transformation into the actual coordinate system, in our case $1/\sin\delta$. To our knowledge, this consideration is neglected in most model space studies, but it would be more severe in ensemble sampling than in gradient-based optimisation.

- A different issue with strike-dip parametrisation is the following: the Euclidean distances applied to $\{\phi_f, \lambda, \delta\}$ by the NA and similar, Cartesian-based algorithms are in fact a rather poor measure of the similarity of two double couple sources. A more suitable measure of misfit is the Kagan angle (Kagan, 1991) or the Tape measure (Tape and Tape, 2012), which is the smallest angle required to rotate the principal axes of one double couple into the corresponding principal axes of the other.
  This is an issue in model optimisation with the first stage of the Neighbourhood Algorithm (Kennett et al., 2000; Sambridge and Kennett, 2001; Vallée et al., 2011). Wathelet (2008) has introduced complex boundaries to the NA, but unfortunately no periodic ones.

- An alternative would be to sample $\{M_{xx}, M_{yy}, M_{zz}, M_{xy}, M_{yz}, M_{xz}\}$ independently, but this is inefficient because the range of physically sensible parameters spans several orders of magnitude.

- Finally, one might choose not to sample the moment tensor at all. Instead, one might sample only from the $\{S_i, d\}$ model space, followed by direct, linear inversion of the six moment tensor elements corresponding to each sample. This would speed up the sampling considerably since the dimensionality of the model space would be reduced from 16 to 10. Moment tensor inversion is a linear problem (Eq. 3.2), and hence we would not lose much information about uncertainties. In a potential downside, moment tensor inversion can be unstable in presence of noise or bad stations, but from our experience with supervised, linear inversions, this is typically not a severe problem in practice. Therefore we are considering this pragmatic approach of reduced dimensionality for production runs.

3.5.3 Neighbourhood Algorithm

The Neighbourhood Algorithm avoids some of the pitfalls of other sampling algorithms. Compared to the popular Metropolis-Hastings-algorithm (MH), we see several advantages for our problem: The Neighbourhood Algorithm avoids some of the pitfalls of other sampling algorithms. Compared to the popular

Metropolis-Hastings-algorithm (MH), we see several advantages for our problem:

- The MH is difficult to implement for multivariate distributions. This is especially true, when the parameters are different physical quantities and follow different distributions as is the case in our study.
- As the MH is a random-walk algorithm, the step width is a very delicate parameter. It affects the convergence rate and also the correlation of models, which has to be taken into account, when estimating PDFs from the ensemble. This is a bigger problem than for the Gibbs sampler, which the NA is based on.
- The MH is rather bad at crossing valleys of low probability in multimodal probability distributions. We are expecting such, especially for the source depth.

These problems are less severe for a Gibbs sampler, on which the first stage of the NA is based. In theory, the first stage of the NA could be replaced by a completely separate mapping algorithm, like Genetic Algorithms or Simulated Annealing, which are no sampling algorithms. Like the first stage of the NA, they only explore the model space for a best-fitting solution. Their results however might be used as input for the second stage of the NA. We are not aware of any examples. Compared to those, the NA uses only two tuning parameters, which control (a) how many new models are generated in each step and (b) in how many different cells these models are generated. As in every optimisation algorithm, they control the tradeoff between exploration of the model space, and exploitation of the region around the best models.

There is no hard and fast rule for choosing values for these tuning parameters. Since we do not want to optimise for only one "best" solution, we tend towards an explorative strategy and try to map large parts of the model space. Compared to other source inversion schemes, we are explicitly interested in local minima in the misfit landscape. Local minima are often seen as nuisance, especially in the rather aggressive iterative optimisation frameworks, but in our view, they contain valuable information. What may appear as a local minimum to the specific data that we are using for inversion, might turn out to be the preferred solution of another source inversion method (e.g., surface waves, GPS or InSAR).

However, an ensemble that does not resolve the best fitting model is equally useless. The posterior of all models gets normalised after all forward simulations have been done (see Eq. 3.10). If one peak (the best solution) is missing, the normalisation constant Z will be too small, and therefore $P(\vec{m}|\vec{d})$ will be too high for all models, meaning that the credibility bounds will be too large. It

is possible that other sampling schemes, such as *parallel tempering*, might find better compromises between exploration and exploitation, which could be a topic of further study.

3.5.4 Comparison with other source inversion schemes

Table 3.4 shows a list of other point source inversion algorithms proposed and applied over the past 15 years. Most widely used is probably the Global Centroid Moment Tensor (CMT) catalogue (Dziewoński et al., 1981; Ekström et al., 2012), which is mostly based on intermediate-period ($> 40\ s$) waveforms to determine a centroid moment tensor solution. Its results are less applicable to short-period body wave studies, since waveforms in the latter are dominated by the hypocenter, which may differ significantly from the centroid. Another classical catalogue is the ISC bulletin (Bondár and Storchak, 2011), which goes back as long as 1960. The ISC catalogue focuses on estimating event times and locations, neither of which are the topic of this study. The ISC recently adopted a global search scheme based on the first stage of the NA, similar to Sambridge and Kennett (2001), followed by an attempt to refine the result by linearised inversion, including inter-station covariances. Garcia et al. (2013) and Tocheport et al. (2007) use Simulated Annealing to infer depth and moment tensor. A STF is estimated from the P-waveforms. By neglecting all crustal contributions and reducing the forward simulation to mantle attenuation, this approach is very efficient.

Similarly, Kolář (2000) used a combination of Simulated Annealing and bootstrapping to estimate uncertainties of the moment tensor, depth and a source time function. The study was limited to two earthquakes and was never extended.

Kennett et al. (2000) used the first stage of the NA to optimise for hypocenter depth, moment tensor, and the duration of a trapezoidal STF, using essentially the same kind of data as the present study, and an advanced reflectivity code for forward modelling. However, no uncertainties were estimated.

Dębski (2008) is one of the only two studies we are aware of that did Bayesian inference of the source time function. He studied magnitude 3 events in a copper mine in Poland. By using the Empirical Green's Functions (EGF) method, it was not necessary to do an explicit forward simulation. The study was limited to inverting for the STF, which he parametrised sample-wise. This was possible since the forward problem was computationally very inexpensive to solve.

The second sampling study is Wéber (2006), which used an Octree importance sampling algorithm to infer probability density functions for depth and moment tensor rate function. The resulting ensemble was decomposed into focal mechanisms and source time functions, a nontrivial and nonunique problem (Wéber, 2009). With this algorithm, a catalogue of Hungarian seismicity was

produced until 2010, but apparently this promising work was not extended to a global context.

The most recent global source catalogue is the *SCARDEC* method by Vallée et al. (2011). It uses the first stage of the Neighbourhood Algorithm to optimise the parameters source depth, strike, dip and rake. For each model and each station, a *Relative Source Time Function* is calculated. The misfit is comprised of a waveform misfit and the differences between the RSTF at different stations. Uncertainties of the parameters are estimated by the variation of the misfit along different parameters.

The *PRISM* algorithm as presented here is the first to enable Bayesian inference of seismic source parameters on a global scale and in a flexible framework. It allows for sampling of the source time function by a set of optimised, wavelet-like basis functions. By producing a whole ensemble of solutions, arbitrary parameters, like the uncertainty of travel time misfits can be estimated from the ensemble afterwards, at little additional cost.

3.6 Conclusions

We showed that routine Bayesian inference of source parameters from teleseismic body waves is possible and provides valuable insights. From clearly stated *a priori* assumptions, followed by data assimilation, we obtain rigorous uncertainty estimates of the model parameters. The resulting ensemble of *a posteriori* plausible solutions permits to estimate the propagation of uncertainties from the source inversion to other observables of practical interest to us, such as travel time anomalies for seismic tomography.

Table 3.4: Overview of similar source inversion algorithms

Name	characteristics					Inversion parameters				algorithms	
	Focus	Probabilistic	Depth range	Data	Catalogue	Depth	Location	Moment tensor	STF	Forward algorithm and model	Inversion algorithm
PRISM (this paper)	global	yes	full	waveforms, P, SH, teleseismic	yes	yes	no	yes	yes	reflectivity, IASP91 + crust	NA[a], both stages
Tocheport et al. (2007)	global	no	>100km	waveforms, P, teleseismic	no	no	no	yes	yes	none	SA[b]
Garcia et al. (2013)	global	no	full	waveforms, P, teleseismic	no	no	no	yes	yes	none	SA
Marson-Pidgeon and Kennett (2000)	global	no	full	waveforms, P, SH, SV	no	yes	no	yes	duration	reflectivity, ak135 + crust	NA, first stage
Sambridge and Kennett (2001)	global	no	full	traveltimes, P, S	no	yes	yes	no	no	ak135	NA, first stage
ISC (Bondár and Storchak, 2011)	global	no	full	traveltimes, all phases	yes	yes[c]	yes	no	no	ak135	NA, first stage
Global CMT (Ekström et al., 2012)	global	no	full	waveforms, P, S + surface	yes	yes	yes	yes	no	normal modes	
Sigloch and Nolet (2006)	global	no	full	waveforms, P, teleseismic	no	yes	no	yes	yes	WKBJ, IASP91	LSQR, iterative
Kolář (2000)	global	uncertainties	full	waveforms, P, SH, teleseismic	no	yes	yes	strike, slip, dip	yes	reflectivity (?), local model	SA + bootstrapping
SCARDEC (Vallée et al., 2011)	global	uncertainties	full	waveforms, P, SH, teleseismic	yes, fast	yes	no	strike, slip, dip	RSTF[d]	reflectivity, IASP91 + crust	NA, first stage
Wéber (2006)	local	yes	shallow	waveforms, P, local	no	yes	yes	yes	MTRF[e]	reflectivity, local model	octree importance sampling
Dębski (2008)	local	yes	shallow	waveforms, P, local	no	no	no	no	yes	EGF[f]	Metropolis-Hastings

[a] Neighbourhood Algorithm (Sambridge, 1999b)
[b] Simulated Annealing (Kirkpatrick et al., 1983)
[c] binning allowed
[d] Relative STF, one STF per station
[e] Moment tensor rate function, one STF per MT component
[f] Empirical Green's functions

There are known knowns; there are things we know that we know.
There are known unknowns; that is to say, there are things that we now know we don't know.
But there are also unknown unknowns – there are things we do not know we don't know."

United States Secretary of Defense, Donald Rumsfeld

4

Estimating the data uncertainties in seismic source inversion

This chapter is in preparation for submission to *Solid Earth* under the title *Fully probabilistic seismic source inversion – Part 2: Data (co) variances* (Stähler, Zhang, and Sigloch, 2014)

Abstract

Probabilistic source inversion in seismology is made difficult by the inherent nonlinearity of the problem. Also, once the Source Time Function is taken into account the dependence of a large number of free parameters makes ensemble sampling methods prohibitively expensive. We propose a framework to sample the earthquake depth, focal mechanism and source time function efficiently by using information from previous classical inversions. The Source Time Function is expressed as a weighted sum of several empirical wavelets derived from a catalogue of > 1000 STFs by Principal Component Analysis. Since we do not see a model of additive Gaussian noise on a waveform as sufficient, we reject misfit models as the ℓ^2-norm and rather use a waveform measure like the Cross-correlation or the Mean Coherence. To determine the Likelihood function for the Bayesian sampling, we look at the distribution of this waveform measure for catalogue results of source inversion.

$\vec{m}$	geophysical model vector
$g(\vec{m})$	forward operator acting on a model vector $\vec{m}$
$u(t)$	recorded seismogram
u_i	discrete version of $u(t)$
$u^{\mathrm{c}}(t)$	synthetic seismogram predicted by a model m and a forward operator $g(m)$
u_i^{c}	discrete version of $u^{\mathrm{c}}(t)$

Table 4.1: Symbols frequently used in this paper

4.1 Introduction

The derivation of source parameters is a classical inverse problem in seismology. Since it is inherently non-linear if the source location is not known, global search methods are useful and since the model parameters are strongly correlated, ensemble sampling can offer valuable insights. In a companion paper Stähler and Sigloch (2013) we presented a way to reduce the model space to make a probabilistic inversion for source depth, moment tensor and source time function feasible. When using waveforms as data, the selection of a suited misfit criterion is important, since the individual samples of one seismogram are strongly correlated and the misfit at multiple stations is correlated as well (Bondár and McLaughlin, 2009). This paper shall motivate, why the Mahalanobis distance (aka ℓ^2-norm) is not an optimal misfit for seismological waveform data and present as an alternative the waveform coherence. For Bayesian inference, it is necessary to know the relation between this misfit and the likelihood of measured data and a model. We infer this relation empirically from a large set of source solutions derived by a deterministic inversion.

4.2 Noise and misfit criteria

4.2.1 Likelihood

Bayesian inference derives the posterior distribution of the parameters using the prior distribution of the parameters and the likelihood of the given data. A likelihood $\mathcal{L}(m, d)$ is a function of the model parameters m given the observations d. It is equivalent to the probability distribution $p(d|m)$ of data d given the model parameters m (Gilks et al., 1996). In geophysical inverse problems the data is defined as the difference between the measurements d and predicted data calculated using the given parameters m and the forward operator $g(m)$.

To facilitate further discussion, we will introduce a quantity called *misfit* $\Phi(\vec{d}, g(\vec{m})) = -\ln(\mathcal{L}(m, d))$.

4.2.2 Misfit criteria

When estimating the parameters, the data is often assumed to be Gaussian distributed

$$\vec{d} = g(\vec{m}) + \epsilon, \quad \epsilon \sim \mathcal{N}(0, S_D) \tag{4.1}$$

, and the method of least square is applied to calculate the misfit.

$$\Phi(\vec{m}|\vec{d}) = k' \left(\frac{1}{2} (\vec{d} - g(\vec{m}))^T S_D^{-1} (\vec{d} - g(\vec{m})) \right). \tag{4.2}$$

The data covariance matrix S_D describes the correlation between the error of single measurements. In the case of seismic data, this is mainly the limited spectrum of environmental noise and the correlation of noise at different receivers (see Bodin et al. (2012) for an example of how to construct this matrix).
This misfit criterion is very sensitive to data d_i deviating strongly from the prediction $g_i(\vec{m})$. Therefore, in noisy settings, other authors have often used the ℓ^1 norm of the data to estimate the parameter distributions, where the noise on each datum d_i is assumed be independently Laplace-distributed.

$$\vec{d} = g(\vec{m}) + \vec{\epsilon}, \quad \epsilon_i \sim \text{Laplace}(0, b_i) \tag{4.3}$$

$$\Phi(\vec{m}|\vec{d}) = -\sum_i \frac{|d_i - g_i(\vec{m})|}{b_i}. \tag{4.4}$$

The ℓ^1-norm is more robust against outliers in the data, however there is no viable way of describing correlated measurements with it. The derivation of applicable multivariate Laplace distributions is ongoing work (Kotz et al., 2001; Kozubowski et al., 2013). The resulting probability density functions are yet to complex to be used in ensemble inference.

However, in Bayesian context, the likelihood can be chosen from any distributions $p(F)$ that best fit the data. For sampling, we can just as well define a Likelihood from the probability of any functional $F : \mathbb{R}^{2\times n} \mapsto unit$ on $u(t), u^c(t) \in \mathbb{R}^n$. To make sense as a misfit, it should fulfil the following conditions:

1. For $u(t) = u^c(t)$, it should take a fixed value, say 0.
2. With decreasing similarity of $u(t)$ and $u^c(t)$, it should increase (however we define *similarity* here).

3. It should be robust against time shifts or amplitude errors, i.e. $F\left(a \cdot u(t+\tau), u^c(t)\right) \approx F\left(u(t), u^c(t)\right)$ for any $a, \tau \in \mathbb{R}$.

Additionally, we would have to know how the values of F are distributed for a typical waveform in presence of the three error sources mentioned above.
The number of misfit criteria has vastly increased in the last years. Among the most popular are cross-correlation travel-time misfits (Sigloch and Nolet, 2006) or other time-frequency-misfits, which separate the phase and amplitude difference (Fichtner et al., 2009) or multitaper analysis of the transfer function (Tape et al., 2009). For a deeper discussion see Kennett and Fichtner (2012). While these are well suited for optimization problems, they cannot be used directly to infer posterior probabilities, since there is no analytical way to estimate their statistics. This fact has sometimes been implicitly ignored in recent literature (Fichtner and Trampert, 2011).
We instead choose the signal decorrelation D as a misfit criterion, defined as $D := 1 - CC(\Delta T)$. Here,

$$CC(\Delta T) = \int_{T_1}^{T_2} \left(u^c(t - \Delta T) \cdot u(t) dt\right) \tag{4.5}$$

is the maximum of the cross-correlation function $CC(\tau)$ between $u(t)$ and $u^c(t)$. D fulfils all three criteria defined above:

1. It takes the value 0 for identical signals.

2. For differing signals, D takes a value between 0 and 2 for exactly inverse signals. (The latter value is not reached for a finite signal and instead the smallest possible value is 1 minus the minimum of the autocorrelation function of the signal.)

3. This is equivalent to showing that $CC(\Delta T)$ for $u(t)$, $u^c(t)$is approximately equal to $CC'(\Delta T - \tau)$ for $u(t+\tau)$, $u^c(t)$.

$$\begin{aligned}
CC(\Delta T) &= \int_{T_1}^{T_2} \left(u^c(t - \Delta T) \cdot u(t) dt\right) \\
&= \int_{T_1-\tau}^{T_2-\tau} \left(u^c(t - \Delta T + \tau) \cdot u(t+\tau) dt\right) \\
&= \underbrace{\int_{T_1-\tau}^{T_1} \ldots dt - \int_{T_2-\tau}^{T_2} \ldots dt}_{\approx 0} + \int_{T_1}^{T_2} \ldots dt \\
&\approx \int_{T_1}^{T_2} \left(u^c(t - (\Delta T - \tau)) \cdot u(t+\tau) dt\right) \\
&= CC'(\Delta T - \tau)
\end{aligned} \tag{4.6}$$

Assuming small time shifts compared to the window length and a vanishing synthetic signal at the limits of the time window ($\lim_{t\to T_1,T_2} u^c(t) = 0;\ \tau \ll (T_2 - T_1)$).

While the cross-correlation coefficient has been used extensively in seismology to detect predicted waveforms in noisy signals, to filter bad recordings or detect temporal changes in repeating signals (Larose et al., 2010, e.g.), it has very seldom been used directly as a misfit criterion in source inversion (we are only aware of Kikuchi and Kanamori (1991) and Marson-Pidgeon and Kennett (2000)), mainly because its statistics are hard to assess. In the following section we present a novel approach using the decorrelation D as data.

4.3 Empirical Likelihood Function

4.3.1 Empirical Likelihood

How can we produce a Likelihood in absence of an analytically describable noise model?
A solution would be to leave the Bayesian interpretation for a moment and take a Frequentist's view:
We could see the measurements of the misfit functional $F(\vec{m}|\vec{d})$ at many stations for one earthquake as realisations of a random process, which follows a so-far unknown probability distribution $p(F)$. If we were able to look at a large number of representations of F for a "true" model $\vec{m}_0$, we could use the distribution of $F(\vec{m}_0|\vec{d})$ as the probability distribution $Pr(F)$ of the functional F for the true model $\vec{m}$ in presence of the noise and modelling errors on $\vec{d}$.
Furthermore, we would have to find an analytical probability density function p, so that

$$\Pr[a \leq F \leq b] = \int_a^b p(x)\,dx. \tag{4.7}$$

To produce a likelihood function from this misfit functional F, its distribution $p(F)$ has to be known.

$$L(m|d) = p\left(F(d|m)\right), \tag{4.8}$$

where

$$F(d|m) = D(d|m) = 1 - max\{CC(u(t)u^c(t))\}. \tag{4.9}$$

To estimate $p(F)$, we would need a large number of solutions for our inverse problem, where the distribution of p is only influenced by noise and modelling error, but not by the model parameters themselves. A source could be the results of a reliable deterministic inversion. If the deterministic inversion algorithm has

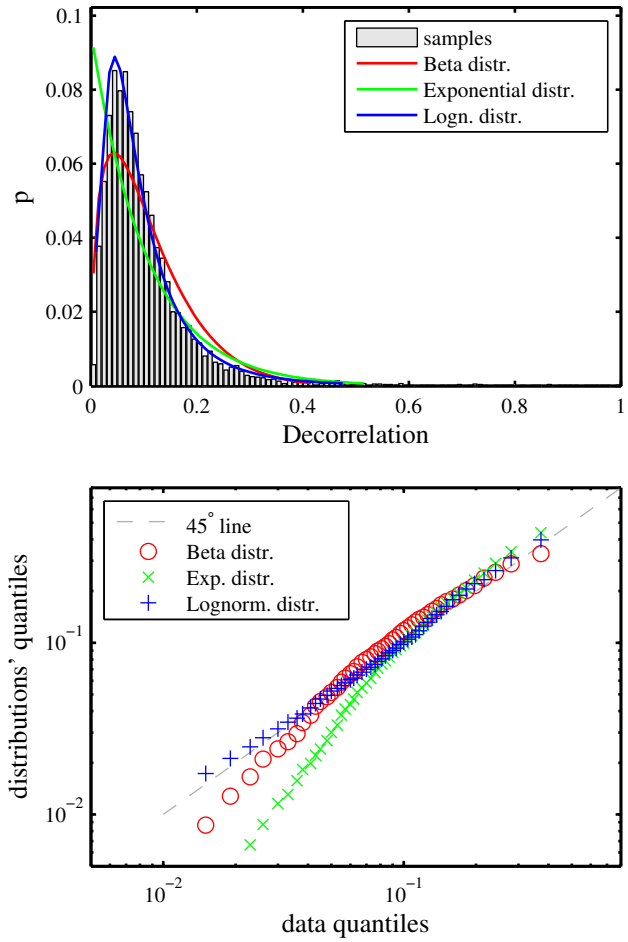

Figure 4.1: Distribution of D for the stations of one earthquake with magnitude 5.8 compared with a different distributions as a histogram (left) and as a quantile-quantile plot (right).

reduced F as far as possible, all residual should be due to the three error sources from section 4.5.1.
Therefore, we calculated D from seismograms and synthetic waveforms for 900 earthquakes with over 100 stations each. As model parameters for the synthetic seismograms, we used the ones obtained from a linearized inversion as described in Sigloch and Nolet (2006) and Stähler et al. (2012). A typical distribution of D is shown in Fig. 4.1a.
To determine an appropriate likelihood for the data D we consider positive distribution functions such as the beta, exponential and the log-normal distributions, which have little tail probability beyond 2 that can be neglected. Using empirical QQ-plots and empirical probability density plots we found out that the log-normal distribution

$$f(x) = \frac{1}{x\sqrt{2\pi\sigma^2}} \exp\left(-\frac{(\ln x - \mu)^2}{2\sigma^2}\right) \tag{4.10}$$

fits the data best, as shown in Fig. 4.2b. The beta and the exponential distribution seem to overestimate the number of very small values for D (i.e. values of $CC_{\max} \approx 1$). In turn, this would mean that such a distribution would await more very good waveform fits than realistic. The likelihood of actually good fitting waveforms would be estimated too low.

From fig. 4.1b, we chose the log-normal distribution to derive the likelihood. If the parameter D is a random variable distributed according to a log-normal distribution with parameters σ, μ, its logarithm $\ln(D)$ is normal distributed with the same parameters. This allows us to easily incorporate inter-station covariances in form of a covariance matrix S_D. The likelihood formula is then

$$L_{\mathrm{D}} = \frac{\exp\left(-\frac{1}{2}\sum_{i=1}^{m}\left(\ln(D_i) - \mu_i\right)^T S_D^{-1}\left(\ln(D_i) - \mu_i\right)\right)}{(2\pi)^{\frac{m}{2}}\sqrt{|\det(S_D)|}}, \tag{4.11}$$

which is the Mahalanobis distance (Mahalanobis, 1936), not of two waveforms, but of the decorrelation D and its expectation value μ.

4.3.2 Distribution coefficients and signal-to-noise-ratio

The argument so far seemed to assume that one distribution should fit D for all seismic stations and all earthquakes. This is an oversimplification. The noise level at stations varies hugely over the year and the day and is higher for stations close to a coast or a city (Stutzmann et al., 2000). Therefore, we might expect different goodnesses of fit at different stations. To reflect that, we could use separate distributions.

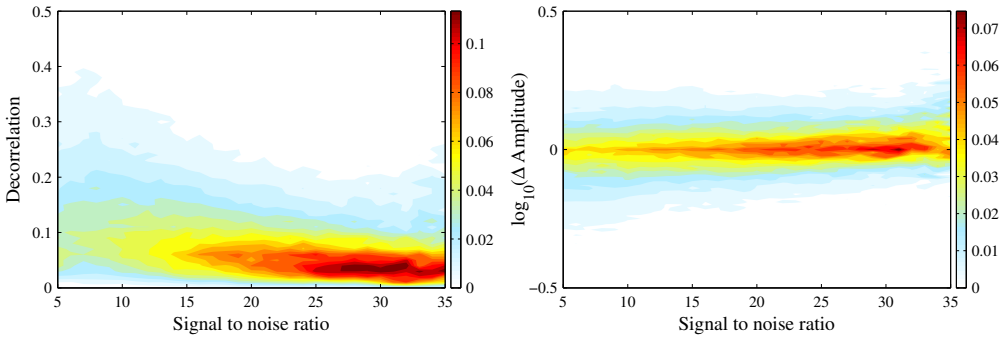

Figure 4.2: 2D-histogram of the density of D (left) and Δlog(A) (right) for different Signal to noise ratios. The density of D and Δlog(A) was calculated in SNR windows of width 1, centred on integer values. Each SNR window was normalized individually. Basically fig. 4.1 repeated for 30 SNR windows.

One possibility could be a database of noise levels for all stations. However, the fit quality is also influenced by the magnitude of the earthquake and azimuth and distance of the station, so we might want a criterion, which is based on the individual source and station.
An idea is to take the Signal-to-Noise Ratio (SNR) of the body wave recording. This is defined here as the integrated spectral energy of the signal time window divided by that of a noise window 60s before the arrival of the first body wave energy.
This means that the noise window before the P-wave contains only background noise, while the one for the SH-wave also may contain P-coda or phases like PP or PcP. In a spherically symmetric earth, like the one our forward solver is assuming, *P-SV* and *SH* should be decoupled and there should be no energy arriving on the transversal (SH) component before *SH*, but lateral heterogeneities and anisotropy convert some P-energy into transversal motion, so that the SH-phase is usually preceded by some signals on the transversal component.

Figure 4.2 shows the density of D for different SNRs. The distribution of D is narrower for high SNRs and centered on higher values, which seems both plausible. For each SNR window, we determined μ and σ of the best-fitting log-normal distribution.

The distribution parameters were calculated for SNRs from 1 to 200 (SH) resp. 1000 (P). Fit functions $h(\mathrm{SNR}) = a_1 + a_2 \cdot \exp(a_3 \cdot \mathrm{SNR})$ were used for $\mu_\mathrm{P}(\mathrm{SNR})$, $\mu_\mathrm{SH}(\mathrm{SNR})$, $\sigma_\mathrm{P}(\mathrm{SNR})$, $\sigma_\mathrm{SH}(\mathrm{SNR})$ (see chapter 4.6). With these, expec-

tation values μ_i and standard deviations σ_i for each station i are calculated from its Signal-to noise ratio SNR_i.

$$\begin{aligned} \mu_i &= a_{\mu,1} + a_{\mu,2} \cdot \exp(a_{\mu,3} \cdot \text{SNR}_i) \\ \sigma_i &= a_{\sigma,1} + a_{\sigma,2} \cdot \exp(a_{\sigma,3} \cdot \text{SNR}_i) \end{aligned} \tag{4.12}$$

4.3.3 Covariance information

To realistically estimate the model uncertainties, it is not sufficient to treat the measurements at different stations as independent. Under the assumption that the modelling errors which produce the likelihood distribution are a result of the earth structure differing from the (layered) model we used for forward calculation, this should influence multiple stations at once. A first guess would be that the effect is strongest for stations with similar azimuth from the source, since their ray paths "see" similar regions of the earth.
To check this influence, we calculated the Pearson correlation coefficient $r(\vartheta)$ in dependence of azimuthal distance ϑ as follows. For each event, the azimuthal difference between all station pairs i, j was calculated and the pairs were binned according to it. The set $\{i, j\}_\vartheta$ then contains all stations for one event, which have the same azimuthal difference (in bins of $5°$ width). The standard score $z_i = (\ln(D_i) - \mu_i)/\sigma_i$ of each station i was calculated using the mean μ_i and standard deviation σ_i expected for it according to its SNR.
Then the correlation coefficient was calculated for each azimuthal bin ϑ using all n_ϑ pairs $\{i, j\}_\vartheta$ in this bin.

$$r(\vartheta) = \frac{1}{n_\vartheta - 1} \sum_{\{i,j\}_\vartheta} z_i z_j \tag{4.13}$$

The values for $r(\vartheta)$ are fit by a function $g(\vartheta) = b_1 + b_2 \cdot \exp(-b_3 \vartheta^2)$ (see chapter 4.6.2).

This correlation coefficient in dependence of the azimuth can be used to fill the elements of the covariance matrix S_D in eq. 4.11

$$S_{Di,j} = \tag{4.14}$$

An example of such a covariance matrix for the Virginia event is shown in figure 4.3.

4.3.4 Amplitudes

Readers familiar with Source inversion will have noticed that the signal amplitudes were blatantly ignored so far, even though they are crucial for constraining

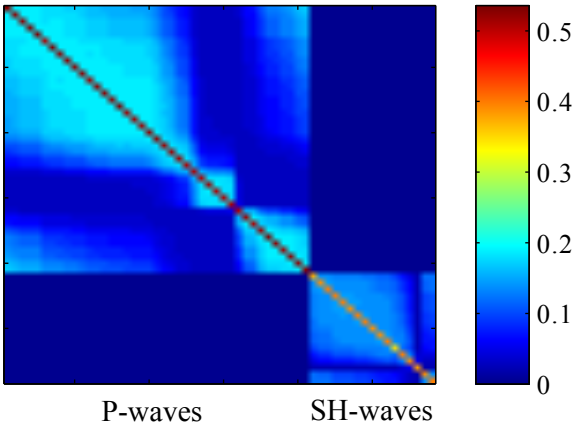

Figure 4.3: Covariance matrix of eq. 4.11 for the Virginia event. The block structure results from the fact that P and SH-waves are being treated as uncorrelated. Since stations are sorted by azimuth, the values close to the main diagonal are biggest.

the source orientation. To use them, a second measurement is done on the waveform, which is simply to compare the logarithmic energy content $\ln(A)$ in a 1s time window around the peak of the signal and the synthetic. Again, we have to check the distribution of this misfit to determine a likelihood. The distribution of $\Delta \ln(A)$ is almost symmetric around 0 (see fig. 4.2) and there is no physical reason, why it should not be, so we try to fit $|\Delta \ln(A)|$, since we have more data this way.
The amplitude misfit $|\Delta \ln(A)|$ follows an exponential distribution, where the parameter k does not vary much with SNR (see sect. 4.6.3).

$$L_{\text{Amp}} = \frac{1}{k} \exp\left(-\frac{|\Delta \ln(A)|}{k}\right) \tag{4.15}$$

4.4 Bayesian Inference

We apply Bayes' rule to obtain the posterior distribution

$$\pi(\vec{m}|\vec{d}) = \frac{L(\vec{d}|\vec{m})p(\vec{m})}{p(\vec{d})}. \tag{4.16}$$

Here, the unknown parameter vector $\vec{m}$ consists of depth, five moment tensor parameters and ten STF weights (Stähler and Sigloch, 2013) and is to be updated during the MCMC steps. The quantity $\vec{d}$ denote the realization of the random variables D for the data. For the prior distribution $p(m)$ we assume the follows:

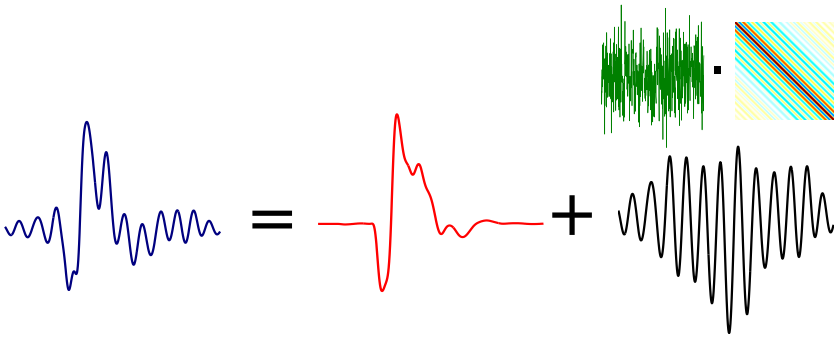

Figure 4.4: Noise model assumed by the ℓ^2 norm. A coloured noise (green) is added to the synthetic waveform (red), which is otherwise identical to the Earth's Greens function.

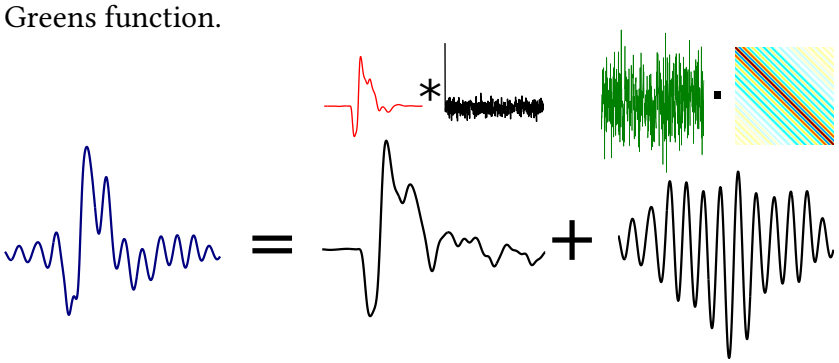

Figure 4.5: More realistic noise model: The Earth's Greens function is the synthetic waveform convolved with a transfer function plus background noise.

- $m_1 \sim \mathcal{U}(d_{\text{min}}, d_{\text{max}})$, the depth is distributed uniformly between d_{min} and d_{max}, which are chosen manually.

- The isotropic and CLVD content of the moment tensor should be as small as possible.

- The STF should have a vanishing negative part.

For the exact implementation, see Stähler and Sigloch (2013) (Chapter 3 in this thesis). For the sake of this study, it is important to state that the velocity model is fixed and the same as in the production of the distributions of D.

4.5 Discussion

4.5.1 Comparing waveforms

Traditionally, when comparing measured seismograms $u(t)$ with calculated synthetic waveforms $u^c(t)$, we apply the ℓ^2-norm, i.e. the Mahalanobis distance $L_M(u(t), u^c(t))$ with a covariance matrix S,

$$L_M(u(t), u^c(t)) = \sqrt{(u(t) - u^c(t))^T S^{-1} (u(t) - u^c(t))}. \tag{4.17}$$

The assumption behind this misfit however, is that the measured signal d is the signal predicted from the model $g(m)$ plus additional multivariate normal distributed noise, $d \sim \mathcal{N}(0, S)$ with the covariance matrix S. For one waveform of one seismic station, S is a Toeplitz-matrix, where the elements are the autocorrelation function R_{nn} of the (discrete) noise time series $n(t) = n(t_0 + \Delta t \cdot i) = n_i$

$$s_j = S_{k,k+j} = R_{nn}(j) = \sum_i n_i n_{i-j} \tag{4.18}$$

This covariance matrix S describes mainly the band-limitedness of the background noise $n(t)$ at this station. If more than one station is involved, it is a block diagonal matrix, if the noise between the stations is uncorrelated or more complicated, if the noise between the stations is correlated.
What this approach fails to attend is that the difference between a synthetic and a real seismogram comes not only from the presence of background noise. Due to characteristics of the data errors we consider as major factors that cause the difference between synthetic and real seismogram:

1. **Background noise**: This is noise from human or natural sources around the receiver, be it ocean generated or the archetypical truck or sawmill. This noise can be described very well by an additional term of like $\epsilon_{\text{noise}} \sim \mathcal{N}(0, S)$.

2. **Modelling error**: The velocity model used by the forward solver is not identical to the velocity of the earth on the scale of the smallest wavelengths used. Therefore, the synthetic waveform can never be identical to the real one, even in absence of background noise. Tarantola and Valette (1982, sect. 5) called this the *theoretical density function* and proposed another Gaussian term for it. We think that the modelling error should not be described by an additive term. Since the earth can be described as a linear operator acting on the source wavelet (aka the Green's Function), this error takes the form of a transfer function, denoted by $T_{\text{model}}(t)$, between the real seismogram $u(t)$ and the synthetic seismogram of the true

source model $u^{\mathrm{c}}(t)$. This error includes the site response, which has usually largest influence on the amplitude of the waveform.

3. **Instrument error**: A seismometer has its own impulse response, which distorts the real seismogram further. This error can also be described by a transfer function $T_{\mathrm{inst}}(t)$. The determination of $T_{\mathrm{inst}}(t)$ is a science in its own (Bogert, 1962). For permanent stations, the correction of the instrument error should be reliable, however, we still find it to be wrong for around one station in a thousand.

To conclude, while the ℓ^2-norm with a covariance matrix assumes that the measured signal $u(t)$ is the "true" signal plus a noise term $\epsilon_{\mathrm{noise}}$, the reality is that the measured signal is the true signal convolved with a transfer function from the modelling error and one from the instrument response.

$$u(t) = u^{\mathrm{c}}(t) * T_{\mathrm{model}}(t) * T_{\mathrm{inst}}(t) + \epsilon_{\mathrm{noise}} \tag{4.19}$$

This may seem as bad news, since we do not have any way to determine $T_{\mathrm{model}}(t)$ analytically. If our forward solver was using the true velocity model of the earth and if it incorporated all the physics of the source process, this term would be the identity operator. For a simplified earth model like IASP91, it is obviously far from that. Using a more sophisticated 3D velocity model of the earth, we could push $T_{\mathrm{model}}(t)$ so far towards identity, that we could neglect it and concentrate on the background noise. However, it is far cheaper computationally to calculate seismograms in a 1D earth model, with some crustal corrections, so in terms of Bayesian inference by sampling, it might be worth to use a bad model but draw a lot more samples from the model space[1]. Therefore, we find the pragmatic definition of (Scales et al., 1998) rather useful:

> Noise is the part of data we choose not to explain.

And what we do not explain is anything in the predicted data that cannot be improved by changing model parameters.

4.6 Likelihood distribution parameters

4.6.1 μ and σ

To estimate the likelihood distribution of new earthquakes, we need to have an analytical fit function of the distribution parameters $\mu_{\mathrm{P}}, \mu_{\mathrm{SH}}, \sigma_{\mathrm{P}}, \sigma_{\mathrm{SH}}$ in dependence of SNR. Figure 4.6 show the parameters with fit functions $h(\mathrm{SNR}) =$

[1] In fact, we do not have a choice here. It is just not possible to include all physics into our forward simulation, even with more and more detailed velocity models.

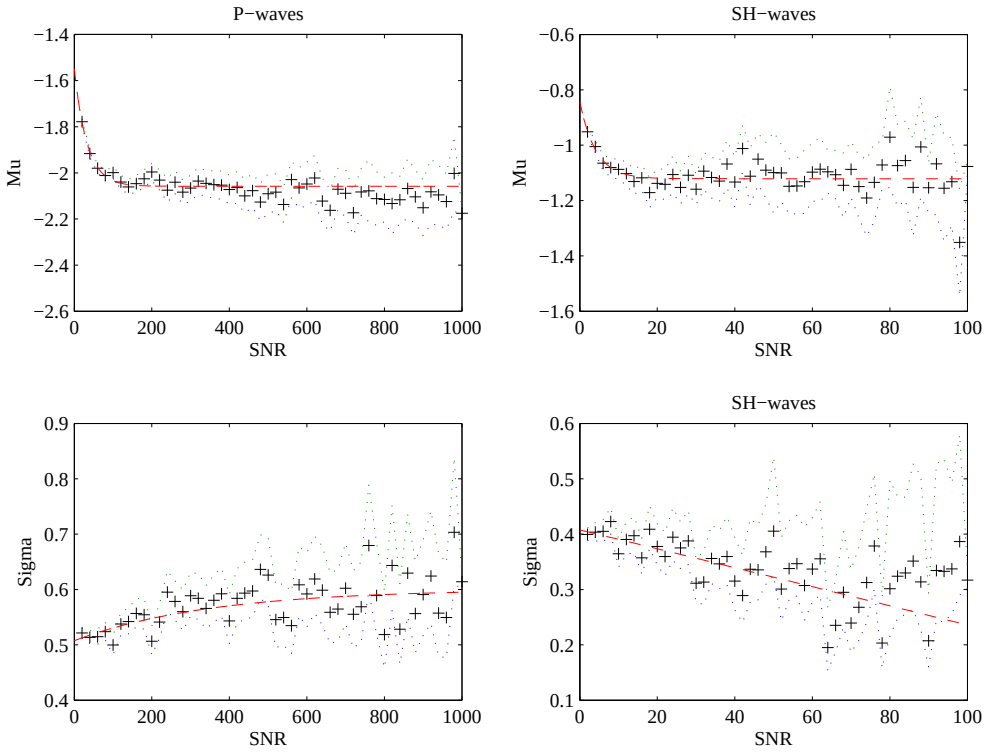

Figure 4.6: Distribution of parameters $\mu_{\mathrm{P}}, \mu_{\mathrm{SH}}, \sigma_{\mathrm{P}}, \sigma_{\mathrm{SH}}$ for different SNR, compared with the fitting function $h(\mathrm{SNR}) = a_1 + a_2 \cdot \exp(-a_3 \cdot \mathrm{SNR})$ (red dashed). The dotted lines show confidence intervals of the parameters estimated by the bootstrapping method.

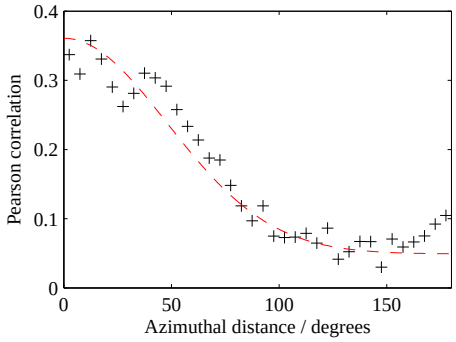

Figure 4.7: Dependance of Pearson covariance between the decorrelation D on the distance ϑ.

	a_1	a_2	a_3
μ_{P}	-2.06	0.51	0.031
σ_{P}	0.6	-0.093	$2.8 \cdot 10^{-3}$
μ_{SH}	-1.12	0.28	0.24
σ_{SH}	6.7	-6.3	$-2.7 \cdot 10^{-4}$

Table 4.2: Fit parameters to calculate μ and σ for the waveform misfit coefficient given a SNR.

	b_1	b_2	b_3
$r(\vartheta)$	0.049	0.31	$2.17 \cdot 10^{-4}$

Table 4.3: Parameters b_1, b_2, b_3 to calculate the inter-station correlation depending on azimuthal distance

$a_1 + a_2 \cdot \exp(-a_3 \cdot \mathrm{SNR})$. The confidence intervals were estimated using the bootstrapping method.

4.6.2 Station correlation

The inter-station correlation was calculated as described in section 4.3.3 and is shown in fig. 4.7. To fit it, the function $g(\vartheta) = b_1 + b_2 \cdot \exp(-b_3 \cdot \vartheta^2)$ was used, with the following parameters as a result: The fit function follows the values well, although there is a non-explained rise from $160°$ on. We think that this is an artefact of imperfectly determined focal mechanisms. Especially strike-slip events have a quadrupole radiation pattern, where errors in the strike parameter will influence stations at $0°, 90°, 180°$ and $270°$. If that explanation was true, there should be another peak at $90°$, which is lost here.

4.6.3 Amplitudes

The amplitude misfit follows an exponential distribution $|\Delta A_i - \mathrm{median}(\Delta A_i)| \sim \mathrm{Exp}(k)$, where k takes the values 0.2 and 0.1 for P and SH respectively.

4.7 Conclusions

This chapter presents an approach to employ Bayesian inference in the presence of unknown noise. From a large set of established solutions to the source inversion problem, we derived the distribution of a waveform misfit parameter (the correlation coefficient) due to modelling error and noise. This approach allows to infer a Likelihood function without a noise model at hand. This approach could

replace simplistic assumptions on data variance in other seismological inverse problems, especially seismic tomography.

And it shall be, when thou hast made an end of reading this book, that thou shalt bind a stone to it, and cast it into the midst of Euphrates

Jeremiah 51:63

5 Conclusion

The scope of the thesis was to improve finite-frequency tomography from the original ray-bases kernels for simple waves to more arbitrary ones, especially triplicated ones from the mantle transition zone. Using the reflectivity method for seismogram simulation, this has been shown to be possible. With the AxiSEM spectral-element solver, it is fundamentally possible to calculate sensitivity kernels for a seismic tomography. This has also been shown in chapter 2. However, it was not yet possible to do an actual tomography using these waveforms. This will be the obvious next step after the work presented in this thesis.

Such a tomography should then also include the probabilistic traveltime estimates from the Bayesian source inversion presented in chapters 3 and 4. A regular, linear inversion will profit from a correct estimation of the data covariance matrix, but at a later stage, a probabilistic for a model with reduced dimensionality would be possible to directly invert for the answer to geological questions, like "is there a plume under La Réunion and where does it start?".

In themselves, the results of the probabilistic source inversion can be given to the seismological community in form of a source catalogue containing not only best-fitting models, but also correct uncertainties. When the whole statistical ensemble of possible source solutions for a large number of earthquakes is used, the whole power of Bayesian inference can be used for the analyses of the distribution of earthquake parameters. These studies have hitherto been unconsciously affected by the reduction of probability density functions to just one "best solution", by someone else.

This is a benefit for geological and tectonic interpretation of earthquake source parameters as well. Working with probability density functions, combination with completely different data, like surface fault expression is possible and would allow true hypothesis testing. Inverse problems in Earth sciences seem to have a high dimensionality, which makes them difficult to solve. However, the intrinsic dimensionality is often rather small, if the problem is reduced to accepting or rejecting hypotheses.

While this thesis alone has not improved our understanding of the Earth, it will give seismologists and other earth scientists new tools for the next years to continue their curious task of inferring a four-dimensional system from some time series on a two-dimensional plane.

Bibliography

Keiiti Aki and Paul G Richards. *Quantitative Seismology*, volume II. University Science Books, 2nd editio edition, 2002. ISBN 0935702962. 46

Kai-Henrik Barth. The Politics of Seismology: Nuclear Testing, Arms Control, and the Transformation of a Discipline. *Social Studies of Science*, 33(5):743–781, October 2003. ISSN 03063127. doi: 10.1177/0306312703335005. 2

C. Bassin, Gabi Laske, and Guy Masters. The Current Limits of Resolution for Surface Wave Tomography in North America. In *EOS Trans AGU*, volume 81, page F897, 2000. 4, 47, 56

Charles C. Bates. VELA UNIFORM, the nation's quest for better detection of underground nuclear explosions. *Geophysics*, 26(4):499–507, August 1961. ISSN 0016-8033. doi: 10.1190/1.1438905. 2

Thorsten W. Becker. On recent seismic tomography for the western United States. *Geochemistry Geophysics Geosystems*, 13(1):1–11, March 2012. ISSN 1525-2027. doi: 10.1029/2011GC003977. 36

Thorsten W. Becker and Lapo Boschi. A comparison of tomographic and geodynamic mantle models. *Geochemistry, Geophysics, Geosystems*, 3(1), January 2002. ISSN 15252027. doi: 10.1029/2001GC000168. 4

Thomas Bodin, Malcolm Sambridge, Nick Rawlinson, and Pierre Arroucau. Transdimensional tomography with unknown data noise. *Geophysical Journal International*, pages no–no, April 2012. ISSN 0956540X. doi: 10.1111/j.1365-246X.2012.05414.x. 67

C Boehm and M Ulbrich. A Newton-CG Method for Full-Waveform Inversion in a Coupled Solid-Fluid System. In Michael Bader, Hans-Joachim Bungartz, and Tobias Weinzierl, editors, *Advanced Computing*, pages 99–117. Springer Berlin Heidelberg, Berlin, Heidelberg, 2013. ISBN 978-3-642-38762-3. doi: 10.1007/978-3-642-38762-3_5. 5

BP Bogert. Correction of seismograms for the transfer function of the seismometer. *Bulletin of the Seismological Society of America*, 52(4):781—-792, 1962. 77

István Bondár and Keith McLaughlin. Seismic Location Bias and Uncertainty in the Presence of Correlated and Non-Gaussian Travel-Time Errors. *Bulletin of the Seismological Society of America*, 99(1):172–193, February 2009. ISSN 0037-1106. doi: 10.1785/0120080922. 66

István Bondár and Dmitry A. Storchak. Improved location procedures at the International Seismological Centre. *Geophysical Journal International*, 186: 1220–1244, July 2011. ISSN 0956540X. doi: 10.1111/j.1365-246X.2011.05107.x. 62, 64

Keith Edward Bullen. Seismology in our atomic age. *Compt. Rend. Assoc. Seismol. et Phys. Int. Terre, Strasbourg*, 12:19–35, 1958. 2

Aimin Cao and Alan Levander. High-resolution transition zone structures of the Gorda Slab beneath the western United States: Implication for deep water subduction. *Journal of Geophysical Research*, 115(B7):B07301, July 2010. ISSN 0148-0227. doi: 10.1029/2009JB006876. 27

Emmanuel Chaljub and Albert Tarantola. Sensitivity of SS precursors to topography on the upper-mantle 660-km discontinuity. *Geophysical Research Letters*, 24(21):PP. 2613–2616, 1997. doi: 199710.1029/97GL52693. 12

Christopher Hugh Chapman. A new method for computing synthetic seismograms. *Geophysical Journal of the Royal Astronomical Society*, 54:481–518, 1978. 19, 47

M. C. Chapman. On the Rupture Process of the 23 August 2011 Virginia Earthquake. *Bulletin of the Seismological Society of America*, 103(2A):613–628, March 2013. ISSN 0037-1106. doi: 10.1785/0120120229. 57

Risheng Chu, Brandon Schmandt, and Don V. Helmberger. Upper mantle P velocity structure beneath the Midwestern United States derived from triplicated waveforms. *Geochemistry Geophysics Geosystems*, 13(1):1–21, February 2012. ISSN 1525-2027. doi: 10.1029/2011GC003818. 30

Andrea Colombi, Tarje Nissen-Meyer, Lapo Boschi, and Domenico Giardini. Seismic waveform sensitivity to global boundary topography. *Geophysical Journal International*, 191(2):832–848, November 2012. ISSN 0956540X. doi: 10.1111/j.1365-246X.2012.05660.x. 26, 36

F. A. Dahlen, Shu-Huei Hung, and Guust Nolet. Fréchet kernels for finite-frequency traveltimes - I. Theory. *Geophysical Journal International*, 141(1): 157–174, April 2000. ISSN 1365-246X. doi: 10.1046/j.1365-246X.2000.00070.x. 5, 6, 11, 19, 20, 21, 22, 25, 34

Arwen Deuss. Global observations of mantle discontinuities using SS and PP precursors. *Surveys in geophysics*, 30(4):301–326, 2009. ISSN 0169-3298. doi: 10.1007/s10712-009-9078-y. 12

Arwen Deuss, Simon A. T. Redfern, Kit Chambers, and John H. Woodhouse. The Nature of the 660-Kilometer Discontinuity in Earth's Mantle from Global Seismic Observations of PP Precursors. *Science*, 311(5758):198–201, January 2006. doi: 10.1126/science.1120020. 12

Wojciech Dębski. Estimating the Earthquake Source Time Function by Markov Chain Monte Carlo Sampling. *Pure and Applied Geophysics*, 165(7):1263–1287, 2008. ISSN 0033-4553. doi: 10.1007/s00024-008-0357-1. 41, 62, 64

Adam M. Dziewoński. Mapping the lower mantle: Determination of lateral heterogeneity in P velocity up to degree and order 6. *Journal of Geophysical Research: Solid Earth*, 89(B7):5929–5952, 1984. ISSN 2156-2202. doi: 10.1029/JB089iB07p05929. 3

Adam M. Dziewoński and Don L. Anderson. Preliminary reference Earth model. *Physics of the Earth and Planetary Interiors*, 25(4):297–356, June 1981. ISSN 00319201. doi: 10.1016/0031-9201(81)90046-7. 3, 17, 47

Adam M. Dziewoński, A.L. Hales, and E.R. Lapwood. Parametrically simple Earth models consistent with geophysical data. *Physics of the Earth and Planetary Interiors*, 10(1):12–48, May 1975. ISSN 00319201. doi: 10.1016/0031-9201(75)90017-5. 2

Adam M. Dziewoński, Bradford H Hager, and Richard J O'Connell. Large-scale heterogeneities in the lower mantle. *Journal of Geophysical Research*, 82(2): 239–255, 1977. ISSN 2156-2202. doi: 10.1029/JB082i002p00239. 3

Adam M. Dziewoński, T.-A. Chou, and John H. Woodhouse. Determination of Earthquake Source Parameters From Waveform Data for Studies of Global and Regional Seismicity. *Journal of Geophysical Research*, 86(B4):2825–2852, 1981. ISSN 0148-0227. doi: 10.1029/JB086iB04p02825. 3, 35, 62

Göran Ekström, M. Nettles, and Adam M. Dziewoński. The global CMT project 2004–2010: Centroid-moment tensors for 13,017 earthquakes. *Physics of the*

Earth and Planetary Interiors, 200-201:1–9, June 2012. ISSN 00319201. doi: 10.1016/j.pepi.2012.04.002. 62, 64

Andreas Fichtner and Jeannot Trampert. Hessian kernels of seismic data functionals based upon adjoint techniques. *Geophysical Journal International*, 185 (2):775–798, May 2011. ISSN 0956540X. doi: 10.1111/j.1365-246X.2011.04966.x. 5, 68

Andreas Fichtner, B. L. N. Kennett, Heiner Igel, and Hans-Peter Bunge. Full seismic waveform tomography for upper-mantle structure in the Australasian region using adjoint methods. *Geophysical Journal International*, 179(3):1703–1725, December 2009. ISSN 0956540X. doi: 10.1111/j.1365-246X.2009.04368.x. 34, 68

Andreas Fichtner, Florian Bleibinhaus, and Yann Capdeville. *Full seismic waveform modelling and inversion*. Springer, 2011. 5

K. Fuchs and Gerhard Müller. Computation of Synthetic Seismograms with the Reflectivity Method and Comparison with Observations. *Geophysical Journal of the Royal Astronomical Society*, 23(4):417–433, September 1971. ISSN 1365-246X. doi: 10.1111/j.1365-246X.1971.tb01834.x. 17

Yoshio Fukao, Masayuki Obayashi, and Tomoeki Nakakuki. Stagnant Slab: A Review. *Annual Review of Earth and Planetary Sciences*, 37(1):19–46, 2009. ISSN 0084-6597. doi: 10.1146/annurev.earth.36.031207.124224. 37

R. F. Garcia, L. Schardong, and S. Chevrot. A Nonlinear Method to Estimate Source Parameters, Amplitude, and Travel Times of Teleseismic Body Waves. *Bulletin of the Seismological Society of America*, 103(1):268–282, February 2013. ISSN 0037-1106. doi: 10.1785/0120120160. 40, 62, 64

Stuart Geman and Donald Geman. Stochastic relaxation, Gibbs distributions, and the Bayesian restoration of images. *IEEE Transactions on Pattern Analysis and Machine Intelligence*, 6(6):721 – 741, 1984. doi: 10.1109/TPAMI.1984.4767596. 53

Slawomir J Gibowicz. Chapter 1 - Seismicity Induced by Mining: Recent Research. In Renata Dmowska B T Advances in Geophysics, editor, *Advances in Geophysics*, volume Volume 51, pages 1–53. Elsevier, 2009. ISBN 0065-2687. doi: http://dx.doi.org/10.1016/S0065-2687(09)05106-1. 40

Walter R. Gilks, Sylvia Richardson, and David J. Spiegelhalter. *Markov Chain Monte Carlo in Practice*. Chapman & Hall/CRC, London, 1996. ISBN 9780412055515. 66

S.P. Grand. Upper mantle shear structure of North America. *Geophysical Journal of the Royal Astronomical Society*, 76(2):399–438, 1984. ISSN 0956-540X. doi: 10.1111/j.1365-246X.1984.tb05053.x. 11

S.P. Grand. Mantle shear structure beneath the Americas and surrounding oceans. *Journal of Geophysical Research*, 99(B6):11591–11, June 1994. doi: 10.1029/94JB00042. 16

S.P. Grand. Mantle shear–wave tomography and the fate of subducted slabs. *Philosophical Transactions of the Royal Society of London. Series A: Mathematical, Physical and Engineering Sciences*, 360(1800):2475, November 2002. ISSN 1364503X. doi: 10.1098/rsta.2002.1077. 12, 16

D. T. Griggs and Frank Press. Probing the Earth with nuclear explosions. *Journal of Geophysical Research*, 66(1):237–258, January 1961. ISSN 01480227. doi: 10.1029/JZ066i001p00237. 2

Beno Gutenberg. Über die Konstitution des Erdinnern, erschlossen aus Erdbebenbeobachtungen. *Physikalische Zeitschrift*, 14:1217–1218, 1913. 2

Beno Gutenberg. Untersuchungen zur Frage, bis zu welcher Tiefe die Erde kristallin ist. *Zeitschrift für Geophysik*, 2:24–29, 1926. 2

W.K. Hastings. Monte Carlo Sampling Methods Using Markov Chains and Their Applications. *Biometrika*, 57(1):97–109, 1970. doi: 10.1093/biomet/57.1.97. 53

Christine Houser, Guy Masters, M. Flanagan, and Peter M. Shearer. Determination and analysis of long-wavelength transition zone structure using SS precursors. *Geophysical Journal International*, 174(1):178–194, July 2008. ISSN 0956540X. doi: 10.1111/j.1365-246X.2008.03719.x. 32

Heidi Houston. Influence of depth, focal mechanism, and tectonic setting on the shape and duration of earthquake source time functions. *Journal of Geophysical Research*, 106(B6):11137–11150, 2001. ISSN 01480227. 40, 44, 58

Harold Jeffreys. The Rigidity of the Earth's Central Core. *Geophysical Journal of the Royal Astronomical Society*, 1(3):371–383, June 1926. ISSN 0956540X. doi: 10.1111/j.1365-246X.1926.tb05385.x. 2

Harold Jeffreys. The times of P, S and SKS, and the velocities of P and S. *Geophysical Supplements to the Monthly Notices of the Royal Astronomical Society*, 4(7):498–533, 1939. 1

Harold Jeffreys. Travel Times for Pacific Explosions. *Geophysical Journal of the Royal Astronomical Society*, 7(2):212–219, December 1962. ISSN 0956-540X. doi: 10.1111/j.1365-246X.1962.tb00370.x. 2

Harold Jeffreys and Keith Edward Bullen. *Seismological tables*. Office of the British Association for the Advancement of Science, London, 1940. 2

Y. Y. Kagan. 3-D rotation of double-couple earthquake sources. *Geophysical Journal International*, 106:709–716, 1991. doi: 10.1111/j.1365-246X.1991.tb06343.x. 60

B. L. N. Kennett. *The Seismic Wavefield: Introduction and theoretical development*. Cambridge University Press, 2001. ISBN 0521006635. 3, 14

B. L. N. Kennett and E. R. Engdahl. Traveltimes for global earthquake location and phase identification. *Geophysical Journal International*, 105(2):429–465, 1991. doi: 10.1111/j.1365-246X.1991.tb06724.x. 14, 15, 17, 47

B. L. N. Kennett and Andreas Fichtner. A unified concept for comparison of seismograms using transfer functions. *Geophysical Journal International*, 191(3):1403–1416, October 2012. ISSN 0956540X. doi: 10.1111/j.1365-246X.2012.05693.x. 68

B. L. N. Kennett, K. Marson-Pidgeon, and Malcolm Sambridge. Seismic Source characterization using a neighbourhood algorithm. *Geophysical Research Letters*, 27(20):3401, 2000. ISSN 0094-8276. doi: 10.1029/2000GL011559. 60, 62

B Y Masayuki Kikuchi and Hiroo Kanamori. Inversion of complex body waves - III. *Bulletin of the Seismological Society of America*, 81(6):2235–2350, 1991. 69

S. Kirkpatrick, C. D. Gelatt, and M. P. Vecchi. Optimization by simulated annealing. *Science*, 220(4598):671, 1983. doi: 10.1126/science.220.4598.671. 40, 64

P. Kolář. Two attempts of study of seismic source from teleseismic data by simulated annealing non-linear inversion. *Journal of Seismology*, 4(2):197–213, 2000. doi: 10.1023/A:1009828401090. 62, 64

Dimitri Komatitsch and Jeroen Tromp. Spectral-element simulations of global seismic wave propagation—II. Three-dimensional models, oceans, rotation and self-gravitation. *Geophysical Journal International*, 150(1):303–318, 2002a. doi: 10.1046/j.1365-246X.2002.01716.x. 3

Dimitri Komatitsch and Jeroen Tromp. Spectral-element simulations of global seismic wave propagation—I. Validation. *Geophysical Journal International*, 149 (2):390–412, 2002b. doi: 10.1046/j.1365-246X.2002.01653.x. 22

Dimitri Komatitsch and Jean-Pierre Vilotte. The spectral element method: An efficient tool to simulate the seismic response of 2D and 3D geological structures. *Bulletin of the Seismological Society of America*, 88(2):368–392, 1998. 3

Samuel Kotz, Tomasz J. Kozubowski, and Krzysztof Podgórski. *The Laplace Distribution and Generalizations: A Revisit With Applications to Communications, Economics, Engineering, and Finance*. Springer, 2001. ISBN 9780817641665. 67

Tomasz J. Kozubowski, Krzysztof Podgórski, and Igor Rychlik. Multivariate generalized Laplace distribution and related random fields. *Journal of Multivariate Analysis*, 113:59–72, January 2013. ISSN 0047259X. doi: 10.1016/j.jmva.2012.02.010. 67

Keiko Kuge and Thorne Lay. Data-dependent non-double-couple components of shallow earthquake source mechanisms: Effects of waveform inversion instability. *Geophysical Research Letters*, 21(1):9–12, 1994. 53

Eric Larose, Thomas Planes, Vincent Rossetto, and Ludovic Margerin. Locating a small change in a multiple scattering environment. *Applied Physics Letters*, 96: 2010–2012, 2010. doi: 10.1063/1.3431269. 69

Thorne Lay and Tianrun Zhang. Near-source contributions to teleseismic P waves and P-wave coda for underground explosions. *Bulletin of the Seismological Society of America*, 82(1):383–405, 1992.

Inge Lehmann. P'. *Bureau Central Séismologique International, Série A, Travaux Scientifiques*, 14:87–115, 1936. 2

Inge Lehmann. S and the Structure of the Upper Mantle. *Geophysical Journal of the Royal Astronomical Society*, 4:124–138, January 1961. ISSN 0956540X. doi: 10.1111/j.1365-246X.1937.tb07108.x. 2

Prasanta Chandra Mahalanobis. On the generalized distance in statistics. *Proceedings of the National Institute of Sciences of India*, 2(1):49–55, 1936. 71

Henk Marquering, F. A. Dahlen, and Guust Nolet. Three-dimensional sensitivity kernels for finite-frequency traveltimes: the banana-doughnut paradox. *Geophysical Journal International*, 137(3):805–815, June 1999. ISSN 0956-540X. doi: 10.1046/j.1365-246x.1999.00837.x. 5, 20

K. Marson-Pidgeon and B. L. N. Kennett. Source depth and mechanism inversion at teleseismic distances using a neighborhood algorithm. *Bulletin of the Seismological Society of America*, 90(6):1369–1383, December 2000. ISSN 0037-1106. doi: 10.1785/0120000020. 64, 69

Timothy I. Melbourne and Don V. Helmberger. Whole mantle shear structure beneath the East Pacific Rise. *Journal of Geophysical Research*, 107(B9):2204, September 2002. doi: 10.1029/2001JB000332. 12

Andrija Mohorovičić. Das Beben vom 8. Oktober 1909 (translated title). *Jahrbuch des meteorologischen Observatoriums in Zagreb*, 4(1):1–67, 1909. 1

Irene Molinari and Andrea Morelli. EPcrust: a reference crustal model for the European Plate. *Geophysical Journal International*, 185(1):352–364, April 2011. ISSN 0956540X. doi: 10.1111/j.1365-246X.2011.04940.x. 4

Raffaella Montelli, Guust Nolet, F. A. Dahlen, Guy Masters, E. R. Engdahl, and Shu-Huei Hung. Finite-frequency tomography reveals a variety of plumes in the mantle. *Science*, 303(5656):338–343, January 2004. ISSN 1095-9203. doi: 10.1126/science.1092485. 5, 11, 21

Raffaella Montelli, Guust Nolet, F. A. Dahlen, and Guy Masters. A catalogue of deep mantle plumes: New results from finite-frequency tomography. *Geochemistry Geophysics Geosystems*, 7(11):Q11007, November 2006. ISSN 1525-2027. doi: 10.1029/2006GC001248. 5

Klaus Mosegaard and Malcolm Sambridge. Monte Carlo analysis of inverse problems. *Inverse Problems*, 18:29–54, 2002. doi: 10.1088/0266-5611/18/3/201.

Gerhard Müller. The reflectivity method: a tutorial. *Zeitschrift für Geophysik/Journal of Geophysics*, 58:153–174, 1985. 37

Tarje Nissen-Meyer. *Full-wave seismic sensitivity in a spherical Earth*. PhD thesis, Princeton, 2007. 5, 6

Tarje Nissen-Meyer, F. A. Dahlen, and Alexandre Fournier. Spherical-earth Fréchet sensitivity kernels. *Geophysical Journal International*, 168 (3):1051–1066, March 2007a. ISSN 1365-246X. doi: 10.1111/j.1365-246X.2006.03123.x. 21, 24, 26

Tarje Nissen-Meyer, Alexandre Fournier, and F. A. Dahlen. A two-dimensional spectral-element method for computing spherical-earth seismograms–I. Moment-tensor source. *Geophysical Journal International*, 168 (3):1067–1092, March 2007b. ISSN 1365-246X. doi: 10.1111/j.1365-246X.2006.03121.x. 11, 24, 34, 37

Tarje Nissen-Meyer, Alexandre Fournier, and F. A. Dahlen. A 2-D spectral-element method for computing spherical-earth seismograms-II. Waves in solid-fluid media. *Geophysical Journal International*, 174(3):873–888, September 2008. ISSN 0956540X. doi: 10.1111/j.1365-246X.2008.03813.x. 24

Tarje Nissen-Meyer, Martin van Driel, Simon C. Stähler, Kasra Hosseini, Stefanie Hempel, Ludwig Auer, Andrea Colombi, and Alexandre Fournier. AxiSEM: broadband 3-D seismic wavefields in axisymmetric media. *Solid Earth*, 5(1): 425–445, June 2014. ISSN 1869-9529. doi: 10.5194/se-5-425-2014. 3

Guust Nolet. *A breviary of seismic tomography: imaging the interior of the earth and sun.* Cambridge University Press, 2008. ISBN 0521882443. 19, 48, 49

Eiji Ohtani. Water in the mantle. *Elements*, 1(1):25, January 2005. ISSN 1811-5209. doi: 10.2113/gselements.1.1.25. 25

Richard Dixon Oldham. On the Propagation of Earthquake Motion to Great Distances. *Philosophical Transactions of the Royal Society A: Mathematical, Physical and Engineering Sciences*, 194(252-261):135–174, January 1900. ISSN 1364-503X. doi: 10.1098/rsta.1900.0015. 1

Richard Dixon Oldham. The Constitution of the Interior of the Earth, as Revealed by Earthquakes. *Quarterly Journal of the Geological Society*, 62(1-4):456–475, February 1906. ISSN 0370-291X. doi: 10.1144/GSL.JGS.1906.062.01-04.21. 1

Gary L Pavlis, Karin Sigloch, Scott Burdick, Matthew J Fouch, and F. L. Vernon. Unraveling the Geometry of the Farallon Plate: Synthesis of Three-dimensional Imaging Results from USArray. *Tectonophysics*, 532–535:82–102, February 2012. ISSN 00401951. doi: 10.1016/j.tecto.2012.02.008. 36

Fuhao Qin, Yi Luo, Kim B. Olsen, Wenying Cai, and Gerard T. Schuster. Finite-difference solution of the eikonal equation along expanding wavefronts. *Geophysics*, 57(3):478–487, March 1992. ISSN 0016-8033. doi: 10.1190/1.1443263. 5

Nick Rawlinson and Malcolm Sambridge. Wave front evolution in strongly heterogeneous layered media using the fast marching method. *Geophysical Journal International*, 156(3):631–647, March 2004. ISSN 0956540X. doi: 10.1111/j.1365-246X.2004.02153.x. 5

A. E. Ringwood. *Composition and Petrology of the Earth's Mantle*, volume 618 of *McGraw-Hill international series in the earth and planetary sciences.* McGraw-Hill New York, New York [u.a.], 1975. ISBN 0-07-052932-9. 37

Jeroen Ritsema, H.J. Heijst, and John H. Woodhouse. Complex shear wave velocity structure imaged beneath Africa and Iceland. *Science*, 286(5446):1925, December 1999. ISSN 00368075. doi: 10.1126/science.286.5446.1925. 3

Jeroen Ritsema, Arwen Deuss, H. J. van Heijst, and John H. Woodhouse. S40RTS: a degree-40 shear-velocity model for the mantle from new Rayleigh wave dispersion, teleseismic traveltime and normal-mode splitting function measurements. *Geophysical Journal International*, 184(3):1223–1236, March 2011. ISSN 0956540X. doi: 10.1111/j.1365-246X.2010.04884.x. 4

L. J. Ruff. Multi-trace deconvolution with unknown trace scale factors: Omnilinear inversion of P and S waves for source time functions. *Geophysical Research Letters*, 16(9):1043–1046, September 1989. ISSN 00948276. doi: 10.1029/GL016i009p01043. 40

Malcolm Sambridge. Exploring multidimensional landscapes without a map. *Inverse Problems*, 14(3):427–440, June 1998. ISSN 0266-5611. doi: 10.1088/0266-5611/14/3/005. 53

Malcolm Sambridge. Geophysical inversion with a neighbourhood algorithm – I . Searching a parameter space. *Geophysical Journal International*, 138(2): 479–494, 1999a. doi: 10.1046/j.1365-246X.1999.00876.x. 40, 41, 53

Malcolm Sambridge. Geophysical inversion with a neighbourhood algorithm – II . Appraising the ensemble. *Geophysical Journal International*, 138(3):727–746, 1999b. doi: 10.1046/j.1365-246x.1999.00900.x. 41, 53, 64

Malcolm Sambridge and B. L. N. Kennett. Seismic event location: nonlinear inversion using a neighbourhood algorithm. *Pure and Applied Geophysics*, 158 (1):241–257, 2001. ISSN 00334533. doi: 10.1007/PL00001158. 60, 62, 64

John A. Scales, Roel Snieder, and John Gay. What is noise ? *Geophysics*, 63(4): 1122–1124, 1998. doi: 10.1190/1.1444411. 77

Peter M. Shearer and Guy Masters. Global mapping of topography on the 660km discontinuity. *Nature*, 355:791–796, 1992. 12

Karin Sigloch. *Multiple-frequency body-wave tomography*. PhD thesis, Princeton, 2008. 5, 6, 29

Karin Sigloch. Mantle provinces under North America from multifrequency P wave tomography. *Geochemistry Geophysics Geosystems*, 12:27 PP., February 2011. doi: 201110.1029/2010GC003421. 30, 35, 58

Karin Sigloch and Mitchell G Mihalynuk. Intra-oceanic subduction shaped the assembly of Cordilleran North America. *Nature*, 496(7443):50–6, April 2013. ISSN 1476-4687. doi: 10.1038/nature12019. 5

Karin Sigloch and Guust Nolet. Measuring finite-frequency body-wave amplitudes and traveltimes. *Geophysical Journal International*, 167(1):271–287, October 2006. ISSN 1365-246X. doi: 10.1111/j.1365-246X.2006.03116.x. x, 16, 18, 20, 29, 35, 40, 42, 43, 44, 48, 49, 58, 64, 68, 71

Karin Sigloch, Nadine McQuarrie, and Guust Nolet. Two-stage subduction history under North America inferred from multiple-frequency tomography. *Nature Geoscience*, 1(7):458–462, July 2008. ISSN 1752-0894. doi: 10.1038/ngeo231. 11, 21, 27

Simon C. Stähler and Karin Sigloch. Fully probabilistic seismic source inversion – Part 1: Efficient parameterisation. *Solid Earth Discussions*, 5(2):1125–1162, July 2013. ISSN 1869-9537. doi: 10.5194/sed-5-1125-2013. 39, 66, 74, 75

Simon C. Stähler, Karin Sigloch, and Tarje Nissen-Meyer. Triplicated P-wave measurements for waveform tomography of the mantle transition zone. *Solid Earth*, 3(2):339–354, 2012. doi: 10.5194/se-3-339-2012. 9, 40, 43, 71

Simon C. Stähler, Ran Zhang, and Karin Sigloch. Fully probabilistic seismic source inversion – Part 2: Estimating data (co)variances. *Solid Earth*, to be subm, 2014. 41, 49, 65

Eléonore Stutzmann, Geneviève Roult, and Luciana Astiz. GEOSCOPE station noise levels. *Bulletin of the Seismological Society of America*, 3(June):690–701, 2000. 71

S. Taber. Earthquakes in Buckingham County, Virginia. *Bulletin of the Seismological Society of America*, 3:124–133, 1913. 54

Fumiko Tajima and S.P. Grand. Evidence of high velocity anomalies in the transition zone associated with southern Kurile subduction zone. *Geophysical Research Letters*, 22(23):3139–3142, 1995. doi: 199510.1029/95GL03314. 12, 35

Fumiko Tajima, Ikuo Katayama, and Tsuyoshi Nakagawa. Variable seismic structure near the 660 km discontinuity associated with stagnant slabs and geochemical implications. *Physics of the Earth and Planetary Interiors*, 172(3-4): 183–198, February 2009. ISSN 0031-9201. doi: 10.1016/j.pepi.2008.09.013. 12, 35

Y. Tanioka and L. J. Ruff. Source Time Functions. *Seismological Research Letters*, 68(3):386–400, May 1997. ISSN 0895-0695. doi: 10.1785/gssrl.68.3.386. 58

Carl Tape, Qinya Liu, Alessia Maggi, and Jeroen Tromp. Adjoint tomography of the southern California crust. *Science*, 325(5943):988–92, August 2009. ISSN 1095-9203. doi: 10.1126/science.1175298. 5, 68

Walter Tape and Carl Tape. Angle between principal axis triples. *Geophysical Journal International*, 191(2):813–831, November 2012. ISSN 0956540X. doi: 10.1111/j.1365-246X.2012.05658.x. 60

Albert Tarantola. Inversion of seismic reflection data in the acoustic approximation. *Geophysics*, 49(8):1259–1266, August 1984. ISSN 1070485X. doi: 10.1190/1.1441754. 34

Albert Tarantola. *Inverse problem theory and methods for model parameter estimation*. SIAM, Philadelphia, 2005. ISBN 0898715725. 59

Albert Tarantola and Bernard Valette. Inverse problems = quest for information. *Journal of Geophysics*, 50:159–170, 1982. 76

Y Tashiro. On methods for generating uniform random points on the surface of a sphere. *Annals of the Institute of Statistical Mathematics*, 29:295–300, 1977. 46

Christine Thomas and M. I. Billen. Mantle transition zone structure along a profile in the SW Pacific: thermal and compositional variations. *Geophysical Journal International*, 176(1):113–125, 2009. 12

Yue Tian, Ying Zhou, Karin Sigloch, Guust Nolet, and Gabi Laske. Structure of North American mantle constrained by simultaneous inversion of multiple-frequency SH, SS, and Love waves. *Journal of Geophysical Research*, 116(B2), 2011. ISSN 0148-0227. doi: 10.1029/2010JB007704. 5, 11, 21

Hrvoje Tkalčić, Mallory Young, Thomas Bodin, Silvie Ngo, and Malcolm Sambridge. The shuffling rotation of the Earth's inner core revealed by earthquake doublets. *Nature Geoscience*, 6(6):497–502, May 2013. ISSN 1752-0894. doi: 10.1038/ngeo1813. 4

A. Tocheport, L. Rivera, and S. Chevrot. A systematic study of source time functions and moment tensors of intermediate and deep earthquakes. *Journal of Geophysical Research*, 112(B7):1–22, July 2007. ISSN 0148-0227. doi: 10.1029/2006JB004534. 58, 62, 64

Jeroen Tromp. Inner-core anisotropy and rotation. *Annual Review of Earth and Planetary Sciences*, (1936):47–69, 2001. 4

Jeroen Tromp, Carl Tape, and Qinya Liu. Seismic tomography, adjoint methods, time reversal and banana-doughnut kernels. *Geophysical Journal International*, 160(1):195–216, December 2005. ISSN 0956540X. doi: 10.1111/j.1365-246X.2004.02453.x. 21, 34

Martin Vallée. SCARDEC solution for the 23/08/2011 Virginia earthquake, 2012. 57

Martin Vallée, J. Charléty, Ana M. G. Ferreira, B. Delouis, and J. Vergoz. SCARDEC: a new technique for the rapid determination of seismic moment magnitude, focal mechanism and source time functions for large earthquakes using body-wave deconvolution. *Geophysical Journal International*, 184(1): 338–358, January 2011. ISSN 0956540X. doi: 10.1111/j.1365-246X.2010.04836.x. 40, 60, 63, 64

Rob van der Hilst, Sri Widiyantoro, and E. R. Engdahl. Evidence for deep mantle circulation from global tomography. *Nature*, 386(6625):578–584, 1997. ISSN 00280836. doi: 10.1038/386578a0. 3

J. C. VanDecar and R. S. Crosson. Determination of teleseismic relative phase arrival times using multi-channel cross-correlation and least squares. *Bulletin of the Seismological Society of America*, 80(1):150–169, February 1990. 16, 18

J. Virieux and Stéphane Operto. An overview of full-waveform inversion in exploration geophysics. *Geophysics*, 74(6):1—-26, November 2009. ISSN 0016-8033. doi: 10.1190/1.3238367. 5

E Von Rebeur-Paschwitz. The earthquake of Tokio, April 18, 1889. *Nature*, 40: 294–295, 1889. 1

M. Wathelet. An improved neighborhood algorithm: parameter conditions and dynamic scaling. *Geophysical Research Letters*, 35(9):1–5, May 2008. ISSN 0094-8276. doi: 10.1029/2008GL033256. 60

Zoltán Wéber. Probabilistic local waveform inversion for moment tensor and hypocentral location. *Geophysical Journal International*, 165(2):607–621, May 2006. ISSN 0956540X. doi: 10.1111/j.1365-246X.2006.02934.x. 41, 62, 64

Zoltán Wéber. Estimating source time function and moment tensor from moment tensor rate functions by constrained L 1 norm minimization. *Geophysical Journal International*, 178(2):889–900, August 2009. ISSN 0956540X. doi: 10.1111/j.1365-246X.2009.04202.x. 62

Ernst Wiechert. Über die Beschaffenheit des Erdinneren. *Schriften der Physikalisch-ökonomischen Gesellschaft zu Königsberg in Preußen, Sitzungsberichte*, pages 4–5, 1896. 1

Ernst Wiechert. Über die Massenverteilung im Inneren der Erde. *Nachrichten von der Gesellschaft der Wissenschaften zu Göttingen, Mathematisch-Physikalische Klasse*, 1897:221–243, 1897. 1

John H. Woodhouse and Adam M. Dziewoński. Mapping the upper mantle: Three-dimensional modeling of Earth structure by inversion of seismic waveforms. *Journal of Geophysical Research*, 89:5953–5986, 1984. 3

C Wright and K J Muirhead. Longitudinal waves from the Novaya Zemlya nuclear explosion of October 27, 1966, recorded at the Warramunga seismic array. *Journal of Geophysical Research*, 74(8):2034–2048, 1969. 2

Ying Zhou, F. A. Dahlen, and Guust Nolet. Three-dimensional sensitivity kernels for surface wave observables. *Geophysical Journal International*, 158(1): 142–168, July 2004. ISSN 0956540X. doi: 10.1111/j.1365-246X.2004.02324.x. 11, 21

Ying Zhou, Guust Nolet, F. A. Dahlen, and Gabi Laske. Global upper-mantle structure from finite-frequency surface-wave tomography. *Journal of Geophysical Research*, 111(B4):B04304, April 2006. ISSN 0148-0227. doi: 10.1029/2005JB003677. 11, 21

Hejun Zhu, Ebru Bozdağ, Daniel Peter, and Jeroen Tromp. Structure of the European upper mantle revealed by adjoint tomography. *Nature Geoscience*, 5(7): 493–498, June 2012. ISSN 1752-0894. doi: 10.1038/ngeo1501. 12, 34

Acknowledgements

It has been a wonderful experience to have four years of freedom to follow new tracks, to talk to big minds and sometimes have this weird feeling, that an idea that somebody, maybe even unknowingly, implanted in your mind, blossoms.

Besides everybody acknowledged in the single chapters, I want to thank my advisor Karin Sigloch, for being an excellent mentor and scientific guide. You always took the time to guide me through these four years and share your ideas with me. In this microcosm of vanity, you are one of the few persons that dares to ask honest and important questions, whether they might impress anybody else or not.

Heiner, with your incredible energy, your readiness to follow new ideas, your enthusiasm in organising great workshops, your ability to make any resource necessary available to your students, you're making the LMU seismology group a great place to work, even if you did not track every small step of my thesis.

Christoph Sens-Schönfelder, I could always rely on you to get a good judgement from outside the LMU bubble, even after our time in Leipzig.

I thank Michael Bader and Marcus Mohr for clearing any red tape issues, especially around the birth of our child, Jens Oeser and Gerald Schroll for a great IT system in the institute, Marion Jegen and Wolfram Geissler for taking me to the world's most remote island, Sherryl Kluver for looking after me in Canberra.

I thank my fellow Ph.D. students, Kasra H. with your courage and placidness, you were a great guy to share work and adventure with, Stefan W. for lighting up my live and helping me out of many a hole and together with Michael E. having the most underestimated room in the 4th floor, Christian P. for being my older brother in the first year, Céline H. for being an awesome geek and scientist, Martin v.D. for pursuing the challenge of finishing AxiSEM against all odds and never giving up to ask questions, Paul K. for being the only young person who seems to understand the importance of proper priors, and Julia L./K. for sharing the most important and confusing experience of all.

At last, this thesis and nothing else would have been possible without my parents putting me on the right track from the very beginning and supporting me whenever I was in need and my sister for getting me back to Earth whenever that was needed.

And at the very last you, P. for taking my hand and leading me through this crazy maze that is a life and into the future embodied by the most affective and direct person I've ever met.

The future is a big place, let's explore it!.